

## On the assessment of aspheric refractive microlenses

Présentée le 14 août 2020

à la Faculté des sciences et techniques de l'ingénieur  
Laboratoire de nanophotonique et métrologie  
Programme doctoral en photonique

pour l'obtention du grade de Docteur ès Sciences

par

**Jeremy BÉGUELIN**

Acceptée sur proposition du jury

Prof. C. Moser, président du jury  
Dr T. Scharf, directeur de thèse  
Prof. H. Gross, rapporteur  
Dr M. Schnieper, rapporteur  
Prof. N. Quack, rapporteur



# Abstract

Refractive microlenses and microlens arrays are key components for many applications such as optical data communication, laser and medical devices, or cameras. In particular, refractive micro-optics enables the miniaturization of high-tech systems but also offers novel optical functionalities. The success of this technology lies in the wafer-level fabrication technique, using the method of photoresist reflow with a subsequent pattern transfer into the substrate by reactive ion etching. Indeed, it allows the manufacturing in parallel of thousands of spherical or aspheric microlenses smaller than 1 mm. Their characterization is usually performed by measuring their surface, as this allows at the same time the evaluation of the microlens performance and feedback for fabrication process optimization. In this thesis, we assess this characterization approach to understand the fabrication process better and to improve the microlenses performance. Concretely, we first study surface form tolerancing, which is crucial to ensure the microlenses quality. However, the link between the surface form of a microlens and its performance is not straightforward, usually resulting in over-restrictive tolerances. Here, we investigate this connection for simple cases and then compare different approaches to tolerance typical micro-optical systems. Practical guidelines are proposed based on the results. Secondly, we present methods to improve surface measurements. For this, we develop an original calibration procedure that takes into account the aberrations of the imaging system. In the presented example, the accuracy is increased by a factor 7, rendering the characterization of diffraction-limited microlenses with high numerical apertures possible. Thirdly, we model the fabrication process to find correlations with the manufactured surface. Thereby, the fabrication optimization is made faster and more accurate. We validate this approach by increasing the uniformity of a large (100 mm  $\times$  100 mm) microlens array by a factor  $\sim 3$ . Finally, we evaluate another microlens characterization that consists of probing the optical functionalities in transmission and compare it to surface measurements. Particularly, we give the reasons for our doubts about its application to wafer-level microlenses. In conclusion, we show that a quantitative analysis of the microlens characterization allows for a significant improvement of the microlens quality and a better understanding of the fabrication process, resulting in lower production cost. For this reason, we believe that the results presented in this thesis will help to render wafer-level refractive micro-optics a more mature technology and build its bright future.



# Résumé

Les microlentilles réfractives et les réseaux de microlentilles sont des composants clés pour de nombreuses applications telles que la communication optique de données, les dispositifs laser et médicaux, ou encore les caméras. Plus particulièrement, la micro-optique réfractive permet la miniaturisation de systèmes de haute technologie, mais offre également de nouvelles fonctionnalités optiques. Le succès de cette technologie réside dans la technique de fabrication sur substrat, utilisant la méthode reconnue de fusion de résine photosensible suivie d'un transfert des structures dans le substrat par gravure ionique réactive. En effet, elle permet la fabrication, en parallèle, de milliers de microlentilles sphériques ou asphériques inférieures à 1 mm. Leur caractérisation s'effectue généralement par la mesure de leur surface par des profileurs optiques de surface, car cela permet à la fois d'évaluer la performance de la microlentille, et d'obtenir un retour d'informations qui servira à optimiser le processus de fabrication. Dans cette thèse, nous évaluons cette approche de la caractérisation pour mieux comprendre le processus de fabrication et améliorer la performance des microlentilles. Concrètement, nous étudions d'abord le tolérancement de la forme des surfaces qui est crucial pour assurer la qualité des microlentilles. Cependant, le lien entre la forme de la surface d'une microlentille et sa performance est complexe, ce qui entraîne généralement des tolérances trop restrictives. Ici, nous étudions cette connexion pour des cas simples, puis comparons différentes approches pour tolérer des systèmes micro-optiques typiques. Des recommandations pratiques sont proposées sur la base des résultats. Deuxièmement, nous présentons des méthodes pour améliorer les mesures de surface. Pour cela, nous développons une procédure d'étalonnage originale, qui prend en compte les aberrations du système d'imagerie. Dans l'exemple présenté, l'exactitude est augmentée d'un facteur 7, ce qui rend possible la caractérisation de microlentilles à haute ouverture numérique et limitées par diffraction. Troisièmement, nous modélisons le processus de fabrication pour le mettre en corrélation avec la surface fabriquée. De ce fait, l'optimisation de la fabrication est rendue plus rapide et plus exacte. Nous validons cette approche en augmentant l'uniformité d'un grand réseau de microlentilles (100 mm × 100 mm) d'un facteur  $\sim 3$ . Enfin, nous évaluons une autre caractérisation de microlentilles examinant les fonctionnalités optiques en transmission et la comparons aux mesures de surface. En particulier, nous expliquons les doutes que nous avons quant à son application aux microlentilles fabriquées sur substrat. En conclusion, nous montrons qu'une analyse quantitative de la caractérisation des microlentilles permet une amélioration significative de leur performance et une meilleure compréhension du proces-

## Résumé

---

sus de fabrication, résultant en une baisse des coûts de production. Pour cette raison, nous pensons que les résultats présentés dans cette thèse contribueront à rendre la micro-optique réfractive sur substrat plus mature et à construire son brillant avenir.

# Remerciements

Tout d'abord, je tiens à remercier mon directeur de thèse, Toralf Scharf, de m'avoir guidé tout au long de ce travail. Je ne connaissais pas Toralf lorsque j'ai débuté, mais j'ai appris à le connaître et il a fini par être mon collègue. J'ai énormément apprécié son soutien constant, son état d'esprit toujours positif et ses conseils qui ont donné forme à cette thèse. Ce travail n'aurait pas été possible sans son support et son engagement.

Mes remerciements vont ensuite à Reinhard Voelkel que j'ai rencontré par hasard dans un bar de Neuchâtel. Reinhard m'a d'abord proposé un stage et il m'a ensuite offert la possibilité de réaliser mon doctorat à SUSS MicroOptics (SMO). Accomplir ce travail dans une entreprise en plein développement a été une opportunité formidable dont j'ai énormément appris. Merci à lui pour la confiance qu'il a placée en moi.

Je remercie également Wilfried Noell, mon responsable au sein du département R&D, au contact de qui j'ai beaucoup appris grâce à sa large expérience et son savoir, ainsi qu'à ses remarques toujours constructives et précieuses.

Même si une thèse est un investissement personnel, il est toujours enrichissant de partager avec des personnes qui vivent la même expérience. Côté mes deux anciens collègues doctorants et amis, Raoul Kirner et Andreas Vetter, a donc été extrêmement formateur et motivant. Je les remercie pour leur soutien, leur aide qu'ils m'ont toujours généreusement accordée, et pour leurs conseils. À côté du travail, je garderai en mémoire les innombrables bières, les discussions engagées, les sorties VTT ou encore le surf à San Diego. Je remercie également Michail Symeonidis, un ancien doctorant de l'EPFL, avec qui j'ai collaboré. C'est lui qui a construit le setup et réalisé les mesures présentées au chapitre 5.

Ses propres idées sont toujours améliorées lorsqu'elles sont testées et malmenées en les partageant. Les résultats présentés dans cette thèse sont donc en partie le fruit de nombreuses discussions et échanges avec mes collègues. Toute ma gratitude va spécialement à Lisa Leonini, Justine Lullin, Sophiane Tournois, Philippe Dubois, Chen Yan et Giorgio Quaranta. Je remercie en particulier Pascal Pernet qui a récolté certaines données expérimentales présentées au chapitre 4 et qui a partagé avec moi son expérience sur les procédés de gravure.

## Remerciements

---

Garder la motivation est extrêmement important dans la réalisation d'un tel travail et l'ambiance positive qui règne à SMO y a fortement contribué. J'aimerais donc dire merci à tous mes collègues avec qui j'ai partagé de multiples discussions, des apéros ou des sessions de sport, et qui ont rendu mon temps à SMO particulièrement sympathique.

Finalement, un immense merci à ma famille et à mes amis, qui donnent un sens à tout ceci. Enfin et surtout, merci à mes parents, Elisabeth et Olivier, qui m'ont offert la possibilité de suivre le chemin que je désirais, qui m'ont toujours soutenu sans réserve et à qui, finalement, je dois tout.

*Neuchâtel, le 20 Mai 2020*

Jeremy



# Preface

It is a great honor and pleasure to have the opportunity to write the preface of Jeremy Béguelin's PhD thesis. Jeremy's work on the assessment of aspheric microlenses represents a big step forward for our company. A big step forward to ensure that we always deliver "perfect" microlenses to all our customers. Whereas "perfect" is related to the performance, the robustness, and the resilience of our microlenses within the application, the module or system of our customer. Jeremy has helped much to understand what is really important for characterizing a microlens and – if the surface is the key parameter – then get the error values below some 20 to 30 nanometers.

When we started the SUSS MicroOptics about 20 years ago, the micro-optics' world was much simpler. The common questions were: "What is a microlens, what is it good for and why should I use it?". Well, "a microlens is like a big lens, take - for example - the lens of your photo camera, but we make it much smaller. It is micro!" The answer to the second question was a bit more difficult. Micro-optics was still a kind of "exotic" product with a small supplier's base and even these suppliers had difficulties to tell their customers what the perfect parameters of the microlens they need are. Why should anybody use micro-optics? Well, the third question is answered today. Micro-cameras and microlens-based sensors are in all our smartphones, microlens fiber couplers are found in all data centers of the world, micro-optics is key for laser beam shaping, in life science, displays, sensing – microlenses are key enabling technology for many consumer and industrial products today. The next killer application for micro-optics seems to be automotive lighting. Microlens-based modules for interior, exterior lighting, microlens headlights, daylights and taillights are under development today. Why should microlens arrays be used in a car? Smaller, cheaper and better. Replacing big and heavy headlights by a small and more efficient microlens headlight might be a big step e.g. for electric cars to reduce weight and improve the range of the electric battery. Yet, integrating micro-optics in a car means that you have to fulfil the harsh quality standards of automotive industry. Once again, the correct assessment of aspheric microlenses is key to success.

Pioneer work on microlens testing was done by Prof. Johannes Schwider in the 1990. He and his PhD students were inventing various interferometers for microlens metrology. When we started the company, we installed his Mach-Zehnder and Twyman-Green interferometers in our first fab. This helped a lot to optimize our manufacturing processes. But still did not answer the question about the "perfect" lens parameters for our customer's specific application. We also found out that there are two fundamental limits of interferometric methods. First, the

sampling theorem and second, the fitting of a profile to the measured data. Over the years, we developed our internal tools and spent a lot of time improving our manufacturing and testing methods. However, a production team has certain limits of time and knowledge. This is where Jeremy stepped in and started to dig much deeper than anybody has done before within the frame of his PhD thesis work. Working already as a student at our company 5 years ago, he quickly got in and was well connected to our production and metrology teams. His supervisors Wilfried Noell and Toralf Scharf helped him much to go the very limits of microlens assessment.

In this thesis, Jeremy started by studying surface form tolerancing and its link to the optical performance related to different applications. He developed guidelines for specifications and tolerancing. Customers often tend to demand very harsh specifications. Just to be on the safe side. Often these specifications are not even related to the application but significantly reduce the yield in production. A smarter choice of tolerances allows to reduce costs and to improve the performance and process robustness of the customer's application. In a second step, Jeremy analyzed our different tools for contact and non-contact metrology of microlens surface profiles. A deep analysis of the process and instrument-related errors enabled him to significantly improve the instruments and methods. Finally, he transferred the obtained to optical design and modelling. This now allows "design for manufacturing" for microlens arrays. With more than 40'000 wafers (8") in our production today, the effects of Jeremy's work on cost reduction and quality improvement are very significant every day.

Jeremy's thesis is very well written, interesting to read and the obtained results are a big step forward for SUSS MicroOptics to keep our leading position in the micro-optics market. Congratulations to Jeremy for this extraordinary PhD thesis.

Dr Reinhard Voelkel, CEO SUSS MicroOptics

# Contents

<b>Abstract (English/Français)</b>	<b>i</b>
<b>Remerciements</b>	<b>v</b>
<b>Preface</b>	<b>vii</b>
<b>1 Introduction</b>	<b>1</b>
1.1 Purpose of the thesis . . . . .	2
1.2 Background and addressed problems . . . . .	3
1.3 Thesis structure . . . . .	7
<b>2 Microlens Surface Form Tolerancing</b>	<b>9</b>
2.1 Introduction . . . . .	9
2.2 Aspheric surface representation and fabrication . . . . .	11
2.2.1 Aspheric equation derivation . . . . .	11
2.2.2 Definition of tolerances . . . . .	13
2.2.3 Fabrication methods and typical surface form deviations . . . . .	14
2.2.4 Simulated distribution of microlenses . . . . .	15
2.3 Surface form deviation and optical performance . . . . .	16
2.3.1 Ideal aspheres . . . . .	17
2.3.2 Arbitrary aspheric surface forms . . . . .	20
2.3.3 Microlens arrays . . . . .	22
2.4 Comparison between different surface form representations . . . . .	23
2.5 Applications to real systems . . . . .	26
2.5.1 Fiber coupling . . . . .	26
2.5.2 Micro-projector . . . . .	27
2.6 Discussion . . . . .	29
2.7 Conclusion . . . . .	32
<b>3 Microlens Surface Measurement</b>	<b>33</b>
3.1 Introduction . . . . .	33
3.2 Geometrical model of optical surface profilers . . . . .	36
3.2.1 Standard calibration and uncertainty . . . . .	37
3.2.2 Reference balls and the random ball test . . . . .	38

## Contents

---

3.3	Advanced models of optical surface profilers . . . . .	42
3.4	Local plane surface approximation model . . . . .	44
3.4.1	Calibration . . . . .	45
3.4.2	Results and discussion . . . . .	49
3.4.3	Uncertainties . . . . .	56
3.5	Phase jumps in coherence scanning interferometry (CSI) . . . . .	58
3.6	Conclusion . . . . .	61
<b>4</b>	<b>Microlens Fabrication Modeling</b>	<b>63</b>
4.1	Introduction . . . . .	63
4.2	Photoresist thermal reflow . . . . .	65
4.2.1	Spherical cap creation by surface energy minimization . . . . .	65
4.2.2	Deviation from the ideal spherical cap case . . . . .	67
4.3	Reactive ion etching (RIE) process . . . . .	70
4.3.1	Directional etching . . . . .	71
4.3.2	Isotropic etching . . . . .	73
4.3.3	General case . . . . .	78
4.4	Uniformity improvement of microlens arrays (MLAs) . . . . .	79
4.4.1	Methods . . . . .	81
4.4.2	Results and discussion . . . . .	84
4.5	Conclusion . . . . .	87
<b>5</b>	<b>Microlens Characterization in Transmission</b>	<b>89</b>
5.1	Introduction . . . . .	89
5.2	Experimental setup . . . . .	90
5.3	Point spread function (PSF) measurements . . . . .	91
5.3.1	Quality assessment . . . . .	92
5.3.2	Feedback for process optimization . . . . .	94
5.4	Wavefront measurements . . . . .	95
5.4.1	Quality assessment . . . . .	96
5.4.2	Feedback for process optimization . . . . .	98
5.5	Conclusion . . . . .	101
<b>6</b>	<b>Conclusion</b>	<b>103</b>
6.1	Summary and discussion . . . . .	103
6.2	Outlook . . . . .	105
	<b>Bibliography</b>	<b>107</b>
	<b>Acronyms</b>	<b>119</b>
	<b>Nomenclature</b>	<b>121</b>

<b>Publications</b>	<b>125</b>
<b>Curriculum Vitae</b>	<b>127</b>



The first principle is that you must not fool  
yourself and you are the easiest person to fool.  
— Richard P. Feynman

À toutes les personnes que j'aime.





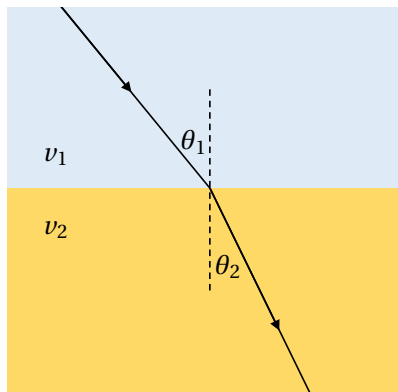
# 1 Introduction

Refraction is the change of propagation direction that happens to a ray of light when going from one medium to another one, in which the light travels at different speeds ( $v_1 \neq v_2$ ), see Fig. 1.1a. This phenomenon is described by Snell's law,

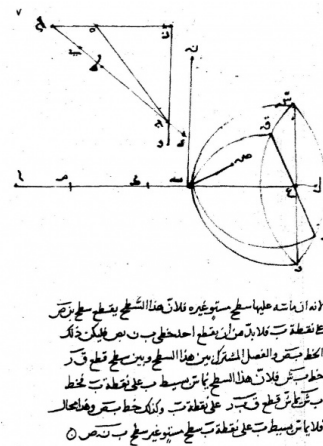
$$\frac{\sin \theta_1}{\sin \theta_2} = \frac{v_1}{v_2}, \quad (1.1)$$

which was first demonstrated by Sahl back in 984 [1, 2], see Fig. 1.1b. However, lenses that exploit the refraction to focalize beams of light and produce images have been manufactured and used since antiquity [3]. Examples of lenses are found in nature for a longer time as eyes are a vision system based on the principle of refraction.

Even though refraction is a simple and well-understood physics phenomenon, it has played



(a) Refraction of a ray of light between two media in which the light travels at different speeds. In this example,  $v_2 < v_1$ .



(b) The first proof of the law by Ibn Sahl around 984.

Figure 1.1 – The law of light refraction.

and still plays a fundamental role in our lives and human history. For example, telescopes allow us to observe and study the universe, microscopes allow us to observe and study the microscopic objects such as micro-organism and thus have been a fundamental tool for biology and medicine.

A refractive microlens is nothing else than a classical lens, but with dimensions in the micro-range. In a certain sense, refractive microlenses are the most recent and advanced form of refractive lenses. Typical microlenses have a diameter between  $100\mu\text{m}$  and  $1000\mu\text{m}$  and a height between  $1\mu\text{m}$  and  $300\mu\text{m}$ . Microlenses can be used individually, but one major advantage of refractive micro-optics is the possibility to create microlens arrays (MLAs) when fabricated at wafer-level. A microlens is the smallest possible refractive lens as the diffraction starts to be significant at smaller dimensions. For light control at a smaller scale, one has to rely on physical optics and the electromagnetic properties of light, as it is the case for metasurfaces, for instance.

There is no fundamental difference between a classical lens and a microlens since they both use refraction to shape beams of light. Besides the dimensions, fabrication and testing methods are the main differences. One can confidently say that the starting point of refractive micro-optics technology is the monolithic fabrication method that has been proposed in 1988 by Popovic & al. [4]. However, refractive micro-optics also exists in nature for a long time [5]. Moreover, biological systems are still inspiring engineers for developing new devices [6, 7].

At this point, we should motivate the use of micro-optics. The first reason for the existence of micro-optics is the general down-scaling trend in technology. For this reason, some means for controlling the light propagation at the micro range are needed. Another reason is the capability to create arrays that offer new optical functionalities. Among the main applications of refractive microlenses, we can mention their role in the following systems: fiber and waveguide couplers [8] for data communication [9], photolithographic systems [10, 11], wavefront sensors [12–14], and beam shaping systems [15–17]. More recently, refractive microlenses have been used as a key enabling component in systems such as cameras [18–20], in lighting systems of cars [21], and in the newly developed augmented/virtual reality displays [22]. All of these application fields are under thorough research and development.

In the end, all these systems rely on a curved surface, which is spherical or aspheric and which is the microlens key component. This thesis mainly focuses on such surfaces.

### 1.1 Purpose of the thesis

The goal of this thesis is to understand and improve the metrology of aspheric refractive microlenses fabricated at wafer-level. Indeed, it is evident that it is only possible to manufacture what can be measured, and thus the measurement accuracy poses the fundamental limit of the achievable microlens quality<sup>1</sup>. This fact is especially true for refractive micro-optics as the un-

---

<sup>1</sup>Throughout this thesis, the term quality refers to the optical performance of a microlens.

certainty of the surface measurements is sometimes above the tolerances. As a consequence, the first goal of this thesis is to assess and improve the accuracy of such measurements.

However, this is not the only limitation of the microlens quality. Indeed, to optimize the fabrication process, one has, as manufacturers, to link the surface parameters to the process parameters. When the correlation between the two sets of parameters is not entirely known, which is the case in reality as the fabrication process is complex, a certain unpredictability exists, which also limits the possibility of improving the fabrication process.

Finally, establishing the quality of a microlens from surface information is usually not a deterministic task. Again, the unknown relation between quality and surface, which means a non-perfect correlation, provokes a certain uncertainty that prevents the perfect knowledge of the optical performance of a given microlens.

In conclusion, the achievable quality is the combination of these three different uncertainties. Therefore, the goal of this thesis is to reduce them to improve the quality of the manufactured microlenses.

At this point, we should emphasize that this work is done in an industrial environment. The purpose of such research is thus not to improve one particular design and to produce a single microlens. It is rather to improve the quality of dozens of different microlens designs that span a large dimensional range and to improve the quality of thousands of microlenses. In consequence, practical considerations such as time, cost, and simplicity are crucial and drive the choice of the methods used for fabrication and characterization.

## 1.2 Background and addressed problems

In this thesis, we focus on aspheric microlenses, which allow a better optical performance compared to spherical microlens [23]. At SUSS MicroOptics, one fabricates the most common type of aspheres which are defined as conical surfaces whose sags are expressed by

$$z = \frac{r^2}{R \left( 1 + \sqrt{1 - (1 + \kappa) \frac{r^2}{R^2}} \right)}, \quad (1.2)$$

with  $r^2 = x^2 + y^2$ ,  $R$  the radius of curvature (ROC) at the vertex, and  $\kappa$  the conic constant. The surface is elliptic ( $\kappa \in (0, -1)$ ), parabolic ( $\kappa = -1$ ) or hyperbolic ( $\kappa < -1$ ) and is thus a generalization of a spherical surface ( $\kappa = 0$ ), see Fig. 1.2.

Designing such a surface consists thus of determining  $R$  and  $\kappa$ . This task is performed by the optical designer, who is usually the customer of the manufacturer. In principle, as manufacturers, we do not participate in this process step, we only confirm the feasibility of the microlens design.

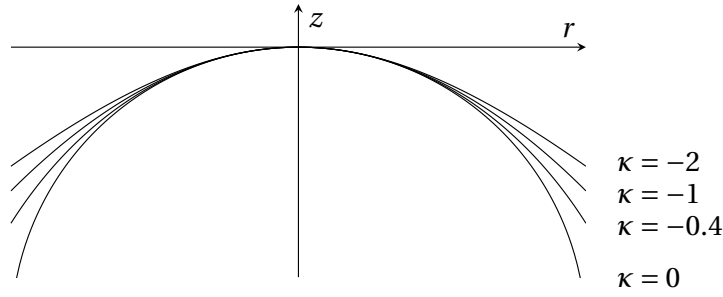


Figure 1.2 – Illustration of different aspheric profiles defined by a single ROC  $R < 0$  and multiple conic constants  $\kappa$ .

After the design of a surface is completed, the second step to undertake is tolerancing. Indeed, a microlens design is not complete if tolerances are not established. This step represents the major part of the interaction between the designer and the manufacturer. First, it has to be decided how the quality is assessed, meaning what should be measured. As the manufacturer is responsible for the quality control, this step is commonly performed through surface measurements, and for this reason, the surface has to be toleranced. Also, an inevitable negotiation happens as the manufacturer must propose realistic tolerances and as the designer always want the smallest tolerances possible.

Once the design and the tolerances are set, the microlens can be manufactured. Many different techniques exist to fabricate refractive microlenses [24]. Most of them use a substrate, usually a wafer, and process it to create a curved surface on one side. For this reason, microlenses are usually a plano-convex, even though curved surfaces can be created on both sides of the substrate. Usually, microlenses are convex, but concave microlenses also exist.

However, for high volume production, only the techniques that process the microlenses in a parallel way are suitable [25]. The first introduced and most common technique consists of the reflow of patterned photoresist cylinders with a subsequent transfer into the substrate by reactive ion etching (RIE) [4, 26], see Fig. 1.3. As this technique is used at SUSS MicroOptics for the fabrication of glass (fused silica) and silicon microlenses, this thesis focuses mainly on this fabrication technique. However, most of the considerations presented in this thesis are independent of the fabrication technique.

Another fabrication technique is replication by UV-imprint [27, 28]. This technique allows the fabrication in high volume production of polymer microlenses at wafer-level. Finally, we can also mention the direct writing [29–31] and micro-machining [32, 33] techniques that allow the fabrication of more complex surfaces with high accuracy. The drawback of these two methods is the time needed for fabrication, which prevents them from being used for high volume production at the moment. However, they can be used to create master templates for the UV imprint replication process.

To establish a manufacturing process, a certain number of trials are usually necessary. For each

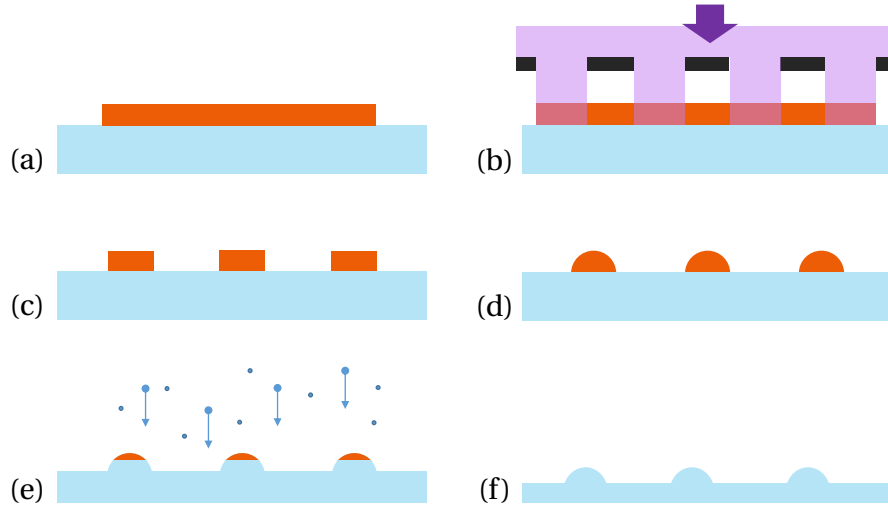


Figure 1.3 – Schematic of the microlens fabrication based on resist reflow with a subsequent reactive ion etching process. (a) A photoresist layer is spin-coated on the wafer. (b) The photoresist is exposed to ultraviolet radiation. (c) After development, cylinders of resist remain. (d) The wafer is heated for the resist to melt and form spherical caps by surface tension. (e) The RIE process transfers the spherical surface into the substrate. (f) Final microlenses.

trial, information about the surface, generally acquired by surface measurements, is required to provide feedback to optimize the process. This optimization process might seem evident if the surface deviation from the nominal surface is computed. However, the link between this quantity and the process parameters, typically the photoresist thickness or gas flows during the RIE process, must still be quantitatively established. We address this knowledge gap for the resist reflow with the subsequent RIE fabrication process.

Even if the process is optimized, the quality of the produced microlenses must still be verified after the surface fabrication. It does exist a list of standards by the International Organization for Standardization (ISO), ISO-14880 [34–38] that addresses the testing of microlenses, but it is already old and thus restrained. Indeed, the content of these standards is limited to low numerical apertures (NAs) and spherical microlenses. At SUSS MicroOptics, the most common and practical way to characterize microlenses is to measure their surface by optical surface profilers. The quality of a microlens is then ensured by tolerancing its surface. Ideally, the tolerances must be well correlated to the optical performance. Otherwise, quality control may be deficient, or the tolerances must be set too tight, which results in a costly fabrication. Nevertheless, tolerancing the surface form has not been explicitly addressed for micro-optics and conical surfaces, and we tackle this problem here.

Instead of measuring the surface to assess the microlens quality, it is also possible to directly probe the optical functionality. However, as mentioned previously, this operation is not

standard and approved for aspheric microlenses. Here, we discuss the possibility of using such an approach for the characterization of high NA microlenses.

The full fabrication process flow, from microlens design to quality assessment, is depicted in Fig. 1.4.

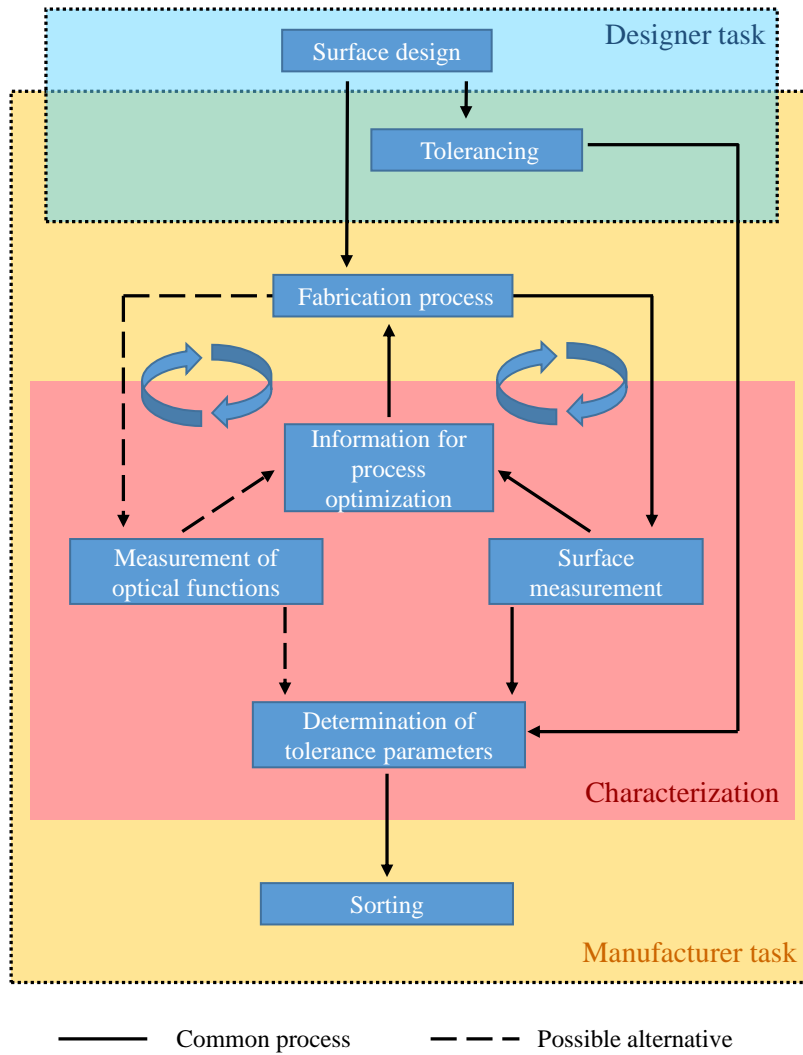


Figure 1.4 – Full process flow of a microlens surface fabrication. Once the surface design is made, i.e. determining the parameters  $R$  and  $\kappa$ , the surface can be manufactured. In parallel, tolerances must be established to determine the quality of the completed microlens. Once the surface is created, it is measured. Based on this measurement, two tasks are performed: firstly, information is extracted to provide feedback for process optimization. Secondly, the measured surface is compared to the tolerances to assess the quality. In red are the steps that we define as the characterization of the microlens, and this is what we consider in this thesis.

In summary, the problems we address to achieve the goal of this thesis can be synthesized by the following points:

- Assessment of the optical quality of a microlens based on its surface form and its corollary, tolerancing the form of the microlens surface.
- Evaluation and improvement of the accuracy of surface measurements by optical profilers.
- Modeling of the fabrication process to link process parameters to surface form.
- Evaluation of the possible characterization based on the measurement of the optical functionality (wavefront, point spread function (PSF)) in transmission.

As the microlens fabrication process is becoming more and more industrialized, the full process flow must be characterized and optimized to be more efficient in terms of cost and time. For this reason, the work presented in this thesis is inevitably quantitative: mathematical and statistical tools are thoroughly used for modeling purposes. We strongly believe that only such an approach allows us to push the achievable microlens quality further.

## 1.3 Thesis structure

Following the schematic Fig. 1.4 and the addressed problems, this thesis is divided into four core chapters:

In the first chapter, dedicated to tolerancing the surface form of aspheric microlenses, we start from the basics by deriving Eq. (2.1) from optical principles and show the optical signification of the geometrical parameters. Using ray optics, we link the surface form to the optical performance for simple cases to understand how tolerancing should be performed. The different approaches for tolerancing are then compared for real examples, and practical guidelines are given.

In the second chapter, we discuss the measurement of the microlens surface by optical surface profilers. In particular, we show that errors in the measurement appear, especially when the surface slope is significant. We first investigate these errors and then propose methods to correct them. We also estimate the accuracy of such measurements by deriving the uncertainties.

In the third chapter, we model the microlens manufacturing based on photoresist reflow with a subsequent RIE process. Such modeling is intended to provide quantitative feedback to optimize the fabrication process. As a practical application and validation, we use the derived models to improve the uniformity over a large ( $> 100 \text{ mm} \times 100 \text{ mm}$ ) MLA.

In the fourth and final chapter, we discuss the characterization in transmission of high NA

## **Chapter 1. Introduction**

---

microlenses whose surface cannot be measured in reflection. Measurement of the PSF and wavefront are discussed and compared.

Finally, a conclusion summarizes the results presented in this work and discusses how the goal of the thesis is achieved. An outlook about future work is also given.



## 2 Microlens Surface Form Tolerancing

In this chapter, we discuss the process of tolerancing the surface form of aspheric microlenses. We first review and discuss the existing surface representations. Then, we link the surface form to the optical performance for simple systems, thus suggesting optimal representations for tolerancing. Finally, we compare the different approaches for idealized and real systems. Based on the results, we propose practical guidelines.

### 2.1 Introduction

The optical characteristics of a plano-convex aspheric refractive microlens are determined by the form of its curved surface. For this reason, tolerancing effectively the form of such surfaces is an essential step towards the performance control of microlenses.

The subject of tolerancing the form of optical surfaces is discussed in different works [39, 40] and is summarized by a series of the ISO standards [41]. However, these approaches have been mainly created for spherical lenses, and their generalization to aspheric surfaces is rather general as there are many different ways to define aspheres. In particular, the case of conical surfaces that we are interested in has not been specifically studied, and for this reason, we discuss it here in more detail. Another originality of the work presented here is the adaption of the tolerancing procedure to micro-optics. Even though the operating principle between classical lenses and microlenses is identical as they both rely on refraction, the fabrication and the testing methods are very different, and we propose a few adjustments.

Wafer-level optics (WLO) fabrication techniques allow the manufacturing in parallel of up to tens of thousands of microlenses on a single wafer. An avoidable drawback of the wafer-level fabrication is that the surface of the individual microlenses cannot be formed independently. It may happen that over one substrate, there are elements that meet the optical specification and others that do not. For this reason, it is essential to tolerance effectively wafer-level aspheric microlenses. Indeed, tighter tolerances than needed results in an unnecessary discarding of microlenses and an increase in the fabrication cost. Another drawback of wafer-level

## Chapter 2. Microlens Surface Form Tolerancing

---

fabrication is its difficulty in producing arbitrary surface forms. This is why microlenses are usually restricted to conical surfaces, which are considered here.

The metrology of the microlenses surface is also different from its macroscopic counterpart. The surface form measurement of microlenses usually relies on optical surface profilers, whereas for classical lenses, this operation is mainly based on wavefront deformation measured by interferometry [42]. This difference leads to slight deviations in the definition of the surface form tolerances.

The process of tolerancing can be described in two steps. First, a surface form representation, i.e., a set of parameters that represents the surface form, is chosen. This choice is fundamental: indeed, if the correlation between these parameters and the optical performance is weak, then it is difficult to establish the quality of the microlens. To motivate a reasonable choice of surface representation, we investigate here the link between the optical performance and the surface form for simple systems by using ray-optics. The second step is an evaluation of the performance degradation of the optical system as a function of random perturbations of the surface form. To perform this step as accurately and realistically as possible, we include, as a manufacturer of wafer-level optics, typical distributions of measured surface form deviations. Once the optical performance is evaluated for the simulated distribution of microlenses, the tolerances for each parameter of the surface representation are determined. This step is an optimization problem since the number of elements that fulfill the optical specification must be maximized. We address this optimization by using global optimization algorithms. This task of performance degradation assessment by perturbation simulation is of major importance when the correlation between the chosen surface representation and the optical performance is not excellent. On the other hand, if the correlation between surface representation and optical performance is perfect, this step is useless.

Here, we make the exercise of tolerancing the surface form based on different representations to compare them. First, for simple systems and then for typical real systems. Based on the results, we propose guidelines to tolerance effectively aspheric microlenses used in different optical systems. Moreover, all parameters and terms that are used or introduced are defined and motivated. It is done to avoid any confusion and to stress the need for standardization in this domain.

This chapter starts with a discussion about the representation of aspheric surfaces, Section 2.2. It also includes typical surface form deviations. In Section 2.3, we try to derive ideal surface form tolerances by linking optical merit functions and surface forms for simple systems. The comparison between selected surface form representations is made for these simple systems in Section 2.4 and in Section 2.5 for real micro-optical systems. Discussion of the results, as well as the general guidelines, are presented in Section 2.6. Finally, conclusions are presented in Section 5.5.

## 2.2 Aspheric surface representation and fabrication

In this work, by an aspheric surface, we mean a rotationally symmetric conical surface defined by its sag [43]

$$z(r) = \frac{r^2}{R \left( 1 + \sqrt{1 - (1 + \kappa) \frac{r^2}{R^2}} \right)}, \quad (2.1)$$

with  $R$  the ROC,  $\kappa$  the conic constant, and  $r^2 = x^2 + y^2$  the radial position. In micro-optics, higher-order surfaces defined with supplementary even polynomials are usually not considered because of fabrication limitations. The resist reflow produces a spherical cap, and the RIE process sets the asphericity. However, it is technologically difficult to produce large deviations from a spherical form, and no other parameters are thus needed to quantify the achievable surface forms.

### 2.2.1 Aspheric equation derivation

This section aims to motivate the use of conical surfaces and to link the geometrical parameters,  $R$  and  $\kappa$ , to the optical ones, the focal length in particular. To do so, the equation Eq. (2.1) is derived from optical principles. To start, we consider the case of a plano-convex lens that focuses a plane wave towards its front focus, see Fig. 2.1.

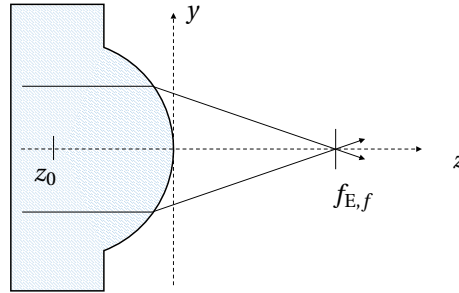


Figure 2.1 – Plano-convex lens with an effective front focal length  $f_{E,f}$

The lens surface  $z = s(y)$  is unknown, and we express the optical path difference (OPD) at the focus by using ray optics and the law of refraction. By convention, the phase at the vertex position is set to zero. On-axis, at an arbitrary position  $z_0$  into the substrate, the phase of the plane wave is  $\phi_0 = knz_0$ ,  $k$  being the wave number<sup>1</sup> and  $n$  the refractive index. Any ray that is only defined by its  $y$ -position  $\tilde{y}$  hits the surface at a position  $(\tilde{y}, \tilde{z} = s(\tilde{y}))$  with a phase

$$\phi = \phi_0 + kn(\tilde{z} - z_0) = kn\tilde{z}. \quad (2.2)$$

After the refraction, rays are linear functions  $y = m(z - \tilde{z}) + \tilde{y}$ . The slope  $m$  is obtained by the

<sup>1</sup>The wavenumber  $k$  should not be confused with the conic constant represented by the Greek letter kappa ( $\kappa$ ).

## Chapter 2. Microlens Surface Form Tolerancing

---

law of refraction and is given by:

$$m = \tan \left( \arcsin \left( n \sin \left( \arctan \left( \tilde{z}' \right) \right) \right) - \arctan \left( \tilde{z}' \right) \right), \quad (2.3)$$

with  $\tilde{z}' = ds(\tilde{y})/dy$ . Thus, the phase of the rays at the front focal position  $f_{E,f}$  is:

$$\phi = kn\tilde{z} + k\sqrt{\tilde{y}^2 + (f_{E,f} - \tilde{z})^2} = k \left[ n\tilde{z} + (f_{E,f} - \tilde{z})\sqrt{m^2 + 1} \right]. \quad (2.4)$$

The phase of the ray that follows the optical axis is given at the focus by  $kf_{E,f}$ . If the lens is ideal, then the phase of all rays is the same. This gives:

$$f_{E,f} = n\tilde{z} + (f_{E,f} - \tilde{z})\sqrt{m^2 + 1}. \quad (2.5)$$

In the ideal case,  $m$  can be rewritten:

$$m = -\frac{\tilde{y}}{f_{E,f} - \tilde{z}}, \quad (2.6)$$

and Eq. (2.5) can be expressed as

$$\sqrt{(f_{E,f} - \tilde{z})^2 + \tilde{y}^2} = f_{E,f} - n\tilde{z}. \quad (2.7)$$

This is a standard second-order equation whose solutions are given by

$$\frac{-A \pm \sqrt{A^2 + B\tilde{y}^2}}{B} \quad \text{or by} \quad \frac{\tilde{y}^2}{A + \sqrt{A^2 + B\tilde{y}^2}}, \quad (2.8)$$

with  $A = f_{E,f}(1 - n)$  and  $B = n^2 - 1$ . By identification with Eq. (2.1), we finally obtain  $R = f_{E,f}(1 - n)$  and  $\kappa = -n^2$ . In other words, an aspheric conical surface focuses perfectly a plane wave traveling parallel to the optical axis towards its front focus and for any NA within limits imposed by total internal reflection.

If the plane wave comes from the front side and the light is focused in the substrate, similar relations can be found:  $R = \frac{n-1}{n}f_{sub}$  with  $f_{sub}$  the focal length defined from the lens vertex and  $\kappa = -1/n^2$ .

In other situations, when the light is refracted at the two interfaces, a conical surface does not produce an aberration-free image of an on-axis point source. However, practically, such surfaces still give good enough results and can be used as a design surface. As the two analytical examples are two extreme cases, the optimal conic constant value lies in the interval  $[-n^2, -1/n^2]$ .

### 2.2.2 Definition of tolerances

In practice, there is always a deviation from the surface design. Such deviation can be quantified by using different tolerances. ISO 10110-5 proposes a non-exhaustive list of these parameters. Here, we clarify the definition of some of them in the case of micro-optics and extend them to the case of conical surfaces.

The microlens tolerancing depends obviously on what quantity is measured, but also on how it is measured. The measurement of the microlenses surface is commonly performed by optical surface profilers such as confocal microscopes or coherence scanning interferometers or by mechanical stylus profilers. All instruments directly provide the surface sag (the  $z$  position). This is different from classical optics, where lens surfaces are usually tested by interferometry [42, 44]. In interferometric testing, the surface form deviation is measured as a wavefront deformation and is defined perpendicularly to the surface [41]. For this reason, all the surface form tolerances established for classical optics, except the sagitta deviation, are defined to be perpendicular to the nominal surface. In the context of micro-optics, we propose to reuse most of the terms defined in ISO 10110-5 [41] but to define them to consider deviations along the  $z$ -axis. In our approach, sagitta deviation and surface form deviation are thus equivalent for microlenses.

Another specificity of micro-optics is the substrate, which is considered to be the reference flat. In this case, it does not make sense for the tilt to be excluded from the total surface deviation.

An important parameter that has to be redefined for conical surfaces is irregularity. For a spherical surface, irregularity is defined as the best sphere fit residual. Consequently, it is the component of the surface form deviation that cannot be compensated by refocusing [45]. For this reason, we propose to keep the term irregularity for the surface deviation from the best aspheric fit with the ROC  $R$  as a fit parameter but with the conic constant  $\kappa$  being fixed at its nominal value  $\kappa_n$ . Indeed, only a deviation of ROC can be compensated by refocusing, whereas a deviation of conic constant provokes spherical aberration that cannot be compensated. We propose to use the term aspheric irregularity for the similar case where  $\kappa$  is also considered as a variable of the fit. Similarly, we also define the irregular slope deviation root mean square (RMS) that is not defined in ISO 10110-5. All these quantities are summarized in Table 2.1. This list is not exhaustive and may be completed when needed.

Table 2.1 – Explanation of the terms used in this thesis. Most of them are inspired by ISO 10110-5, but deviations are always computed along the  $z$ -axis. The variables  $X$ ,  $Y$ , and  $Z$  represent the position of the surface vertex, which is, by definition of Eq. (2.1), positioned at  $(0,0,0)$ .

Surface form tolerance	Nomenclature	Fit variables
total surface deviation RMS	RMSt	$X, Y, Z$
irregularity RMS	RMSi	$X, Y, Z, R$
aspheric irregularity RMS	RMSai	$X, Y, Z, R, \kappa$
total slope deviation RMS	RMSt $\Delta$ S	$X, Y, Z$
irregular slope deviation RMS	RMSi $\Delta$ S	$X, Y, Z, R$

### 2.2.3 Fabrication methods and typical surface form deviations

As previously mentioned, when the correlation between the optical merit function and the chosen tolerances is not ideal, which is usually the case in practice, it is important to simulate perturbations of the surface form that are as close as possible to reality to assess the performance degradation. When the simulation does not correspond to reality, there is a risk of two failures. Firstly, the performance degradation is overestimated, which leads to tolerances that are too tight. Secondly, the inverse, the degradation is underestimated, with the consequence that the optical system does not work correctly.

For this reason, we provide two examples of surface form deviation. For a qualitative assessment, these surface deviations are decomposed into Zernike polynomials [46]. Figure 2.2 presents typical surface form deviations produced by the photoresist reflow with the subsequent RIE process fabrication method. One advantage of this fabrication method is that the produced surfaces mainly consist of low spatial frequencies, and thus the 30 first Zernike polynomials are usually sufficient for accurate modeling. The remaining RMS value of the Zernike representation (roughness) is typically a few nanometers and is thus negligible. The distribution in Fig. 2.2 is obtained by measuring the surface of 300 microlenses in silicon (diameter  $2a = 480\mu\text{m}$ ,  $R = 525\mu\text{m}$ ,  $\kappa = -2.5$ ) with a confocal microscope. Defocus is clearly the main component of the surface form deviations. We explain this by the non-uniformity of the etching chamber, and we can correct it as discussed in [47] and Section 4.4. The measured second and third orders have a quasi null value, which confirms that the microlenses are not tilted.

Figure 2.3 presents the same distribution but for polymer microlenses replicated by UV imprint on a glass substrate ( $2a = 790\mu\text{m}$ ,  $R = 1043\mu\text{m}$ ,  $\kappa = -0.4$ ). The same main conclusions can be done: defocus is the main component, and tilt is negligible. However, we note that the amplitude of the deviation is lower in this specific example.

These measured surface form deviations can be used to create a random distribution of surfaces during the tolerancing process.

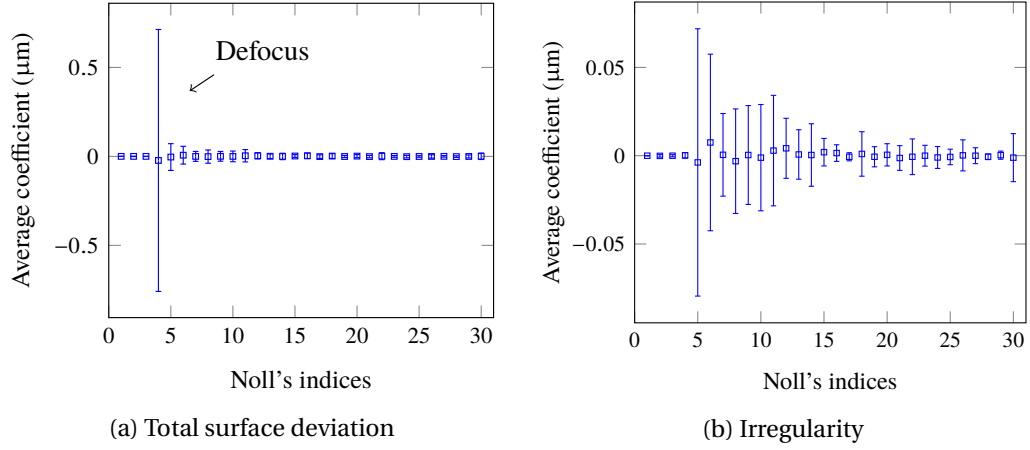


Figure 2.2 – (a) Zernike representation of the surface form deviation for a typical measured distribution over one wafer of silicon microlenses manufactured by reactive ion etching. Value is given as the distribution average. Error bars half-length is one standard deviation. Indexing follows Noll's convention [48]. It is seen that process non-uniformity is mainly translated into a spread of focal lengths. (b) Zernike representation of the surface irregularity.

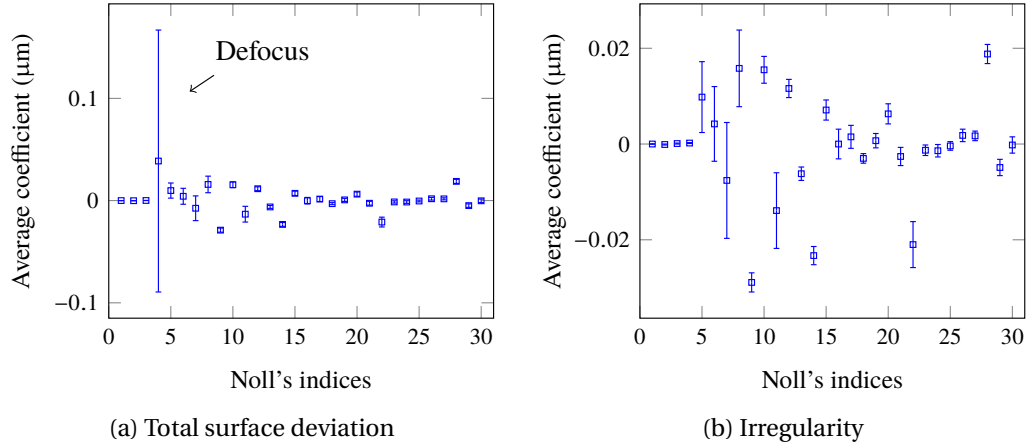


Figure 2.3 – (a) Zernike representation of surface forms deviation for a typical measured distribution over one wafer of replicated microlenses manufactured from a resist reflow template. Value is given as the distribution average. Error bars half-length is one standard deviation. Indexing follows Noll's convention [48]. (b) Zernike representation of the surface irregularity.

### 2.2.4 Simulated distribution of microlenses

The Zernike representation of the surface form deviation allows us to simulate the perturbations to perform tolerancing. Indeed, the coefficient of each Zernike polynomial can be assumed to be a random variable with a particular distribution. The uniform distribution is chosen here instead of the normal distribution because it is considered to be more conservative [45].

In this chapter, we construct a perturbation distribution that mimics the distribution in Fig. 2.2a because this thesis focuses on the photoresist reflow with the subsequent RIE process technique. The designer should, however, use the most realistic distribution for its product. To create this distribution, we consider only the Zernike orders 4 to 30. Also, for simplicity, we assume that all random variables (coefficients) are independent. We also assume that they all have the same uniform distribution with a mean of zero. The only exception is the defocus, which is assumed to have a standard deviation 8 times higher, see Fig. 2.4.

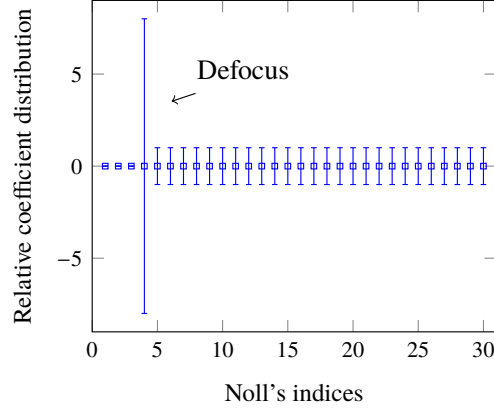


Figure 2.4 – Zernike representation of the simulated surface form deviations used in this chapter. The coefficients are independent uniform random variables, and the error bars half-length is one standard deviation of the distribution. Indexing follows Noll's convention [48].

In order to obtain perturbations with increasing amplitudes, for each trial, only the relative value of the coefficients is used. Each coefficient is then normalized to produce a surface form deviation with the desired RMS value.

It has to be stressed again that the choice of the distribution only matters when the correlation between the surface form tolerances and the optical figure of merit is weak. In this case, the optical designer is encouraged to get an insight into typical surface form deviations from the manufacturer.

### 2.3 Surface form deviation and optical performance

To link the lens surface form and the lens optical performance, we first have to establish what is usually the optical performance. Among the most popular optical figure of merit (FOM), we can mention [49] the RMS spot size, the modulation transfer function (MTF), the wavefront aberration, and the Strehl ratio. Here, we consider the RMS spot size and the RMS wavefront aberration depending on the desired optical quality of the microlens.

In this section, we restrict our discussion to the case of a plane wave focused on-axis. This restriction is motivated by several reasons: firstly, because important applications of microlenses are on-axis systems such as fiber coupling or beam shaping. Secondly, it is a simple



case that allows analytical derivations and consequently offers an excellent platform to discuss concepts. Finally, it can be seen as the starting point for an off-axis focusing description, when the latest is considered to be a perturbation of the on-axis case, which is reasonable for small angles. The off-axis case is nevertheless considered in Section 2.5.2.

The optical systems considered in this section and in the next one, Section 2.4, are depicted in Fig. 2.5. Typical geometrical parameters are chosen for the microlens. As defined in ISO 14880-1 [34], they are: diameter  $2a = 300 \mu\text{m}$ , ROC  $R = 500 \mu\text{m}$ , conic constant  $\kappa = -2.25$  or  $\kappa = -0.54$ , refractive index  $n = 1.5$  and substrate thickness  $T = 500 \mu\text{m}$ .

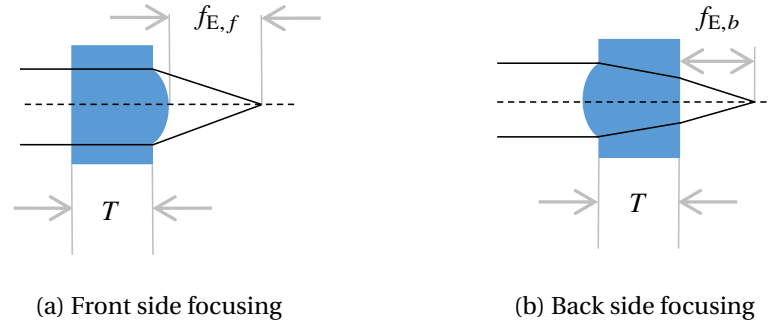


Figure 2.5 – Schematic of the optical systems considered in Sections 2.3 and 2.4. A plane wave is focused on-axis by a microlens towards its front side (a) or its backside (b). The microlens parameters are: diameter  $2a = 300 \mu\text{m}$ , ROC  $R = 500 \mu\text{m}$ , refractive index  $n = 1.5$  and substrate thickness  $T = 500 \mu\text{m}$ . Conic constant optimal value is  $\kappa = -0.54$  for backside focusing and  $\kappa = -2.25$  for front side focusing.

### 2.3.1 Ideal aspheres

First, we focus on "ideal" aspheres. This means aspheric surfaces whose ROCs and conic constants deviate from their nominal values but without any irregularity. This makes the situation easy to work with because the surface is defined by only 2 parameters and allows for a graphical representation.

In this example, the figure of merit is chosen to be the on-axis RMS spot size. It is calculated as a function of  $R$  and  $\kappa$  for the system considered in Fig. 2.5b. Figure 2.6a presents the results without focus compensation. The RMS spot size is almost constant along a diagonal in the  $R/\kappa$  space. By looking at Fig. 2.6e, we observe that the RMS spot size is mainly a consequence of defocus, which seems to be a linear function of  $\Delta R$  and  $\Delta \kappa$ . In the next section, we confirm this linear relation and show how to derive it. A change of conic constant thus provokes a defocus on top of spherical aberration. For this reason, the RMS spot size provoked by a change of ROC can be partially compensated by a change of conic constant. Finally, Fig. 2.6c shows that RMSt is well correlated to RMS spot size in this particular case.

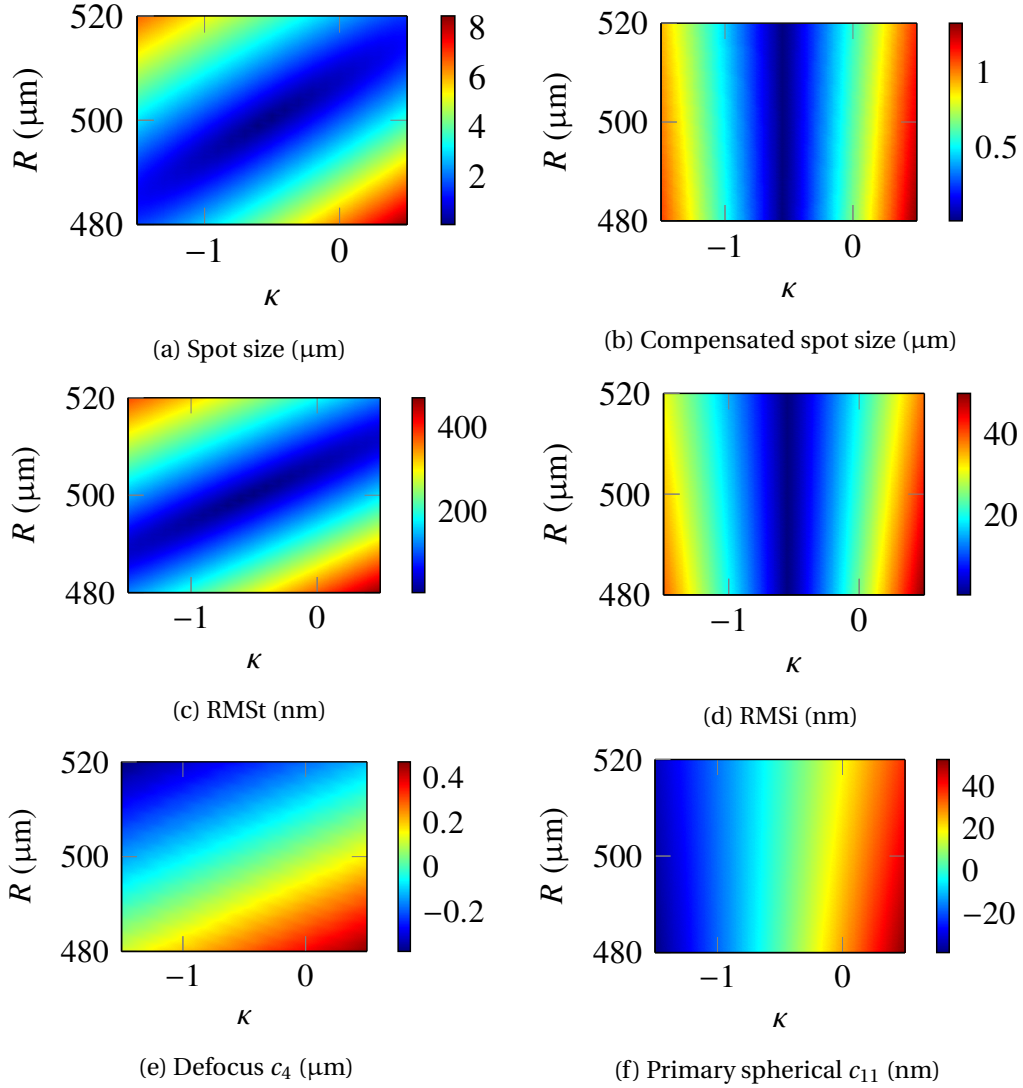


Figure 2.6 – RMS spot size with and without focus compensation as well as different surface form tolerances for ideal aspheres in the range  $R = 500 \pm 20 \mu\text{m}$  and  $\kappa = -0.54 \pm 1$ . It is seen that RMS spot size is well correlated with RMSt and Zernike defocus  $c_4$ . Likewise, if focus compensation is used, RMS spot size is well correlated to RMSi and Zernike primary spherical  $c_{11}$ . The relation between these parameters can be mathematically explained.

With focus compensation, see Fig. 2.6b, the RMS spot size becomes almost uniquely a function of the conic constant. This is explained by the fact that the level of spherical aberration is uniquely defined by the conic constant deviation, see Figure 2.6f. Finally, Fig. 2.6d shows that RMSi is well correlated to RMS spot size in this particular case.

These results lead to ways of tolerancing ideal aspheres: for systems without focus compensation, because the defocus is a linear function of  $\Delta\kappa$  and  $\Delta R$ , tolerances of the form  $R = R_n \pm \Delta R$  and  $\kappa = \kappa_n \pm \Delta\kappa$  are inefficient. Graphically, this can be seen by the fact that the tolerance

bands can only represent a rectangle in the  $R/\kappa$  space, which cannot fit the diagonal observed in Figs. 2.6a, 2.6c and 2.6e. Different ways are possible to increase the tolerancing efficiency: tolerance RMSt or tolerance  $c_4$  and  $c_{11}$  at the same time, meaning constructing a trapezoid in the  $R/\kappa$  space. Another option is to create a function of  $R$  and  $\kappa$  that can be used to perform the tolerancing.

It is interesting to note that, for systems with focus compensation, tolerances of the form  $R = R_n \pm \Delta R$  and  $\kappa = \kappa_n \pm \Delta \kappa$  are efficient. Indeed, the optical performance is well correlated to the conic constant.

#### Relation between $R$ , $\kappa$ , and Zernike defocus coefficient $c_4$

To qualitatively understand the results about ideal aspheres, we investigate the link between three parameters:  $R$ ,  $\kappa$ , and Zernike defocus coefficient  $c_4$ . To allow analytical derivations, we consider the Taylor expansion of Eq. (2.1) to the 4th order:

$$z(r) \sim \frac{1}{2R} r^2 + \frac{(1+\kappa)}{8R^3} r^4. \quad (2.9)$$

For a microlens with  $R = 500 \mu\text{m}$ ,  $2a = 300 \mu\text{m}$  and  $\kappa = -0.54$ , the RMS value of the difference between the Taylor expansion and the complete expression is 1.2 nm. This is acceptable for tolerancing purposes when small perturbations of the surface are considered.

The defocus  $c_4$  is given by the scalar product of the defocus polynomial expression and the aspheric formula. The scalar product is the integral over a unit disk, and for this reason, the variable change  $r = a\rho$  is made,  $a$  being the semi-aperture and  $\rho$  the normalized radial position. This is expressed by

$$c_4 = \int_0^{2\pi} d\theta \int_0^1 d\rho \sqrt{3} (2\rho^2 - 1) \left( \frac{a^2}{2R} \rho^2 + \frac{(1+\kappa)a^4}{8R^3} \rho^4 \right). \quad (2.10)$$

And after integration, by:

$$c_4 = \frac{\pi a^2}{15R} + \frac{3\pi(1+\kappa)a^4}{140R^3}. \quad (2.11)$$

Again, it has to be stressed that we are interested in small perturbations, thus in the differential form of this equation which reads,

$$c_4 = \left( -\frac{\pi a^2}{15R_n^2} - \frac{9\pi(1+\kappa_n)a^4}{140R_n^4} \right) \delta R + \frac{3\pi a^4}{140R_n^3} \delta \kappa. \quad (2.12)$$

The subscript " $n$ " is here to stress that we consider a deviation from the nominal surface. Defocus is thus a linear function of  $\delta R$  and  $\delta \kappa$ , which is confirmed in Fig. 2.6e. This means that a change of radius of curvature can be compensated by a change of conic constant. This also means that if a lens suffers from spherical aberration, it is possible to reduce it by slightly moving the lens out of its paraxial focus.

What is also interesting to look at is the amount of information carried by  $R$  and  $\kappa$  that is actually supported by  $c_4$ . To do so, we calculate the projection of the 4th order in Eq. (2.9) on  $c_4$ . Because this is independent of the vector length or polynomial coefficient, it is given by:

$$\cos(\theta) = \frac{\langle x^2, x^4 \rangle}{|x^2||x^4|} = \frac{\sqrt{45}}{7} \approx 0.96. \quad (2.13)$$

This shows that defocus contains most of the information represented by  $R$  and  $\kappa$ . This explains why, in Fig. 2.6, the RMS spot size, RMSt, and  $c_4$  have an excellent correlation. This fact and Eq. (2.12) are a justification for the fact that  $R$  and  $\kappa$  should not be toleranced independently when refocusing cannot be performed.

### 2.3.2 Arbitrary aspheric surface forms

The surface of a microlens needs an infinite number of parameters to be defined, or practically, a high enough number of coefficients for a given accuracy. An intuitive approach to tolerance arbitrary surface forms would be to transfer the methods discussed for ideal aspheres and to tolerance the aspheric irregularity, which is the deviation from the best asphere fit,  $R$  and  $\kappa$  being fit parameters, see Table 2.1. This approach, which one commonly encounters in practice as manufacturers, is compared to others in the next section, Section 2.4.

Another option is to express the optical figure of merit (FOM) as a function of the surface and investigate the link between surface form deviation and optical performance degradation. Unfortunately, this is impossible in practice for most cases because the merit function cannot be analytically expressed as a function of the surface. An exception is the case of a plane wave focused towards the front focal spot of a plano-convex microlens, see Fig. 2.5a, when the FOM is represented by the geometrical lateral aberration (spot size) or by the wavefront aberration. These two cases are treated here consecutively.

#### RMS spot size

To start the investigation, we note that when the lens surface  $z = s(y)$  is optimized, all rays have zero lateral aberration  $u$  at the focal spot  $z = f_{E,f}$ . As in Section 2.2.1, a ray is defined only by its  $y$  position  $\tilde{y}$  when collimated and by a linear function,  $y = \tilde{y} + m(z - s(\tilde{y}))$ , after refraction. In this ideal case, all rays thus satisfy the following condition:

$$v \equiv \tilde{y} + m(f_{E,f} - s) = 0. \quad (2.14)$$

Now, a real surface has a certain surface form deviation, which is usually small compared to the nominal surface itself. One can take a first-order perturbative approach and rewrite the previous equation:

$$v + \delta v = \tilde{y} + (m + \delta m)(f_{E,f} - (s + \delta s)) \approx y + m(f_{E,f} - s) + \delta m(f_{E,f} - s) - m\delta s. \quad (2.15)$$

### 2.3. Surface form deviation and optical performance

By identification, when the second orders are neglected, the lateral aberration at the focal spot is given by:

$$\delta v \approx \delta m(f_{E,f} - s) - m\delta s \approx (n-1)\delta s'(f_{E,f} - s) - (n-1)s'\delta s, \quad (2.16)$$

with  $s$  the microlens sag,  $\delta s$  the surface form deviation,  $s'$  the slope,  $\delta s'$  the slope deviation,  $n$  the refractive index and  $f_{E,f}$  the effective front focal length. Typical values for these parameters are:  $|s| < 30 \mu\text{m}$ ,  $|\delta s| < 1 \mu\text{m}$ ,  $|\delta s'| < 50 \text{ mrad}$ ,  $|s'| < 0.5 \text{ rad}$ , and  $f_{E,f} \approx 1000 \mu\text{m}$ . This means that the first term,

$$\delta v \approx (n-1)(f_{E,f} - \bar{z})\delta s', \quad (2.17)$$

is usually the most significant and because  $f_{E,f} \gg s$ , it can be assumed to be a linear function of  $\delta s'$ . This reads

$$\delta v_{RMS} \propto \delta s'_{RMS}. \quad (2.18)$$

This suggests that the slope deviation should be toleranced, as already mentioned by ISO 10110-5. This is confirmed in Fig. 2.7a, which shows the excellent correlation between the on-axis RMS spot size and the slope deviation RMS for the simulated distribution of microlenses defined in Section 2.2.4 above.

Likewise, Figure 2.7b presents the RMS spot size as a function of the irregular slope deviation RMS for the same distribution of microlenses, but when defocus is compensated. In this case, the correlation is not as good as before. This is likely because the fit parameter  $R$  and focus compensation do not exactly represent the same degree of freedom.

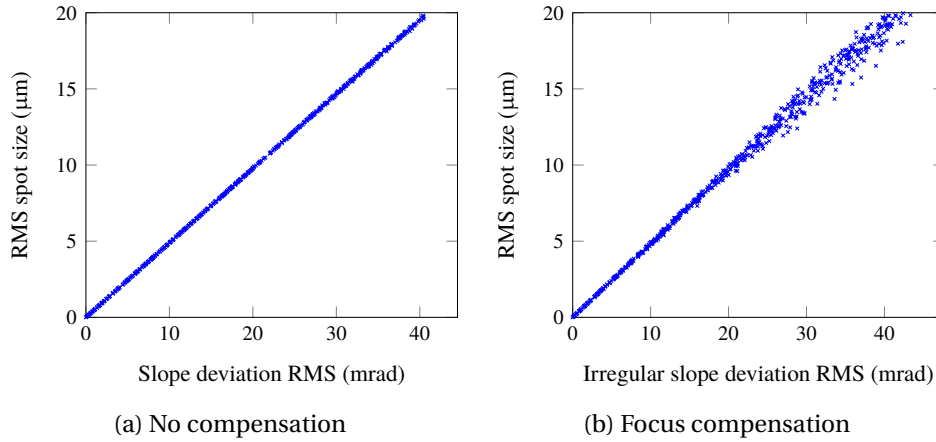


Figure 2.7 – On-axis RMS spot size as a function of slope deviation for the simulated distribution of surfaces as described in Section 2.2.4. Without focus compensation, the correlation between RMS spot size and total slope deviation RMS is almost perfect, thus suggesting that the total slope deviation RMS might be a powerful surface form tolerance. With compensation, the correlation between irregular slope deviation and RMS spot size is less good but still a right candidate for tolerancing.

### Wavefront aberration

Following the same idea, it is possible to perform a perturbative approach to approximate the wavefront aberration for the same optical system. We start by considering the phase at the vertex plane for a ray  $\tilde{y}$ . Using optical path length, see Section 2.2.1, it is written:

$$\phi = ks \left( n - \sqrt{m^2 + 1} \right). \quad (2.19)$$

In the case of the paraxial approximation, all the trigonometric functions are linearized and  $m \approx (n - 1)s'$ . Also, if the square root is replaced by its Taylor expansion, the phase becomes

$$\phi = k(n - 1)s \left( 1 - \frac{n - 1}{2} s'^2 \right). \quad (2.20)$$

Now the wavefront aberration can be approximated by the total differential:  $\delta\phi \approx \frac{\partial\phi}{\partial s} \delta s + \frac{\partial\phi}{\partial s'} \delta s'$ . Finally, the wavefront aberration is explicitly given by

$$\delta\phi \approx k(n - 1) \left[ \left( 1 - \frac{n - 1}{2} s'^2 \right) \delta s - (n - 1) s s' \delta s' \right], \quad (2.21)$$

which is a function of the surface form deviation  $\delta s$ , of the slope deviation  $\delta s'$ , but also of the surface  $s$  and its derivative  $s'$ . In this case, the dominant term is  $k(n - 1)\delta s$ , which is nothing else than the phase change produced by a thin element of thickness  $\delta s$  [50]. This suggests that for small surface form deviations, RMSt (or RMSi if focus compensation is assumed) may be used to tolerance the surface form when the optical performance is represented by the wavefront aberration RMS.

### 2.3.3 Microlens arrays

Tolerancing a MLA is a bit different than tolerancing a single microlens. Indeed, the fabrication process produces inevitable inhomogeneities with the consequence that the forms of the microlenses are slightly different across the array. In particular, the focal lengths of the individual microlenses are different. If the system allows for focus compensation, only the average defocus can be compensated. Consequently, a tolerance has to be set to control this non-uniformity. If no compensation is available, uniformity does not need to be controlled, and all microlenses should be compared to the nominal surface.

A second inhomogeneity that appears during the MLA fabrication provokes an edge effect. It means that the surfaces of the microlenses at the MLA edge are slightly different from the rest of the array. As a manufacturer, one observes this edge effect in UV imprint and RIE techniques. This edge effect depends on different factors, for instance, on the gap between the microlenses or on their positions on the wafer. As this effect is unavoidable, a solution to attenuate its impact is to put dummy microlenses or structures outside the effective active area of the MLA.

## 2.4. Comparison between different surface form representations

Figure 2.8 presents the ROC non-uniformity within an MLA that consists of a single row of 32 spherical microlenses. Microlens parameters: diameter  $2a = 940\mu\text{m}$ ,  $R = 3845\mu\text{m}$ . Fabrication non-uniformity, as well as edge effect, can be observed. Knowing these effects helps to tolerance effectively.

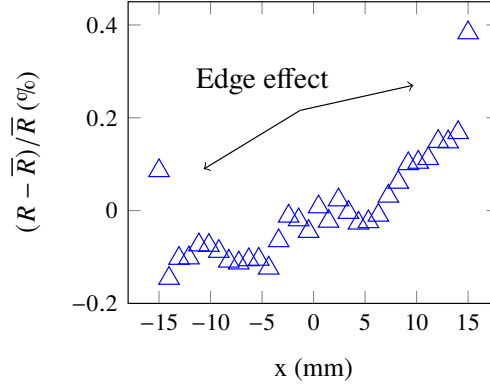


Figure 2.8 – Example of ROC non-uniformity across an MLA of 30 mm length manufactured by resist reflow and reactive ion etching. Microlens parameters: diameter  $2a = 940\mu\text{m}$ ,  $R = 3845\mu\text{m}$ . A non-random non-uniformity - average linear trend - is observed. Edge effect caused by symmetry breaking of the layout, a missing neighbor microlens, is also seen.

## 2.4 Comparison between different surface form representations

An ideal tolerancing process is a method that accepts all the elements that respect the specification on the optical performance and which rejects all the out-of-spec elements. This is, however, impossible to achieve in practice. Thus, to quantitatively evaluate the different surface form representations, which we define to be the set of parameters and surface form tolerances to which tolerances are assigned, we introduce the notion of tolerancing efficiency. We define this quantity to be the ratio of the number of elements that are within the tolerances to the number of elements that are optically in-spec. This definition makes sense only if there is, at the same time, control of the out-of-spec elements that lie within the tolerance bands (false positive). Here, we adopt the convention that consists of rejecting all out-of-spec elements.

In this section, we want to compare different surface representations; it means we want to compare their tolerancing efficiencies. To do so, we have first to establish the tolerances for the selected surface form representations. Here, we perform the process of tolerancing as follows: we first simulate a distribution of microlenses, see Section 2.2.4, that is supposed to represent well the potentially manufactured microlenses. Then, for a given surface form representation, the tolerances are found for each parameter. We restrict ourselves to finding tolerances for each parameter independently and in a symmetrical form for non zero target values (e.g.  $R \pm \Delta R$ ,  $RMS_i < \text{Threshold}, \dots$ ).

## Chapter 2. Microlens Surface Form Tolerancing

Mathematically, the problem is to determine the tolerance bands which maximize the number of accepted elements under the constraint that all elements within the tolerance bands must be optically in-spec. When the surface representation consists of a single parameter, this can easily be done by hand. However, when using multiple parameters, finding the tolerances becomes an optimization problem in a multidimensional space that may have a multitude of local optima. Global optimization methods are thus needed. Here, we use both a genetic algorithm [51] and simulated annealing [52] to find the optimal tolerances. The optimization run is done several times with both techniques to increase the chance of finding the global optimum. Any additional constraint that the manufacturer may set, for instance, a minimum tolerance of 1% on the ROC value, can directly be integrated into the global optimization process.

Then, the comparison of the different surface representations is made for the following case: the merit function is the on-axis RMS spot size of the system presented in Fig. 2.5b. Practically, a distribution of 2500 simulated microlenses is considered. Their total surface deviation RMS ranges from 0 nm to 1000 nm. First, no focus compensation is assumed. Arbitrarily, elements with a RMS spot size smaller than 15  $\mu\text{m}$  are considered to meet the optical specification.

Tolerances for selected representations are given in Table 2.2 as well as their tolerancing efficiency. The definition of the different parameters is found in Table 2.1. A first simple approach is to tolerance RMSt, but its efficiency is only 54.9%, which is the lowest in this test. Another representation with a single parameter is the total slope deviation. As shown in Section 2.3.2, this parameter is well correlated to the on-axis RMS spot size, which we consider here as our figure of merit. This is confirmed since the efficiency is 100%, which makes it the best approach for this specific case. The representation based on  $R$  and RMSi gives an efficiency of 80.9%. The approach based on the generalization of ideal asphere with additional RMSai has an efficiency of 74.0%. As expected, it should not be used in such a case. Replacing  $R$  and  $\kappa$  by defocus and using the RMS of the surface form deviation without the defocus component, RMS\*, allows for an improvement of  $\sim 9\%$ , giving an efficiency of 82.6%.

Table 2.2 – Comparison between selected approaches for tolerancing aspheric surfaces used in the setup presented in Fig. 2.5b. No focus compensation is considered. RMS\* is the RMS of the surface form deviation without the defocus component. The total slope deviation RMS, thanks to its good correlation to RMS spot size, see Eq. (2.18), has an efficiency of 100% and is the best approach.

Parameters	RMSt	RMSt $\Delta$ S	$R$ / RMSi	$R/\kappa$ / RMSai	$c_4$ / RMS*
Tolerances	< 332 nm	< 31 mrad	$\pm 41.5 \mu\text{m}$	$\pm 76.7 \mu\text{m}$	$\pm 0.56 \mu\text{m}$
			< 303 nm	$\pm 4.64$ < 242 nm	< 310 nm
Efficiency (%)	54.9	100.0	80.9	74.0	82.6



## 2.4. Comparison between different surface form representations

Some lessons can be learned from these results: firstly, RMSt is not an efficient parameter, at least when we consider microlens far from the diffraction limit. Secondly, the total slope deviation RMS is ideal for tolerancing systems whose performance is well described by the RMS spot size. Thirdly, as already mentioned, the conic constant should not be toleranced together with the ROC when no focus compensation is considered. Finally, increasing the number of parameters, for instance, from  $R/\text{RMSi}$  to  $R/\kappa/\text{RMSai}$ , does not necessarily increase the efficiency.

The same example is considered when focus compensation is assumed. We arbitrarily fix that elements with a RMS spot size smaller than  $10\text{ }\mu\text{m}$  meet the optical specification. The results are provided in Table 2.3. Most of the conclusions drawn in the case without focus compensation are also valid in this case: RMSt has a low efficiency of 45.5% and should not be used. This was expected because it is the only representation that does not take into account the degree of freedom provided by the focus compensation. The representation based on slope deviation is again the most efficient even though it has only 86.9% of efficiency this time. All remaining representations are pretty equivalent in this case and of lower efficiency.

A few more points need to be discussed: one might think that increasing the number of parameters increases the tolerancing efficiency, but this is correct only if the parameters are independent, which is incorrect for a given representation as the parameters are derived from the same fit. Also, for a high number of parameters, the tolerancing procedure becomes more complicated because of the global optimization process. Increasing the number of parameters to increase the tolerancing efficiency should thus be done very carefully.

Also, on a single wafer, microlenses do not have RMSt from 0 nm to 1000 nm, but are more condensed around a specific value. The entire wafer can be largely in-spec, and the representation choice has no real importance. It may also happen that the microlens distribution center is not far from the spec limit, and in this case, the representation choice is even more critical than in the presented example.

Table 2.3 – Comparison between selected approaches for tolerancing aspheric surfaces used in the setup presented in Fig. 2.5. Focus compensation is considered. RMS\* is the RMS of the surface form deviation without the defocus component. Again, the slope deviation based representation is the best approach even though it has no more 100% of efficiency.

Parameters	RMSt	$R / \text{RMSi}\Delta S$	$R / \text{RMSi}$	$R/\kappa / \text{RMSai}$	$c_4 / \text{RMS}^*$
Tolerances	< 237 nm	$\pm 39.1\text{ }\mu\text{m}$	$\pm 39.1\text{ }\mu\text{m}$	$\pm 45.7\text{ }\mu\text{m}$	$\pm 0.49\text{ }\mu\text{m}$
		< 18 mrad	< 233 nm	$\pm 3.34$ < 233 nm	< 233 nm
Efficiency (%)	45.5	86.9	77.1	77.6	75.9

### 2.5 Applications to real systems

The complexity of real systems comes from different features: first, from the illumination. For instance, the apodization might be non-uniform, and the incoming light may have a certain angular spectrum. On-axis considerations need thus to be generalized. It also comes from the physical model needed to propagate the light: physical optics may be required. Finally, more complex FOMs, such as the coupling efficiency into a waveguide, might also be considered.

To show the impact of such advanced considerations, we present two examples inspired by real systems. The first one, presented in Section 2.5.1, presents a microlens that couples an on-axis Gaussian beam into a single-mode fiber (SMF). The second example, found in Section 2.5.2, presents the case of an MLA that acts as a projector. It is an off-axis example.

#### 2.5.1 Fiber coupling

One major application of refractive microlenses is to couple light into waveguides and optical fibers. Aspheric microlenses can do it perfectly in theory [8]. Here, we consider a collimated Gaussian beam that is coupled into a standard single-mode fiber (Cornell SMF-28), see Fig. 2.9. The microlens is in fused silica and its geometrical properties are: diameter  $2a = 500\mu\text{m}$ , ROC  $R = 600\mu\text{m}$ , conic constant  $\kappa = -0.49$  and substrate thickness  $T = 500\mu\text{m}$ . The light wavelength  $\lambda$  is  $1.55\mu\text{m}$ . In this configuration, the optimized coupling efficiency is 95 %.

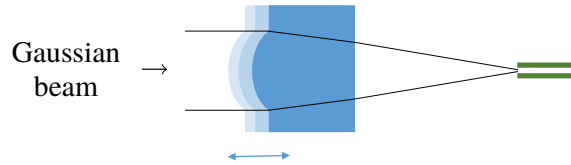


Figure 2.9 – Schematic of a collimated Gaussian beam coupled into a single-mode fiber. In order to achieve a good coupling efficiency, the microlens has to be actively aligned.

Fiber coupling imposes tight tolerances, and active focus compensation is usually performed. For this reason, we only compare representations that take into account this degree of freedom. Based on the results of Table 2.3, we consider irregularity RMS and irregular slope deviation RMS for the tolerancing. In order to go one step further, the apodization should be considered as well. For this reason, we also weight the RMS value of the surface form tolerances according to the beam apodization.

The coupling efficiency is calculated for a simulated microlens distribution, as described in Section 2.2.4. The calculation is done with the software FRED from Photon Engineering [53]. We decide to set the optical specification to be a reduction of the coupling efficiency of less than 20%. Tolerances are found according to the procedure described in Section 2.4.

The results of this tolerancing process are presented in Table 2.4. RMSi provides a better

tolerancing efficiency than RMSi $\Delta$ S in this case. For this reason, we also use this representation with a Gaussian weight. As expected, the tolerancing efficiency is increased in this case. Figure 2.10 shows how the correlation between coupling efficiency and RMSi increases when weighted according to the beam apodization.

In conclusion, for fiber coupling, a simple and efficient way to tolerance a microlens is to use the ROC and the irregularity RMS with a weight that corresponds to the beam apodization.

Table 2.4 – Comparison between selected approaches for tolerancing aspheric surfaces of microlenses used for fiber coupling, see Fig. 2.9. In this case, the RMSi gives better results than RMSi $\Delta$ S. As intuitively expected, weighting the surface form to mimic the apodization increases the tolerancing efficiency.

Parameters	$R / \text{RMSi}\Delta S$	$R / \text{RMSi}$	$R / \text{RMSi weighted}$
Tolerances	$\pm 57.2 \mu\text{m}$	$\pm 57.2 \mu\text{m}$	$\pm 52.9 \mu\text{m}$
	$< 11.7 \text{ mrad}$	$< 341 \text{ nm}$	$< 306 \text{ nm}$
Efficiency (%)	72.3	84.7	91.3

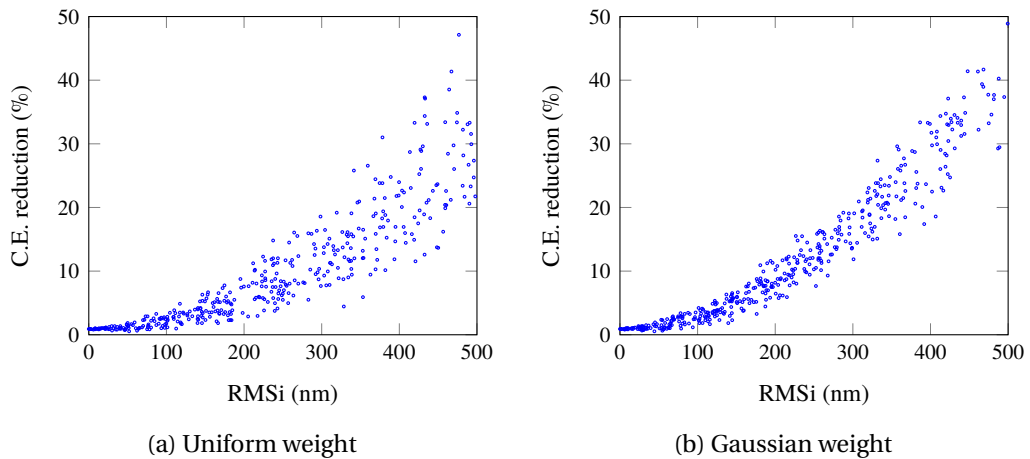


Figure 2.10 – Reduction of the coupling efficiency as a function of RMSi and weighted RMSi. With a Gaussian weight, the correlation between coupling efficiency and RMSi is increased, allowing a more efficient tolerancing process, see Table 2.4.

## 2.5.2 Micro-projector

One recent application of MLAs is pattern projection [54, 55]. The working principle is presented in Fig. 2.11. A chromium layer buried in the substrate is illuminated and imaged at infinity by a projection microlens. This operation is performed in parallel by every microlens through the MLA. The final projection is thus the sum of the single projections.

From a design and tolerancing point of view, such a system can be described using backprop-

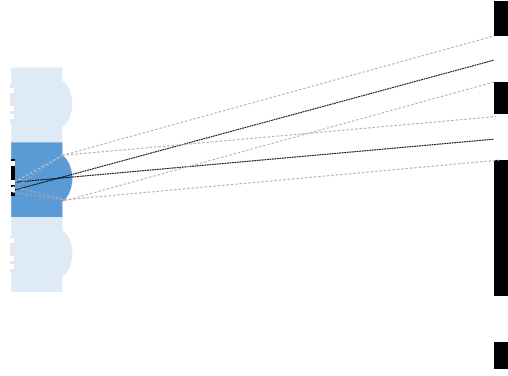


Figure 2.11 – Representation of a single channel of a micro-optical array projector. A chromium pattern buried in the substrate is imaged at infinity and can thus be projected on a screen. The final image is the superposition of the projection of all channels. Microlens properties are: diameter  $2a = 300\ \mu\text{m}$ , ROC  $R = 500\ \mu\text{m}$ , conic constant  $\kappa = -0.44$ , refractive index  $n = 1.5$  and substrate thickness  $T = 1477\ \mu\text{m}$ .

agation: the microlens is illuminated by plane waves with different angles and imaged on the chromium layer, which lies in the focal plane of the microlens. Because of the angular spectrum, the imaging is performed within a certain field of view and not only on-axis. If the angular spectrum is large, images in the field cannot be diffraction-limited, and aberrations are mainly geometrical. In this case, it is advised to take the RMS spot size as the performance metric. Practically, the merit function should be the average RMS spot size over the field of view.

For each angular component, the RMS spot size is computed with respect to the RMS spot centroid produced by the nominal surface. The system distortion is thus not taken into account. This is not a limitation for such a projection system since this distortion can be compensated in the chromium pattern design. However, such systems are not compensated for defocus due to fabrication and utilization constraints. Microlens properties are: diameter  $2a = 300\ \mu\text{m}$ , ROC  $R = 500\ \mu\text{m}$ , conic constant  $\kappa = -0.44$ , refractive index  $n = 1.5$  and substrate thickness  $T = 1477\ \mu\text{m}$ .

The average RMS spot size is computed for the simulated microlens distribution, as explained in Section 2.2.4. Here, we are interested in generalizing the results obtained for the on-axis system. For this, the average RMS spot size is compared to the total surface deviation RMS and the total slope deviation RMS. The results are presented in Fig. 2.12. As for the on-axis system, the correlation between RMSt and average RMS spot size is poor, whereas the total slope deviation RMS is extremely well correlated to the average RMS spot size.

In conclusion, these results show that the off-axis case can be handled similarly to the on-axis case. In particular, the total slope deviation RMS is also a very efficient parameter to tolerance microlens surfaces used in off-axis optical systems whose performance is well described by the RMS spot size.

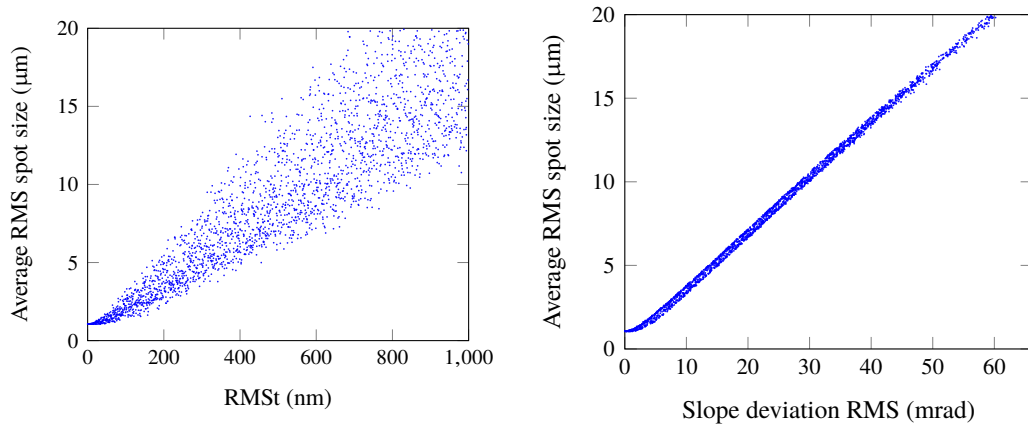


Figure 2.12 – RMS spot size averaged over the full field of view as a function of the total surface deviation RMS and of the total slope deviation RMS for the simulated distribution of surface described in Section 2.2.4. Like for the on-axis case, the correlation between the RMS spot size and the total slope deviation RMS is excellent.

## 2.6 Discussion

**Application domain of the results:** In this thesis, we focus on rotationally symmetric surfaces. However, the results of this work can be extended without problem to circular and non-circular cylindrical microlenses. Nevertheless, the useful tool that is the Zernike polynomials cannot be used anymore. Historically, because of fabrication process limitations, microlenses have been limited to spherical or conical surfaces. Nowadays, thanks to micromachining and imprint technology as well as direct writing techniques, it is also possible to manufacture freeform surfaces. Going from spherical to aspheric surfaces requires an additional parameter: the conic constant. For freeform surfaces, a high number of parameters might be required, or the surface may not even be defined by an explicit equation. In these situations, certain surface form tolerances such as irregularity are no more defined nor relevant. Also, a freeform surface has, by definition, a more complex optical function than a classical lens and cannot be reduced to a focusing element. For all these reasons, tolerancing freeform surfaces is out of the scope of this work even if some of the presented conclusions, notably that the slope deviation is an effective tolerancing parameter, could probably be applied to such complex surfaces.

**Guidelines:** Some conclusions can be drawn from the results presented in this chapter. The first one is that the parameters used for the surface design,  $R$  and  $\kappa$  in the present case, are not necessarily the best ones for tolerancing, see Fig. 2.6 and Tables 2.2 and 2.3. Indeed, the slope deviation RMS is demonstrated to be a more effective surface form tolerance in many situations and should be used.

A second lesson, as it is seen in Table 2.2, is that tolerancing the conic constant might be inefficient. This is explained by the strong correlation between  $R$  and  $\kappa$ . Moreover, the Zernike representation of the surface form deviation presented in Fig. 2.2a does not show that Zernike spherical coefficients, which represent the asphericity set by the conic constant, have larger amplitudes than any other specific coefficients. This suggests there is no reason why  $c_{11}$  or  $\kappa$  should be specifically toleranced. In conclusion, the approach of tolerancing  $R$ ,  $\kappa$ , and  $\text{RMS}_i$  should be avoided.

We have to mention that these recommendations are not specific to micro-optics. Indeed, similar conclusions have been derived for classical lenses [40, 45, 56]. This is not surprising since, in both cases, the light is mostly shaped by means of refraction.

ISO standards about surface form tolerances have not been developed or adapted for microlenses nor conical surfaces. In this chapter, we show some of the differences between micro- and classical optics and why it is difficult to use the exact ISO definitions for aspheric microlenses. The lack of standards might be an obstacle for the communication between the manufacturer and the designer as most surface form tolerances have to be redefined and clarified. We also want to stress this problem and to advocate an extension of the ISO standards to micro-optics. As the tolerances we propose here as an alternative are, however, not fundamentally different from the ISO standards, they could be the first step towards such an extension.

**Tilt and centering tolerances:** In this chapter, we focus on surface form tolerancing. However, other microlens geometrical features also influence the optical performance, and we also want to discuss them.

First, the tilt of the microlens. Because of the wafer-level fabrication techniques, there is always the substrate flat-area around a single microlens or an MLA. An implicit assumption that is motivated by the flatness of wafers is to consider this flat area as being perpendicular to the optical axis. Based on this, the tilt can be either toleranced or included in any surface form deviation. However, by looking at the Zernike representation of the surface form deviation provided in Figs. 2.2 and 2.3, the tilt is, in practice, usually negligible compared to other aberrations.

Secondly, the microlens centering. This is especially important for single microlenses that are not actively aligned or for MLAs. Particularly, this is of uttermost importance for MLAs that couple light simultaneously in multiple waveguides. Centering accuracy is dictated by the photomask for RIE microlenses, by the template for their imprint counterparts, and by the fabrication process local variation. As already mentioned in Section 2.3.3, an edge effect exists in MLA and also impacts the pitch, see Fig. 2.13. We observe that the first and last pitches have slightly different values. As already mentioned for ROC, this demonstrates the need for dummy microlenses/structures to prevent this edge effect.

A last important parameter is the thickness of the microlens substrate  $T$ . The effect of thickness variation can be evaluated by the definition of the effective back focal length,

$$f_{E,b} = \frac{R}{n-1} - \frac{T}{n}. \quad (2.22)$$

A thickness variation thus mainly provokes a focal change. Thickness tolerance should thus be coupled to a defocus tolerance, e.g. to a ROC tolerance.

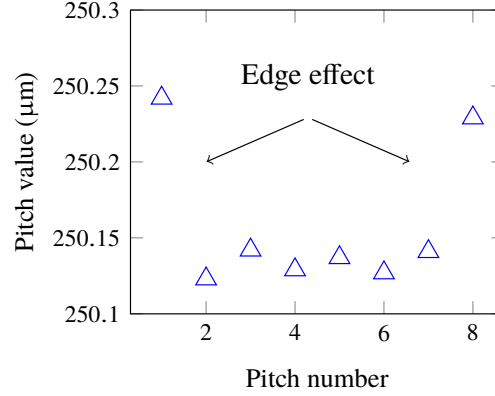


Figure 2.13 – Measured pitches within a 9 columns 1 row MLA. The microlens diameter is  $245\mu\text{m}$ , and the nominal pitch value is  $250\mu\text{m}$ , so the gap between the microlenses is  $5\mu\text{m}$ . Expanded uncertainty estimated from optical surface profiler calibration is  $\pm 0.375\text{ nm}$ . The first and last pitches are clearly larger than the other ones. This is explained by local inhomogeneity of the RIE process caused by symmetry breaking in the MLA layout.

**Tolerancing and machine learning:** Besides the challenges of surface form representation determination, and of tolerances determination, there is one more assumption that limits the effectiveness of the tolerancing procedure: the independent tolerancing of the parameters. This is highlighted for ideal aspheres without focus compensation: the problem is not the choice of the parameters  $R$  and  $\kappa$ , because, by definition, the surface is entirely defined by them, but the independent tolerancing of these parameters. As suggested, tolerancing the correct function of  $R$  and  $\kappa$  could solve this problem. However, finding such a function would be difficult in a higher-dimensional space.

A tolerancing process is nothing else than a classification problem. An efficient way to address such a problem is by using machine learning methods [57], which could take care of the challenges mentioned above: determination of an optimal surface representation and determination of the optimal decision boundaries (tolerances). By using deep learning methods, input data could be in basic shape: for instance, Zernike coefficients or even meshed surfaces, like images that feed convolutional neural networks (CNNs). In these cases, however, the set of training data has to be pretty large.

Nonetheless, approaching the tolerancing process with machine learning methods has few

drawbacks: this is non-standard, and no information can be put on a technical drawing. Moreover, the algorithm should be shared between the optical designer and the manufacturer. This poses the issue of software compatibility.

### 2.7 Conclusion

Tolerancing the surface form of an aspheric microlens is an important step towards the quality control of this microlens as its optical function is not necessarily tested. Tolerances must thus ensure the quality, but they should not be over-selective as this unnecessarily increases the fabrication cost. For this, tolerances and optical performance must be as correlated as possible. This tolerancing task is especially important for wafer-level fabrication techniques as up to tens of thousands of microlenses are processed at the same time on a single substrate without the possibility to shape the microlenses individually.

This work addresses this challenge from a practical point of view but is not an exhaustive treatment of the topic. Indeed, only a few surface tolerances are considered. We rather suggest a general approach that motivates the use of specific surface form tolerances: we analytically link the surface form and the optical performance with the help of ray optics. A perturbative formulation of the derived connection suggests the use of specific tolerances. Then, we compare these suggested tolerances with more common parameters for typical micro-optical systems, thus leading to important guidelines. In particular, we show that the slope deviation RMS should be toleranced as it has a strong correlation with the optical performance when represented by the RMS spot size. We also emphasize that the parameters used for the design, the radius of curvature and the conic constant, are not ideal for tolerancing purposes. Moreover, the conic constant should not be toleranced. In this regard, this work is more a practical extension and an adjustment of ISO 10110-5 developed for classical lens surfaces rather than a completely new approach. However, we believe that the guidelines proposed here should help any optical designer in the task of tolerancing the surface form of the microlens they request.

In the future, this work could be extended by including new tolerance parameters, other optical figures of merit, and other types of surfaces. For instance, one could also consider the Peak-to-Valley value of the different deviations as tolerance parameters. We could also represent the optical performance not only by a single number but by a function, for instance, the modulation transfer function. Finally, we could consider more advanced surfaces such as freeform microlenses that can now be manufactured by direct writing techniques.



## 3 Microlens Surface Measurement

Measuring the surface of microlenses by optical surface profilers is the prominent way to characterize microlenses. Indeed, this allows for quality assessment and feedback for process optimization. However, the measurement accuracy is reduced by errors in the measurement, limiting the achievable microlens quality. In this chapter, we study these errors and propose methods to correct them.

### 3.1 Introduction

The key element of a refractive microlens is its curved surface, usually spherical or aspheric, where the light refraction occurs. Measuring and characterizing the form of such surfaces is of central importance for two reasons. Firstly, it provides the necessary piece of information for the manufacturer to optimize the fabrication process. Secondly, it allows us to assess the optical performance of the microlens. Even if the microlens quality can be evaluated by different optical techniques [35, 36, 58], its assessment by surface measurements has several significant advantages: first, commercial instruments that are easy to use and can be fully automated for wafer-level optics are available. Moreover, the measurements are quite fast, and the measuring instrument configuration does not depend on the microlens geometry (focal length and asphericity). Measuring the surface is also quite insensitive to the microlens material because no signal is transmitted through the microlens, allowing to characterize polymer, glass, and particularly silicon microlenses that are not transparent in the visible range. For all these reasons, surface measurement is at the heart of the microlens metrology and is thus of great importance for micro-optics manufacturers.

The instruments available to measure microlenses surfaces can be sorted in two categories: on the one hand, there are the 2D contact probe surface profilers such as the mechanical stylus. On the other hand, there are the areal surface texture measuring instruments that allow recording the full 3D surface topography. Even though aspheric microlenses have a rotationally surface, the surface form deviation is not always symmetrical, and knowledge of the full surface is thus desirable. Since 2D surface profilers need multiple scans to achieve this

task, the measurement time is larger compared to 3D surface measuring instruments and thus less suited for a high volume production environment.

Among the 3D surface measuring instruments, two of them are especially suited for microlens surface measurements: the confocal microscope [59, 60] and the coherence scanning interferometer (CSI) [61, 62]. Typical configurations of these instruments are presented in Fig. 3.1 and Fig. 3.2. They possess a vertical nanometric resolution and can measure a few microlenses per minute. Also, these technologies are well established, and many instruments are commercially available.

Even if CSIs and confocal microscopes are quite similar in terms of performance, two differences are essential for microlens surface measurements. Firstly, the vertical resolution of CSI is independent of the microscope objective NA and can be subnanometric. On the other hand, the vertical resolution increases with the NA for confocal microscopes and generally reaches 1 nm only for the highest NAs, thus the highest magnifications. The second difference is the type of microscope objectives that can be used. A CSI requires interferometric objectives, and for a given magnification, the NA is generally smaller than the confocal microscope equivalence, see Fig. 3.3. From these facts, flat lenses are better resolved by CSIs, but when the microlens surface is steep, confocal microscopes are superior.

As just mentioned, the main limitation of 3D surface microscopes is their limited capability in terms of size and slope. When the surface starts to be too steep, microscope objectives with a higher NA must be used but with the drawback of a field of view (FOV) reduction. Image stitching may thus be needed. This operation is reasonably implementable only when few images have to be stitched together. Otherwise, the measurement becomes dramatically long. Beyond this limit, the use of contact probe profilers with multiple scans becomes the best alternative.

In this chapter, we discuss the measurement of microlens surface by CSIs and confocal microscopes and particularly the accuracy of such measurements. First, we discuss the ideal geometrical model of such instruments and its typical calibration. In a second time, we show that a surface error appears when non-flat surfaces are measured. This error can be larger than the surface deviation tolerance, thus making impossible the use of such measurements to characterize microlenses. Consequently, we discuss the extension of the original model and propose a new calibration procedure that allows us to correct this error.

Throughout the discussion, we also calculate the uncertainties of the different measured parameters. All the calculations are done following the rules of the *Guide to the expression of uncertainty in measurement* [63] and of the related documents [64–67], which are the reference documents on this topic.

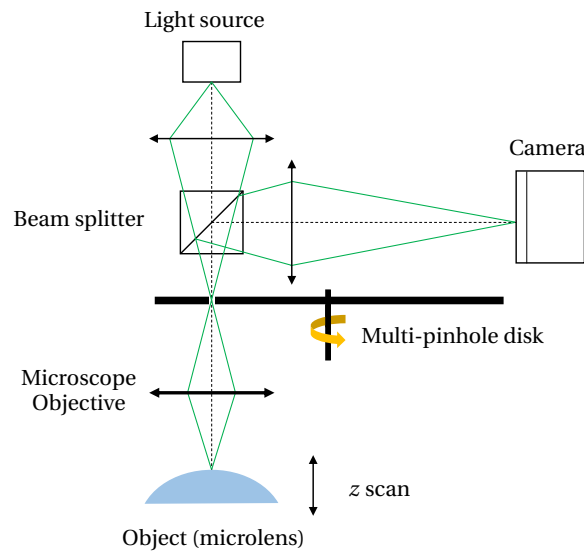


Figure 3.1 – Simplified schematic of the confocal microscope  $\mu$ surf as presented by the manufacturer Nanofocus: a microscopic object is illuminated and imaged by a microscope objective on a camera. Due to the multi-pinhole disk, only the reflected light that is in focus reaches the camera. Consequently, images taken at different vertical positions allow extracting the vertical position of the surface accurately.

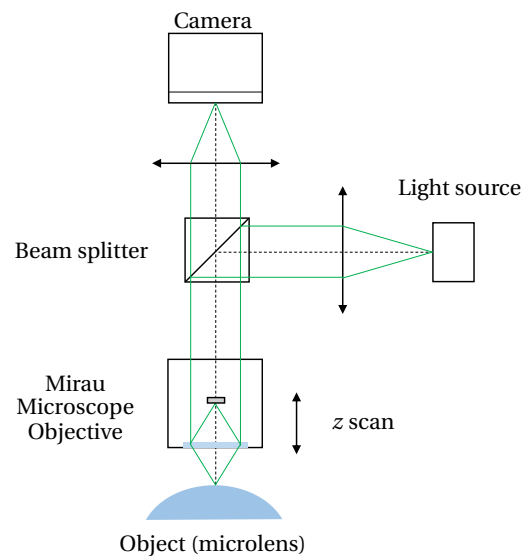


Figure 3.2 – Simplified schematic of the coherence scanning interferometer Nexview as presented by the manufacturer Zygo: a microscopic object is illuminated and imaged by an interferometric microscope objective on a camera. Due to the light source partial coherence, the reflected light that is in focus coincides with the highest contrast fringe. Consequently, images taken at different vertical positions allow extracting the vertical position of the surface accurately.

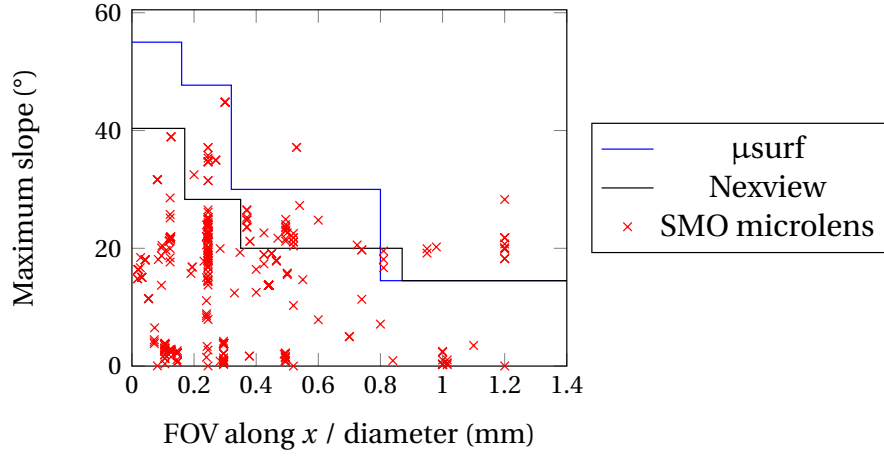


Figure 3.3 – Maximum slope that can be measured using specular reflection on an optically smooth surface as a function of the  $x$  dimension of the FOV for the confocal microscope  $\mu$ surf and the CSI Nexview. These values are derived from the NA of the microscope objectives. In reality, the measurable maximum slope is reduced by different factors, notably the signal-to-noise ratio. However, this shows that the confocal microscope  $\mu$ surf is capable of measuring a wider parameters range without using image stitching. Parameters of typical microlenses produced at SUSS MicroOptics (SMO) are presented.

This chapter is organized as follows: in Section 3.2, we discuss the calibration of the ideal model of confocal microscopes and CSIs as well as the resulting expected accuracy. In Section 3.3, it is shown that this original ideal model is not sufficient to describe the measurements accurately as errors appear in particular situations. We also discuss the already proposed approaches to correct these errors and explain why we believe none of them can be directly applied for the characterization of microlenses. Consequently, in Section 3.4, a model to calibrate the instrument and to avoid the error in spherical surface measurement is proposed. We use it for the measurement of different reference balls as well as for one aspheric surface. In Section 3.5, we consider another type of error that arises in CSI measurements, which we name phase jumps. We propose a method to correct this phase jumps error for microlens surface measurements. Finally, we provide a summary of this chapter in Section 3.6.

## 3.2 Geometrical model of optical surface profilers

Even though these two techniques, confocal microscopy and coherence scanning interferometry, are different, the basic model that describes them is identical. Ideally, it is possible to consider both of them as instruments that record ideal 2D geometrical images at different vertical positions. A mechanical driver determines the positions of these images. Usually, a piezo actuator is used to perform vertical scanning. In this model and for a confocal microscope, the intensity recorded as a function of the  $z$ -position consists of a delta Dirac function, the non-null value corresponding to the surface height. For a CSI, the intensity as a function of

the  $z$ -position presents fringes, the most visible one corresponding to the surface height. For an ideal system, only two parameters must be defined: the lateral scaling, which is nothing else than the magnification  $M$ , and the vertical scaling. Most utilization of these instruments relies on this idealized model with a small correction for flat surfaces, i.e., the residual flatness correction described in Section 3.3.

#### 3.2.1 Standard calibration and uncertainty

In order to use this ideal model, at least two calibrations must be performed [68]: firstly, the calibration of the magnification (also called field amplification coefficient) of the imaging system (microscope objective plus an eventual zoom lens), which links the coordinates of the image plane (the camera sensor)  $(\chi, \zeta)$  to the object plane  $(x, y)$  (the sample). This link is written as:

$$x = \frac{\chi}{M} \text{ and } y = \frac{\zeta}{M}. \quad (3.1)$$

Secondly, the calibration of the vertical amplification coefficient  $\alpha_z$ , which links the measured height  $z_m$  to the actual height  $z$ :

$$z = \alpha_z z_m. \quad (3.2)$$

When the instrument is not calibrated, it is possible to rewrite the parameters as follow:

$$M' = M + \delta M = M \left( 1 + \frac{\delta M}{M} \right) := M c_M \text{ and } \alpha'_z = \alpha_z + \delta \alpha_z = \alpha_z \left( 1 + \frac{\delta \alpha_z}{\alpha_z} \right) := \alpha_z c_{\alpha_z}. \quad (3.3)$$

This leads to the definition of non-calibrated coordinates,

$$x' = c_M x, \quad y' = c_M y \text{ and } z' = c_{\alpha_z} z. \quad (3.4)$$

The coefficients  $c_M$  and  $c_{\alpha_z}$  are by definition 1 when the instrument is correctly calibrated. When measured with a non-calibrated instrument, an aspheric surface,

$$z = \frac{r^2}{R \left( 1 + \sqrt{1 - (1 + \kappa) r^2 / R^2} \right)}, \quad (3.5)$$

becomes

$$z' = \frac{c_{\alpha_z}}{c_M^2} \frac{r'^2}{R \left( 1 + \sqrt{1 - \frac{(1 + \kappa)}{c_M^2} r'^2 / R^2} \right)}, \quad (3.6)$$

which is also the equation of an asphere with a ROC  $R'$  and a conic constant  $\kappa'$ . By identifica-

tion, one finds:

$$R' = \frac{c_M^2}{c_{\alpha_z}} R := \gamma R \text{ and } \kappa' = \frac{c_{\alpha_z}^2}{c_M^2} (1 + \kappa) - 1. \quad (3.7)$$

These relations can be used to determine the uncertainty of the aspheric surface parameters induced by the instrument calibration. The uncertainties of both coefficients are deduced from the standards used for the calibration. The pitch reference standard used here is the model NIST SRM 476 / BC-E-023-1-E-5, which gives a standard uncertainty  $u_{c_M} = 0.067\%$ . As step height standard, a SHS-76.0 Q is used and provides a standard uncertainty  $u_{c_\alpha} = 0.23\%$ <sup>1</sup>.

The uncertainty of the ROC is given by following the rules of the Guide to the Expression of Uncertainty in Measurement [63]. One finds:

$$u_R = R \sqrt{4u_{c_M}^2 + u_{c_\alpha}^2} = 0.0025R, \quad (3.8)$$

i.e. 0.25%. For comparison, typical ROC tolerance that is received from the optical designer is about 3%. Likewise, the conic constant uncertainty is given by:

$$u_\kappa = 2(1 + \kappa) \sqrt{u_{c_M}^2 + u_{c_\alpha}^2} = 0.0048(1 + \kappa). \quad (3.9)$$

This derivation is valid only within the considered ideal model and when both the ROC and the conic constant are parameters of the surface determined from the measurement by a least-square regression. When the conic constant is not a fit variable anymore, an additional uncertainty has to be considered for the ROC, which is the part of the conic constant uncertainty that is transferred to the ROC. Indeed, these two parameters are not independent. This additional uncertainty can be evaluated using Eq. (2.12):

$$\delta R = \frac{3a^2 R}{\frac{140}{15} R^2 + 9(1 + \kappa) a^2} \delta \kappa. \quad (3.10)$$

In this case,  $u_R$  becomes a function of the diameter  $2a$  and of the conic constant  $\kappa$ .

#### 3.2.2 Reference balls and the random ball test

Another calibration artifact that may be used for the calibration is reference balls. Many suppliers exist, and the ball quality is defined in a standard from the Deutsches Institut für Normung (DIN) [69]. When considering balls from the best class (G3), the Peak-to-Valley (PV) deviation from the perfect shape is  $< 80$  nm, and the surface roughness is  $< 10$  nm. It is also possible to make these balls certified by national institutes of metrology.

The key point is that the relative uncertainty of the ball diameter is smaller in comparison with

---

<sup>1</sup>  $u_{c_{\alpha_z}}$  is replaced by  $u_{c_\alpha}$  to lighten the notation

the relative uncertainties of the other standards previously mentioned. Indeed, the expanded uncertainty (95% confidence) is  $0.2\mu\text{m}$  for a ball diameter of  $2000\mu\text{m}$ , meaning a relative standard uncertainty of  $0.005\%$ , which is  $> 50\times$  better than the uncertainty value given in Eq. (3.8). However, it is not possible to use this value when measuring the surface locally with an optical surface profiler. Indeed, the ball is not perfectly round, and thus the local ROC deviates from the diameter half value.

The close geometry of balls allows us to solve this problem. The surface of a ball can be described as an ideal sphere with a small perturbation expressed in spherical harmonics [70]. In spherical coordinates, the surface is written:

$$\tilde{r}(\theta, \phi) = \tilde{r}_0 + \sum_{l,m} Y_l^m(\theta, \phi), \quad (3.11)$$

with  $\tilde{r}$ ,  $\theta$  and  $\phi$  the spherical coordinates as commonly defined, and  $Y_l^m$  a given spherical harmonic of degree  $l$  and order  $m$ . The average radial distance  $\tilde{r}_0$  is defined by:

$$\tilde{r}_0 = \frac{1}{4\pi} \int_S \tilde{r}(\theta, \phi) d\Omega, \quad (3.12)$$

with  $S$  being the surface of the ball. Consequently, the integral of the spherical harmonics expansion vanishes:

$$\int_S \left( \sum_{l,m} Y_l^m(\theta, \phi) \right) d\Omega = 0. \quad (3.13)$$

In other words, if the ball surface is measured locally at different positions, the average of the measurements converges towards a perfectly spherical surface. Moreover, the ROC of this average surface converges towards half the ball diameter, which is known with high accuracy. This process, known under the name of a random ball test, can thus be used to calibrate the instrument. It is also used in spherical surfaces testing by interferometry in the null configuration to suppress the wavefront error caused by the reference ball surface [71, 72].

In principle, using a random ball test to obtain the measurement of a reference surface known with high accuracy allow us to calibrate both the magnification and the amplification coefficients. For this, the ROC and the conic constant of this reference surface must be determined, and thanks to Eq. (3.7), calibration coefficients may be retrieved. However, the uncertainty of the conic constant by the common calibration method is only  $0.0048$ . For the measurement of a  $1000\mu\text{m}$  ROC ball over a diameter of  $300\mu\text{m}$ , this uncertainty represents a vertical difference of  $0.3\text{ nm}$ , which is smaller than any instrument resolution. Consequently, the second part of Eq. (3.7) cannot be used, and only the ROC is useful for the calibration. For this reason, we focus on determining the coefficient  $\gamma = R'/R$  from the random ball test.

In practice, the integration step in Eq. (3.13) is approximated by a finite number of surface measurements, with a finite spatial extent. This approximation adds a supplementary uncertainty that we want to assess. To do so, the ROC is calculated for each local measurement and considered as a random variable. Indeed, the location where the ROC is measured is randomly

chosen. Then, the distribution mean,  $\bar{R}$ , is determined, and its uncertainty is assessed by the central limit theorem. The ROC calculation from a measurement is a non-linear operation, and the average ROC does not exactly converge towards  $\tilde{r}_0$ . However, since the deviation from a perfect sphere is very small, this shift is negligible. We demonstrate this fact by simulation later in this section.

As a practical illustration, we consider surface measurements of a 1000  $\mu\text{m}$  ROC ball performed by the CSI Nexview equipped with a 50 $\times$  microscope objective and a zoom lens 0.5 $\times$ . Each measured spherical surface is cropped on a diameter of 300  $\mu\text{m}$  and the ROC is determined by a least-squares fit.

To attribute a probability distribution to  $R$ , we simulate the measurement process: this consists of creating a ball with a deviation of  $\sim 80$  nm by using the 50 first spherical harmonics. The coefficients are determined randomly and normalized to obtain the desired roundness deviation. Then, the ball surface is measured at 5000 randomly chosen locations, and the ROC is determined by a fit. Figure 3.4 shows the obtained distribution. It looks like a Normal distribution, even though it does not perfectly match. However, this is of no concern because the only necessary condition to apply the central limit theorem is the existence of a value for the standard deviation. In this simulation, the average ROC  $\bar{R}$  is 1000.0047  $\mu\text{m}$ , which confirms that  $\bar{R}$  converges towards  $\tilde{r}_0$ , at least with sufficient accuracy for our purpose.

The same operation is done experimentally. The distribution for 50 trials is presented in Fig. 3.5. The average radius  $\bar{R}$  is 1000.56  $\mu\text{m}$  and the sample standard deviation  $\sigma = 0.23$   $\mu\text{m}$ . However, this distribution does not originate only from the surface. It also contains the repeatability of the measurement process. In order to access it, the surface ball is measured 100 times in a row at the same location. The sample standard deviation  $\sigma$  is found to be 0.17  $\mu\text{m}$ . Under the

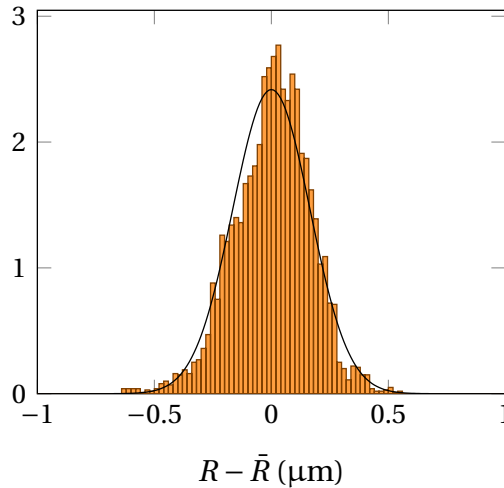


Figure 3.4 – Empirical probability density function of  $R$  based on 5000 simulated measurements:  $\bar{R} = 1000.0047$   $\mu\text{m}$  and  $\sigma = 0.16$   $\mu\text{m}$ . The measured ROC  $R$  can be modeled by a random variable with a Normal distribution (black line) defined with the sample average and variance.



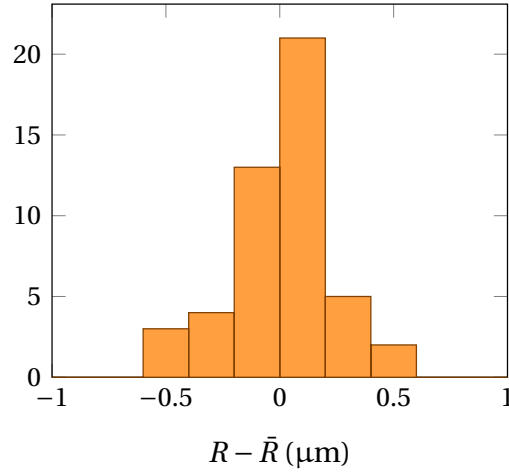


Figure 3.5 – Empirical probability density function of  $R$  based on 50 experimental trials:  $\bar{R} = 1000.56 \mu\text{m}$  and  $\sigma = 0.23 \mu\text{m}$ .

assumption of independence, the standard deviation of the  $R$  distribution is given by

$$\sigma = \sqrt{0.23^2 - 0.17^2} = 0.15 \mu\text{m}, \quad (3.14)$$

which is close to the value provided by the simulation. This shows that the modeling of the surface deviation by spherical harmonics represents well the reality. However, it has to be mentioned that these values are valid for a given measurement instrument, a ball with a given ROC, and a given diameter.

Knowing the standard deviation, it becomes possible to calculate the uncertainty of  $\bar{R}$  by using the central limit theorem. With 50 trials, one finds  $u_{\bar{R}} = 0.15/\sqrt{50} = 0.02 \mu\text{m}$ . This uncertainty has to be combined with the uncertainty coming from  $\kappa$ ,  $u_{R(\kappa)} = 0.02 \mu\text{m}$ , and with the uncertainty of the diameter  $u_{\bar{r}_0} = 0.05 \mu\text{m}$  provided by the certification. Finally, the combined uncertainty of  $R$  is:

$$u_R = \sqrt{0.02^2 + 0.05^2 + 0.02^2} = 0.06 \mu\text{m}. \quad (3.15)$$

This represents an extended uncertainty of 0.012% at a 95% confidence level. We recall that this value is the uncertainty of the ROC value of the reference ball.

Finally, the goal is to adjust the calibration parameters, for the magnification  $c_M$  and for the amplification coefficient  $c_\alpha$ , based on this procedure. However, how to modify them based only on the value of  $\gamma$ ? We note that the uncertainty of  $c_\alpha$  is larger than the uncertainty of  $c_M$  and  $\gamma$ . Consequently, we propose to use  $c_M$  and  $\gamma$  for the calibration and to use Equation (3.7)

to determine  $c_\alpha$  with lower uncertainty. This reads,

$$\frac{u_{c_\alpha}}{c_\alpha} = \sqrt{u_\gamma^2 + 2 \left( \frac{u_{c_M}}{c_M} \right)^2} = 0.11\%, \quad (3.16)$$

which is an improvement by a factor  $> 2$  for the amplification coefficient determination.

To summarize, it is possible to measure the ROC of spherical surfaces with an expanded uncertainty (95% confidence) of 0.012% by using a random ball test compared to 0.5% with the common calibration procedure. However, this is done under the assumption that the simple geometrical model is valid. Intuitively, this model is only an approximation of reality, and a more sophisticated model that takes into account perturbations is needed. Consequently, in reality, the uncertainties of ROC measurements are likely higher.

### 3.3 Advanced models of optical surface profilers

A real optical surface measuring instrument is a complex imaging system, and its modeling by ideal geometrical optics is likely not sufficient to explain its behavior. The measurement of a reference flat surface illustrates this fact as it does not appear flat [73]. For this surface, it is possible to correct the error by measuring a reference flat mirror. Thanks to its quality, it is usually made of silicon carbide, the residual from the flat is considered to be an error of the measurement system. It is thus recorded and subtracted in subsequent measurements. This calibration procedure can be seen as a null test for flat surfaces. This operation is called residual flatness correction or calibration and is part of ISO 25178-607 [59].

Such an approach is quite empirical as the causes of the error are not investigated nor modeled. For this reason, it is very unlikely that this calibration removes the error in other surface measurements. Indeed, as in any null test, a reference surface is needed for every different surface geometry.

Similar errors are found in optical testing by interferometry. In this case, these errors are called retrace errors, and different methods exist to correct them in the non-null test configuration [74, 75]. However, the considered interferometers are systems devoid of microscope objectives and of scanning mechanisms, thus rendering these correction methods meaningless in our case.

What we call *error*, *height error*, or *surface error* in this context, is nothing else than the behavior of the measuring instrument that cannot be explained by the ideal geometrical model. To address this problem, we propose a generalization based on two additional features:

1. Physical optics: a real imaging system, even if perfect, undergoes diffraction, and thus an image of a point source is not a point but has an inevitable spread in all three dimensions. The imaging process may thus be described by a 3D point spread function.

2. Aberrations: a real imaging system is never perfect and contains aberrations.

When taking these two features into account, the image formation process, as well as the surface height derivation, becomes difficult to model. Some works have been published, notably by taking a linear filtering operation approach [76–80]. However, the assumption that the PSF of the imaging system is identical throughout the FOV (shift invariance) is required. As a side note, this assumption is correct for on-axis imaging systems that obtain areal information by scanning in all three directions  $x, y, z$ . However, for the systems we consider here, this assumption is not valid, especially for high NA microscope objectives or when the field curvature is not corrected [81].

Moreover, distortion in the imaging system is not considered even though it is clear that distortion also produces a surface error. It is possible to correct it by using many different techniques [82, 83]. However, these methods assume the distortion to be constant. When measuring slopes, the backscattered rays do not fill the entire objective lens pupil, and the distortion might thus slightly change compared to the flat surface case. Hence, the distortion is expected to also depend on the measured object.

To illustrate the problem, Fig. 3.6 presents the surface error of two tilted mirror measurements by the confocal microscope  $\mu\text{surf}$  by Nanofocus. A shift-invariant PSF cannot explain this error since the surface is itself shift-invariant. Indeed, the  $z$  difference between two positions of a tilted plane surface is only a function of the distance between them, not of their locations in the FOV. Because the shape of the surface residual is different for the two tilts, a distortion cannot explain it either.

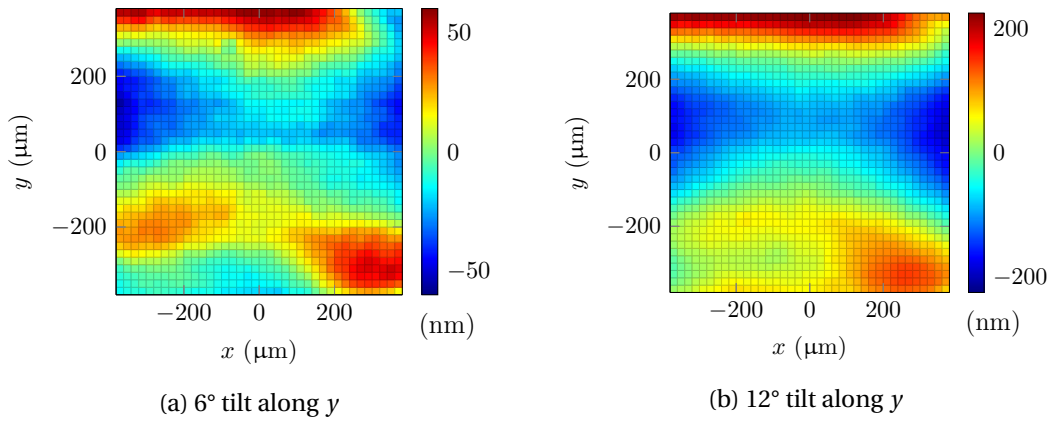


Figure 3.6 – The surface error of a tilted reference mirror measurement performed by a confocal microscope equipped with a  $20\times$  NA 0.6 microscope objective. An aberrated shift-invariant PSF does not provoke any surface error in this case because the surface is also shift-invariant. Either distortion has to be considered, or shift-invariance rejected. Moreover, because the shape of the surface error is different for the two tilts, a fixed distortion alone cannot explain these errors.

When the assumption of shift-invariance is abandoned, a model of the system becomes even more complex and has to be developed. In order to avoid such complexity, empirical approaches could be considered. Firstly, we can consider null tests. If a spherical microlens has to be measured, the surface error can be assessed by measuring a reference ball with the same ROC. A random ball test can be used to increase the accuracy of the method [84]. As for every null test, the drawback is to obtain a reference. For instance, reference balls can only be obtained for discrete ROCs. This is even more problematic for aspheric surfaces. A first but rough approach is to use the closest reference ball in terms of surface deviation to get the surface error and then subtract it from the considered asphere. However, the error can only be partially corrected.

Another empirical approach based on the recording of the error as a function of the surface slope has been published by Sensofar Tech SL, another manufacturer of confocal microscope [85]. However, in this work, only surfaces with slopes below  $10^\circ$  are considered, and the demonstrated accuracy after correction does not reach the required level for high-quality microlens fabrication. Indeed, to manufacture diffraction-limited microlenses, surface deviations RMS in the order of 50 nm have to be measured [86]. The exact value depends on the microlens material and on the operation wavelength.

For all the reasons mentioned above, we propose our model, in which we make no assumption about the properties of the system, such as shift-invariance or what kind of aberration it contains.

#### 3.4 Local plane surface approximation model

The model we propose is based on one assumption: the surface of the measured object can be locally approximated by planes. This approximation is motivated by the following assumption: the spatial extension of the imaging system PSF and the distortion are in the range of a few microns. It means that within this range, any surface  $s = z(x, y)$  with a radius of curvature of several hundreds of microns can be approximated by planes. In other words, this assumption allows the surface error  $\epsilon$  to be seen as a function of the surface gradient and of the position within the FOV::

$$\epsilon = \epsilon \left( x, y, \frac{\partial s}{\partial x}, \frac{\partial s}{\partial y} \right). \quad (3.17)$$

This approximation is illustrated in Fig. 3.7 and is similar to the one done in wave-optics propagation known as the local plane interface approximation [87].

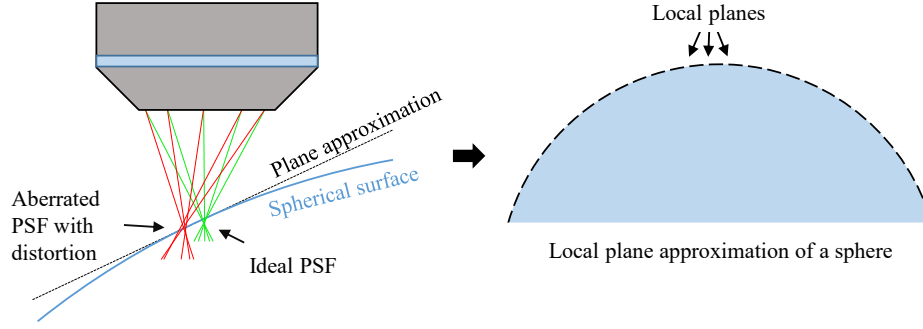


Figure 3.7 – Illustration of the local plane approximation made in this work. On the left, it can be seen that an aberrated PSF with distortion provokes almost the same error for the spherical surface or for the plane approximation thanks to the small surface curvature. In other words, the effect of the surface curvature on the light-surface interaction is neglected. An example of a local plane approximation for a sphere is presented on the right.

#### 3.4.1 Calibration

Since this model aims to correct the deviation from the ideal geometrical model, the calibration procedure consists of recording the error function and of subtracting it. Before performing this, the instrument must already be calibrated, as discussed in Section 3.2. Then, the error function is determined experimentally for all angles within the accessible NA and positions within the FOV. In this regard, it is a generalization of the residual flatness correction to slopes above  $0^\circ$ .

In order to record the error  $\epsilon$ , one intuitive idea would be to measure tilted reference planes and take the deviation from the best plane fit as the error. Although this approach is quite difficult to implement in practice because tilting the mirror takes time and presents the risk to crash the microscope objective into the sample, this approach does not work for more fundamental reasons. To show this, we start by remarking that the measurement of a tilted plane can be expressed by

$$z = c_x x + c_y y + z_0 + \epsilon(x, y), \quad (3.18)$$

with  $\epsilon$  the height error produced by the measuring instrument in this specific measurement,  $z_0$  a general offset and  $c_x, c_y$  the coefficients of the plane equation. The error can be rewritten:

$$\epsilon(x, y) = \epsilon_0 + \epsilon_1^x x + \epsilon_1^y y + \epsilon_2(x, y), \quad (3.19)$$

with  $\epsilon_0 = S^{-1} \int_S dx dy \epsilon(x, y)$ . When the measurement is fitted by the plane equation the measured height can be rewritten:

$$z = c'_x x + c'_y y + z'_0 + \rho(x, y), \quad (3.20)$$

with  $\rho(x, y)$  the best plane fit residual. By definition of least square fit,  $\int_S dx dy \rho(x, y) = 0$ .

### Chapter 3. Microlens Surface Measurement

---

Thus, by comparing the terms,

$$\rho(x, y) = \epsilon_2(x, y), \quad (3.21)$$

which shows that the best plane fit residual gives access only to the non-constant and non-linear part of the error. If the exact tilt of the plane would be known by any technical means, in other words, if  $c_x$  and  $c_y$  are known, then the residual would be  $\rho = \epsilon - \epsilon_0$ . First, this means that the tilt provoked by the error should be detectable, and likely no mechanical actuator can provide this accuracy. Secondly, the average value of the error is still missing. We believe this derivation demonstrates that this approach cannot be used to record the height error function  $\epsilon = \epsilon(x, y, \partial s / \partial x, \partial s / \partial y)$ .

Consequently, we propose a different approach to record the height error: using a reference ball instead of plane surfaces. Indeed, it is sufficient to move it throughout the FOV to obtain the different angles for all positions, when its ROC is well chosen. Practically this is easily performed since CSIs and confocal microscopes may be equipped with a xy-stage that can be automated.

The measurement of the ball surface when the ball is placed at a position  $(x_0, y_0)$  provides a spherical cap described by the equation:

$$z(x, y) = R - \sqrt{R^2 - ((x - x_0)^2 + (y - y_0)^2)} + \epsilon(x, y). \quad (3.22)$$

Since the ROC of the ball is assumed to be known with a very high accuracy, which can be achieved through a random ball test as mentioned in Section 3.2.2, the best sphere fit has only three parameters that are the position of the top of the ball  $x_0, y_0, z_0$ . When the measurement is fitted, it can be rewritten as:

$$z(x, y) = R - \sqrt{R^2 - ((x - x_0)^2 + (y - y_0)^2)} + z_0 + \rho(x, y). \quad (3.23)$$

Here, we actually make an assumption: since the position of the ball is not known and thus fitted, the error will slightly modify  $x_0$  and  $y_0$ . Consequently, they are not the same variable in the two previous equations. However, we assume that the difference between these two quantities is very small and that the error is almost constant on the scale of this difference. These two assumptions are necessary to record the error and can be validated at the end of the correction process.

Under these assumptions and by identification, the error can finally be written:

$$\epsilon(x, y) = z_0 + \rho(x, y). \quad (3.24)$$

To determine the unknown offset  $z_0$ , we remember that a flat surface presents no error when

### 3.4. Local plane surface approximation model

residual flatness calibration has been performed. In other words,  $\epsilon(x_0, y_0) = 0$ , which leads to :

$$z_0 = -\rho(x_0, y_0), \quad (3.25)$$

and to the final expression for the error:

$$\epsilon(x, y) = \rho(x, y) - \rho(x_0, y_0). \quad (3.26)$$

The slope for each position is simply found by the analytical expression of the sphere derivative, explicitly:

$$\frac{\partial z}{\partial x}(x, y) = \frac{x}{\sqrt{R^2 - (x^2 + y^2)}} \quad (3.27)$$

and likewise for the slope along  $y$ .

#### Practical recording of the error function

To illustrate this correction method, measurements performed by the confocal microscope  $\mu\text{surf}$  custom from Nanofocus are evaluated. In particular, we choose the  $20\times$  NA 0.6 microscope objective. This microscope objective is chosen because it extends the measurement capability compared to the CSI Nexview as seen in Fig. 3.3 and is thus an essential configuration for the production of microlenses. The instrument is already calibrated according to the standard procedure: calibration of the magnification, of the vertical amplification coefficient, and correction of the residual flatness.

The choice of the reference ball to record the surface error is based on dimensional considerations: the field of view when using the  $20\times$  NA 0.6 microscope objective under consideration is  $800\mu\text{m} \times 800\mu\text{m}$ . The maximum measurable slope is  $36^\circ$ , but, because of noise, the limit is fixed at  $25^\circ$ . Therefore, balls with a ROC value  $R = 400\mu\text{m}$  can be measured only on a diameter of  $320\mu\text{m}$ , which corresponds to the FOV of the  $50\times$  microscope objective. In this case, this larger magnification has to be used as it gives a better signal to noise ratio due to its higher NA. The ROC range considered in this work is thus  $R > 400\mu\text{m}$ . This motivates the choice of the  $550\mu\text{m}$  ROC ball to record the surface error.

In order to record the height error, the reference ball is measured at 961 locations within the field of view. These positions are arranged on a grid whose pitch is  $25\mu\text{m}$ . This operation takes about 6 h, which is an overnight process, but this has to be done only once for a given microscope objective.

In the confocal microscope  $\mu\text{surf}$ , confocal images are created with the help of a multi-pinhole rotating disk and are recorded on a camera. Since images consist of  $512 \times 512$  pixels, the surface error function  $\epsilon$  is obtained for more than  $2.5 \cdot 10^8$  observations from the 961 measurements. To simplify the data processing, we only consider surface slopes that have a component exclusively along the gradient  $\partial s / \partial \tilde{r}$ , with  $\tilde{r} = (x^2 + y^2)^{\frac{1}{2}}$  the radial distance defined with

respect to the FOV center. This simplification is relevant since spherical objects are usually positioned at the center of the FOV. This placement is ensured by noting that the reflected light in confocal mode describes a circle on the spherical surface in focus, thus allowing to manually position the circle center at the FOV center with high accuracy. This simplification can nevertheless be suppressed without difficulty. With this simplification, the dataset is reduced to a design matrix of dimension  $2.3 \cdot 10^5$ -by-4. Figure 3.8 shows the surface error as a function of the slope, which is analytically derived from the spherical equation, for the different recorded positions  $x$  and  $y$ .

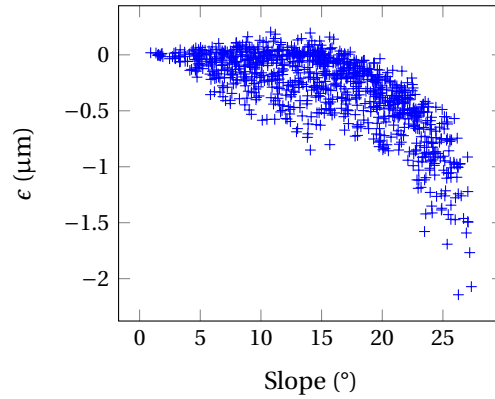


Figure 3.8 – Measured surface error  $\epsilon$  as a function of the radial slope. The error amplitude is mainly proportional to the slope. However, multiple values of  $\epsilon$  for a given slope value means that the error is also a function of the location within the FOV.

#### Regression with neural networks

This dataset is used to correct subsequent measurements that consist of  $< 2.5 \cdot 10^5$  pixels. Since frames are corrected pixel by pixel, a lookup table approach to calculate the surface error of a single measurement would render the correction procedure too slow to be practical. An alternative approach is to perform a regression of the function  $\epsilon = \epsilon(x, y, \partial s / \partial r)$  with a neural network [88].

This task is performed using the Neural Net Fitting app included in the Deep Learning toolbox of Matlab. The feed-forward neural network has a single hidden layer which contains a chosen number of neurons equal to 50. 70% of the dataset is used for the training, 15% for the validation, and 15% for the testing. The data partitioning is realized randomly. The training step depends on the initial conditions, which are also randomized. For several independent training processes, the number of completed epochs is between 500 and 1000, making the training time to be about 5-15 min on a standard commercial computer. The prediction rate of the trained network is about  $4 \cdot 10^5$  examples per second. This corresponds to a maximum correction time of 0.625 sec when the surface occupies the entire FOV. Such a short time renders this procedure practical, especially for high volume production. The main steps of the correction method are summarized in Fig. 3.9.



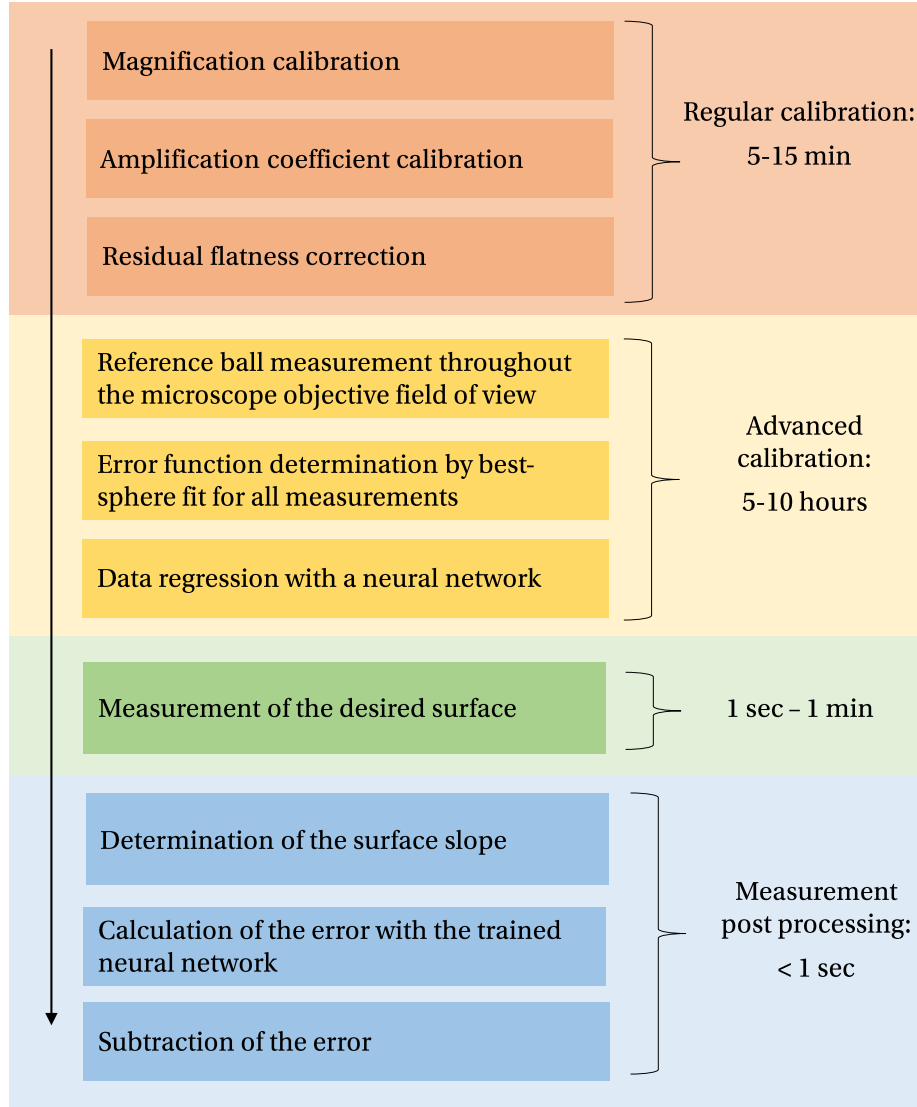


Figure 3.9 – Summary of the steps involved in the proposed correction method.

#### 3.4.2 Results and discussion

##### Spherical surfaces

In order to illustrate the benefit of this method, measurements of different reference balls with nominal ROCs  $R_n$  ranging from  $450\ \mu\text{m}$  to  $875\ \mu\text{m}$  are corrected. Results, comprising the corrected and uncorrected ROC values  $R_c$  and  $R_u$ , respectively, as well as the best sphere fit residual  $\rho$ , are presented in Table 3.1. For each ball, the measured surface is cropped at a diameter  $2a$  such that the maximum considered slope is  $25^\circ$ .

### Chapter 3. Microlens Surface Measurement

Table 3.1 – Effect of the correction on different reference ball measurements. The cropped diameter  $2a$  is chosen to obtain a maximum slope of  $25^\circ$ . The uncorrected ROC value  $R_u$  has a constant offset of 1.2 % compared to the nominal value  $R_n$ . After correction, the ROC value  $R_c$  converges towards  $R_n$ . The RMS value of the spherical fit residual  $\rho_{rms}$  is also decreased by a factor  $> 6$ . Uncertainties are given as a 95% level confidence interval.

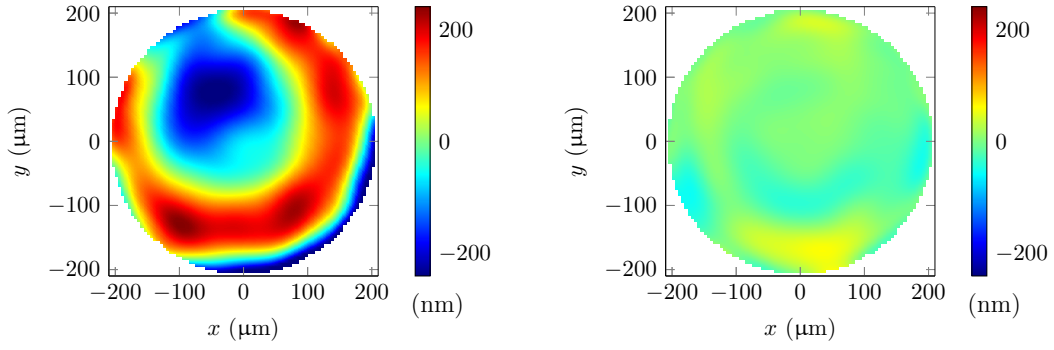
$R_n$	$R_u$	$R_u - R_n$		$R_c$	$R_c - R_n$		$\rho_{rms}$		$2a$
( $\mu\text{m}$ )	( $\mu\text{m}$ )	( $\mu\text{m}$ )	(%)	( $\mu\text{m}$ )	( $\mu\text{m}$ )	(%)	(nm)	(nm)	( $\mu\text{m}$ )
$450 \pm 0.4$	$454.9 \pm 2.6$	+4.9	+1.23	$447.9 \pm 0.5$	-2.1	-0.47	137.6	32.0	380
$500 \pm 0.4$	$505.7 \pm 2.8$	+5.7	+1.14	$499.2 \pm 0.4$	-0.8	-0.16	140.1	20.6	420
$550 \pm 0.2$	$556.3 \pm 3$	+6.3	+1.15	$549.8 \pm 0.4$	-0.2	-0.04	144.1	21.7	460
$750 \pm 0.4$	$759.3 \pm 4.2$	+9.3	+1.24	$751.7 \pm 0.3$	+1.7	+0.22	145.2	11.7	640
$875 \pm 0.4$	$886.6 \pm 5$	+11.6	+1.33	$877.8 \pm 0.2$	+2.8	+0.32	129.7	21.3	740

The effect of aberrations can be divided into a ROC shift and a residual deviation  $r$  from the spherical shape. Before the correction, the relative ROC shift seems to be a constant function. Its average value is 1.22 %. After the correction, its average value decreases to 0.24 %. However, the corrected shift is not constant and increases when  $R_n$  deviates from 550  $\mu\text{m}$ , the ROC of the ball used to record the error function. This is not surprising since the curvature of the ball is not taken into account.

These values have to be put in perspective with the uncertainty of the nominal ROC  $R_n$ , the uncorrected ROC  $R_u$ , and the corrected ROC  $R_c$ . The uncertainty of  $R_n$  is derived from the manufacturer specifications and by ball roundness simulation, as done in Section 3.2.2. For the 550  $\mu\text{m}$  ball, because a random ball test is performed, the uncertainty is reduced. The uncertainty of  $R_u$  is derived from the uncertainty of the magnification and amplification coefficient uncertainty combined with the repeatability uncertainty. Finally, the uncertainty of  $R_c$  is derived from the uncertainty of the 550  $\mu\text{m}$  ball and the repeatability. A more detailed discussion about the uncertainty calculation is found later in this chapter, Section 3.4.3.

The comparison of the different uncertainties shows that even though the correction procedure well reduces the ROC shift, it is still higher than the uncertainty. Moreover, it has a general trend. All this shows that the correction procedure does not correct all the errors and may be improved.

The RMS value of the spherical fit residual  $\rho_{rms}$  is quite constant before correction with an average value of 139.3 nm. In the corrected case, this average value drops to 21.5 nm, i.e., a reduction by a factor  $> 6$ . However, from the ball specification, an RMS value  $< 10\text{nm}$  is expected, which shows the imperfection of the method again. As an illustration, the residual deviation of the 500  $\mu\text{m}$  ROC ball is depicted in Fig. 3.10.



(a) Uncorrected spherical fit residual  $\rho$ :  
 $R = 505.7 \mu\text{m}$ ,  $\rho_{rms} = 140.1 \text{ nm}$ .

(b) Corrected spherical fit residual  $\rho$ :  
 $R = 499.2 \mu\text{m}$ ,  $\rho_{rms} = 20.6 \text{ nm}$ .

Figure 3.10 – Spherical fit residual of the confocal microscope measurement of a reference ball of nominal ROC value  $R_n = 500 \pm 0.2 \mu\text{m}$ . Using the same color bar scale allows for clear visualization of the improvement.

#### Calibration improvement

In the previous section, it is seen (Table 3.1) that the ROC shift is not completely corrected after calibration. Here, we propose an explicit explanation and an additional method to correct it.

We assume that the magnification and the amplification coefficient of the system are not ideally calibrated so that the measured surface of a reference ball with a ROC  $R_0$ , using the 2nd order Taylor expansion to allow an analytical derivation, can be written as:

$$z = \frac{r^2}{2\gamma R_0}. \quad (3.28)$$

The coefficient  $\gamma$  is the same as in Section 3.2. For the calibration method we propose, the considered error  $\epsilon$  is written

$$\epsilon = \frac{r^2}{2\gamma R_0} - \frac{r^2}{2R_0} = \frac{r^2}{2R_0} \left( \frac{1}{\gamma} - 1 \right). \quad (3.29)$$

Now, we consider a second surface with a different ROC  $R_1 = R_0 + \Delta R$ . Again, the surface sag is given by  $z_1 = \frac{r_1^2}{2\gamma R_1}$ .

In this case, the error  $\epsilon$  cannot be considered a function of the location within the FOV, but only of the surface slope. Indeed, it is caused by a miscalibration of the magnification and amplification coefficients, which are identical throughout the FOV.

### Chapter 3. Microlens Surface Measurement

The position  $r_0$  used to record the error that is subtracted at a position  $r_1$ , is thus determined by equaling the slopes:

$$\frac{r_0}{R_0} = \frac{r_1}{R_1} \rightarrow r_0 = \frac{R_0}{R_1} r_1. \quad (3.30)$$

The measured second surface after correction is thus written:

$$z_1 = \frac{r_1^2}{2\gamma R_1} - \epsilon = \frac{r_1^2}{2\gamma R_1} - \frac{1}{2} \frac{R_0}{R_1^2} r_1^2 \left( \frac{1}{\gamma} - 1 \right) = \frac{r_1^2}{2R_1} \left[ \frac{1}{\gamma} - \frac{R_0}{R_1} \left( \frac{1}{\gamma} - 1 \right) \right] := \frac{r_1^2}{2R'_1}. \quad (3.31)$$

This equation finally allows us to determine what is the impact of the calibration on the ROC  $R_1$ :

$$\frac{R_1}{R'_1} = \frac{1}{\gamma} - \frac{R_0}{R_0 + \Delta R} \left( \frac{1}{\gamma} - 1 \right), \quad (3.32)$$

which equals to 1 for all  $R_1$  when  $\gamma = 1$  or when  $\Delta R = 0$  for all  $\gamma$  as we intuitively expect.

If the uncorrected ROC offset of 1.15% of the 550  $\mu\text{m}$  ROC ball is assumed to be a consequence of a miscalibration of the magnification and of the amplification coefficient, the different measured ROCs have an error that is presented in Figure 3.11. In this plot, a good agreement between the experimental values and Eq. (3.32) can be seen. The observed differences may be explained by the Taylor expansion approximation or by a coefficient  $\gamma$  non-equal to 1.15%.

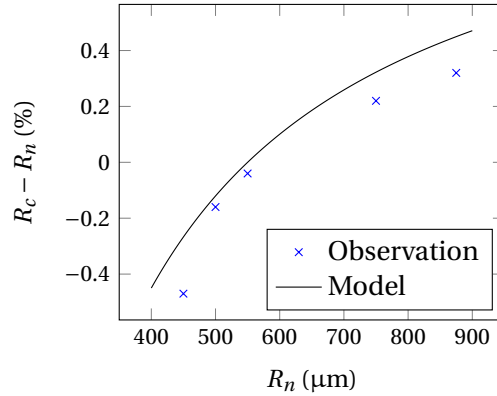


Figure 3.11 – Relative difference between the corrected ROC value  $R_c$  and the nominal value  $R_n$  as a function of the nominal value. A good agreement is observed between the measurements and the model. They both present an increase of the offset when  $R_n$  deviates from 550  $\mu\text{m}$ . The remaining difference may be partially explained by the 2nd order approximation of the model.

This result suggests an additional step in the correction procedure: since the change of 1.15% seems due to a miscalibration of the ideal model and not induced by the deviation from this one, the initial calibration should be modified accordingly. Determining the  $\gamma$  coefficient can be done through the 550  $\mu\text{m}$  reference ball measurement, or it can be based on the average ROC shift of all balls. However, in the second case, the full calibration procedure requires the measurement of a few balls to be finalized. The effort to perform this task in terms of time is small since it takes only a few minutes to be done. We thus consider it here. Results presented

### 3.4. Local plane surface approximation model

in Table 3.1 are analyzed a second time with this additional step and summarized in Table 3.2. The comparison of the ROC shift value between these two tables shows that this additional step improves the accuracy of the ROC determination.

Table 3.2 – Effect of the correction on different reference ball measurements with the additional step that modifies the initial calibration (magnification and amplification coefficient) of the instrument. In this case, the average absolute relative difference with the nominal value is 0.06%, whereas it is 0.24% without this additional step. Uncertainties are given as a 95% level confidence interval.

$R_n$	$R_u$	$R_u - R_n$		$R_c$	$R_c - R_n$		$\rho_{rms}$		$2a$
( $\mu\text{m}$ )	( $\mu\text{m}$ )	( $\mu\text{m}$ )	(%)	( $\mu\text{m}$ )	( $\mu\text{m}$ )	(%)	(nm)	(nm)	( $\mu\text{m}$ )
$450 \pm 0.4$	$454.9 \pm 2.6$	+4.9	+1.23	$449.3 \pm 0.5$	-0.7	-0.15	137.6	31.5	380
$500 \pm 0.4$	$505.7 \pm 2.8$	+5.7	+1.14	$499.9 \pm 0.4$	-0.1	-0.02	140.1	16.6	420
$550 \pm 0.2$	$556.3 \pm 3.0$	+6.3	+1.15	$550.2 \pm 0.4$	+0.2	+0.03	144.1	20.4	460
$750 \pm 0.4$	$759.3 \pm 4.2$	+9.3	+1.24	$750.3 \pm 0.3$	+0.3	+0.03	145.2	16.4	640
$875 \pm 0.4$	$886.6 \pm 5.0$	+11.6	+1.33	$875.6 \pm 0.2$	+0.6	+0.07	129.7	24.3	740

#### Aspheric surface

More generally, a microlens consists of an aspheric surface defined by its ROC  $R$  and its conic constant  $\kappa$  [89]. In order to illustrate the correction method for this extended geometry, the case of an aspheric microlens is presented.

The evaluation of the correction method accuracy is more tricky in this case as no reference surface exists. A workaround is to measure this aspheric surface with an almost aberration-free imaging system. This task is completed by using the CSI *Nexview* by Zygo configured with its  $50\times$  NA 0.55 Mirau MO and a  $0.5\times$  zoom lens. However, the FOV in this configuration is reduced to  $340\mu\text{m}\times 340\mu\text{m}$ . In order to measure the full surface, image stitching has to be used. A 50 % overlap between images is used to get rid of stitching artifacts. In the present case, this corresponds to a measurement of 9 frames, taking 4 min to capture compared to 25 seconds for the confocal microscope measurement.

In order to show that this measurement system can be a reference, it is used to measure a  $600\mu\text{m}$  ROC reference ball. The ROC of this ball is chosen in order for the ball surface to be the closest possible to the measured asphere. The results are presented in Fig. 3.12: the measured ROC shift  $\Delta R$  is  $0.3\mu\text{m}$  and RMS value of the residual is 6.3 nm. Both values are within the uncertainty values and negligible compared to the ones obtained with the uncorrected confocal microscope measurement. Again, a random ball test can confirm this conclusion. Even though it may be surprising that the more complex Mirau objective gives the best results, it should be noted that the FOV is reduced by a factor of more than 2 for almost the same NA and magnification.

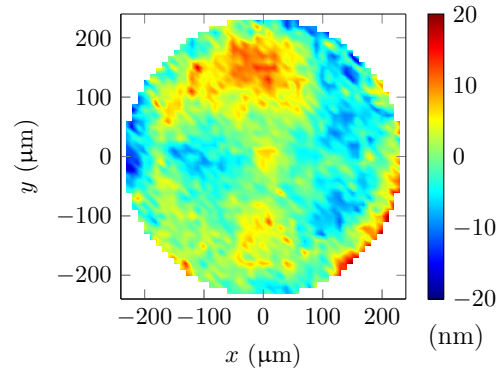


Figure 3.12 – Spherical fit residual of the CSI measurement of a reference ball of nominal ROC value  $R_n = 600 \pm 0.4 \mu\text{m}$ :  $R = 600.3 \pm 3.2 \mu\text{m}$ ,  $\rho_{rms} = 6.3 \text{ nm}$ .

Figure 3.13 presents the aspheric fit residual of the reference, the uncorrected, and the corrected measurements. Table 3.3 presents the  $R$  and  $\kappa$  values for these three measurements. After correction, confocal microscope and CSI measurements are consistent. Indeed, the RMS value of the difference between the corrected confocal microscope and the CSI surfaces is only 14 nm. Such a good agreement is not evident since the measurements are carried out with two different instruments with different working principles. Moreover, their calibration is not performed using the same artifacts.

Table 3.3 – Effect of the correction on aspheric microlens parameters:  $R$  and  $\kappa$  are corrected, and the RMS value of the fit residual  $\rho_{rms}$  converges towards the reference value. Uncertainties of  $R$  and  $\kappa$  measured with the reference system are given as expanded uncertainties and derived from the uncertainties of the calibration standards, assuming no aberration in the CSI measurement system.

	Uncorrected	Corrected	Reference
$R (\mu\text{m})$	523.9	$528.3 \pm 0.4$	$528.4 \pm 2.8$
$\kappa$	-2.84	$-2.59 \pm 0.04$	$-2.60 \pm 0.02$
$\rho_{rms} (\text{nm})$	59.6	26.6	16.3

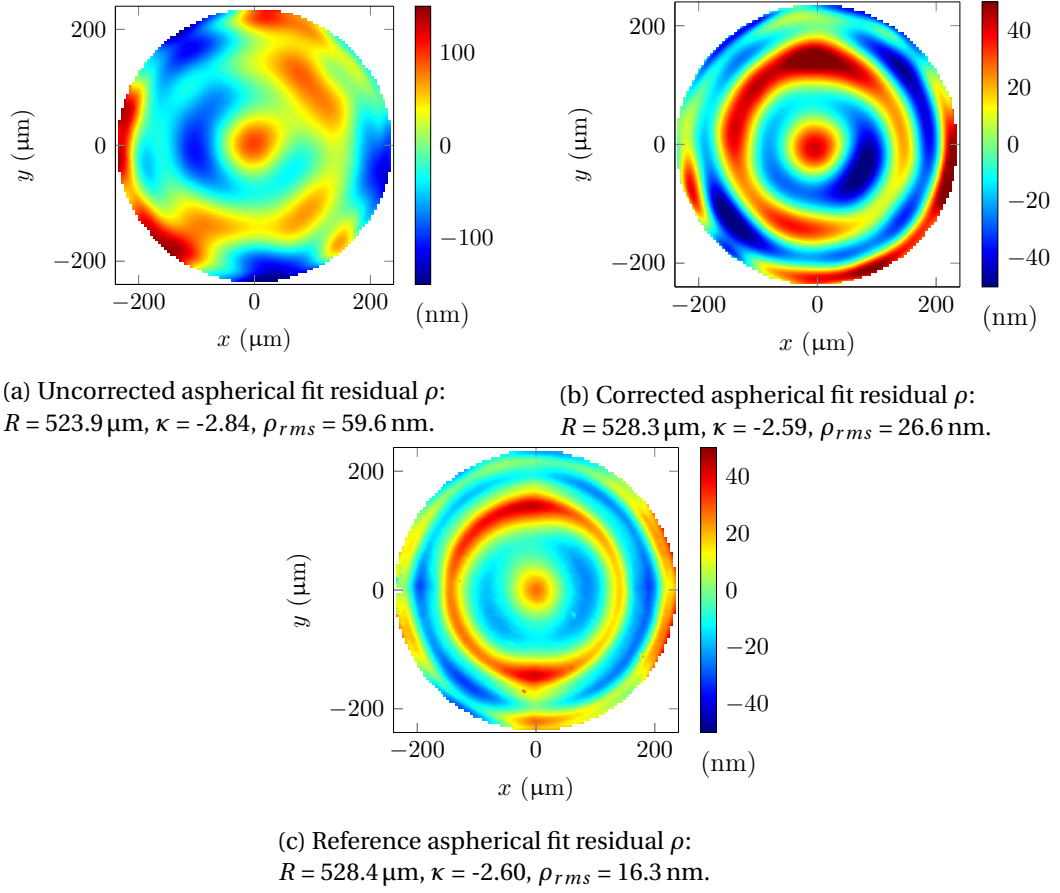


Figure 3.13 – The aspherical fit residual of the confocal microscope measurement of a strong asphere before correction (a), after correction (b), and of the CSI measurement (c). The diameter is  $480 \mu\text{m}$ , and the maximal slope is  $21.7^\circ$ . The shape of the confocal microscope measurement residual after correction is qualitatively similar to the reference one, meaning they both provide similar feedback for fabrication process improvement.

#### Impact on the optical performance assessment

As mentioned in the introduction, one role of the surface measurement is to control the optical quality of the surface. It is thus important to evaluate the accuracy of the measurement in terms of optical performance. A way to do this is to translate the ROC shifts into focal length shifts, and the residual surface deviations into wavefront aberrations [90]. Quantitatively, the focal shift is approximated by

$$\Delta f = \frac{\Delta R}{n - 1}, \quad (3.33)$$

where  $n$  is the refractive index of the microlens. In the uncorrected case, for  $n = 1.5$ , values presented in Table 3.1 lead to an average defocus of 2.44 %, which is corrected up to the calibration uncertainty with the proposed approach. On the other hand, the value of the wavefront error can be estimated using the thin element approximation. This estimate is

appropriate since it is applied only to the surface deviation and not to the surface itself. Indeed, the surface deviation and the corresponding slope deviation are much smaller than the surface height, respectively than the surface slope. With this approximation, the phase shift  $\Delta\Phi$  under a plane wave illumination [50] is given by

$$\Delta\Phi = \frac{2\pi}{\lambda}(n-1)\rho, \quad (3.34)$$

with the residual surface deviation  $\rho$ .

Without correction, the RMS surface deviation attributed to the measurement system is about 140 nm and about 20 nm after correction, see Table 3.1. For  $\lambda = 500$  nm and  $n = 1.5$ , this leads to an RMS wavefront error of  $\lambda/7$  (Strehl Ratio  $\sim 0.45$ ) without correction and of  $\lambda/50$  (Strehl Ratio  $\sim 0.98$ ) after correction. This demonstrates that this method is suited for the characterization of diffraction-limited microlenses.

#### 3.4.3 Uncertainties

The uncertainties provided in this section are given as standard uncertainties, meaning they represent the estimated standard deviation of the measurement result. However, the final statement about the uncertainty is given as a confidence interval, commonly a 95% confidence interval. To derive this interval, a coverage factor that depends on the probability distribution must be applied. Practically and for most cases, this coverage factor is close to 2 for a 95% confidence level interval.

**Nominal ROC:**  $u_{R_n}$  is the combination of the diameter uncertainty  $u_{\tilde{r}_0}$  with the uncertainty due to the roundness, which is the standard deviation of the distribution of local ROC measurements,  $u_{rdn} = \sigma_R$ , when no random ball test is performed. When a random ball test is performed, then the latter is reduced by a factor  $\sqrt{N}$ :  $u_{rdn} = \sigma_R / \sqrt{N}$ . In summary,

$$u_{R_n} = \sqrt{u_{\tilde{r}_0}^2 + u_{rdn}^2}. \quad (3.35)$$

**Measured ROC:**  $u_R$  is the combination of several uncertainties:

1. The repeatability uncertainty  $u_{rep}$ , which is assessed experimentally.
2. The calibration uncertainty  $u_{cal}$ , which is due to the uncertainty of the magnification and amplification coefficient calibration for the standard calibration. For the proposed method, it is based on the uncertainty of the  $\gamma$  coefficient obtained with a random ball test.
3. The uncertainty of the conic constant being fixed,  $u_\kappa$ , which is derived from equation Eq. (3.7).



### 3.4. Local plane surface approximation model

The combined uncertainty is thus given by:

$$u_R = \sqrt{u_{rep}^2 + u_{cal}^2} \text{ or } u_R = \sqrt{u_{rep}^2 + u_{cal}^2 + u_{\kappa}^2}, \quad (3.36)$$

depending if  $\kappa$  is a fit parameter or not.

**Conic constant:**  $u_{\kappa}$  is the combination of the uncertainty due to calibration and the repeatability:

$$u_{\kappa} = \sqrt{4(1+\kappa)^2 (u_{c_M}^2 + u_{c_a}^2) + u_{rep}^2} \text{ or } u_{\kappa} = \sqrt{4(1+\kappa)^2 (u_{\gamma}^2 + 3u_{c_M}^2) + u_{rep}^2}, \quad (3.37)$$

depending if a random ball test is performed or not.

**Residual error:** The RMS value of the spherical deviation of a reference ball is  $< 10\text{ nm}$  as stated by the manufacturer and as it is confirmed by the measurement of the reference ball by the CSI Nexview. This shows that the calibration procedure is not perfect and that some residual error exists. Here, we want to calculate the uncertainty of the RMS irregularity value RMSi due to this residual error.

First, it has to be recalled that a function can be seen as a vector and its RMS value as its norm. This is valid for a residual, and we use this property here. The addition of RMS values of two residual,  $\rho_{rms}^{(1)}$  and  $\rho_{rms}^{(2)}$ , obeys the vectorial addition and thus depends on the angle  $\theta$  between these vectors. This is written

$$\rho_{rms}^{tot} = \sqrt{\left(\rho_{rms}^{(1)} + \cos(\theta)\rho_{rms}^{(2)}\right)^2 + \left(\sin(\theta)\rho_{rms}^{(2)}\right)^2} \quad (3.38)$$

and shows that when the form of the residual is identical, their norm simply adds, and when they are orthogonal, the Pythagorean addition applies. The angle between the two residuals is thus the key but unknown parameter. From observation, it is quite intuitive that it is more likely that two residuals, coming from the manufacturing and the measurement tool, have not much correlation. To estimate the uncertainty, we choose to define  $\theta$  as a random variable defined on the interval  $(0, \pi)$  with a Gaussian distribution centered at  $\pi/2$ . The standard deviation is set to  $\pi/10$ .

The results in Table 3.2 give an RMS residual error  $\rho_{rms}^{\epsilon}$  of  $19.4 \pm 3.7\text{ nm}$ . If an RMS residual  $\rho_{rms}^m$  is measured, then the actual irregularity RMS can be estimated by inverting the previous equation:

$$\text{RMSi} = \sqrt{(\rho_{rms}^m)^2 - (\sin(\theta)\rho_{rms}^{\epsilon})^2 - (\cos(\theta)\rho_{rms}^{\epsilon})^2}, \quad (3.39)$$

which is also a random variable. We chose the expected value of its distribution as the estimate and the standard deviation for the standard uncertainty. The determination of the uncertainty for the aspheric surface correction is done using the following numerical values:  $\rho_{rms}^e = 20$  nm,  $\rho_{rms}^m = 26.6$  nm. This leads to

$$\text{RMSi} = 18.3 \text{ nm} \pm 7.5 \text{ nm}, \quad (3.40)$$

which is perfectly coherent with the value measured with the CSI Nexview of 16.3 nm. This also confirms that the assumption of quasi orthogonality is relevant.

#### Possible improvements

The RMS value of the spherical deviation after correction is about 20 nm, see Table 3.1. The reference balls specification as well as CSI measurements, see Fig. 3.12 for example, show that the actual surface deviation RMS of reference balls is below 10 nm. This suggests that this method can still be improved. Two points are believed to offer improvement potentially. First, the second derivative of the surface could be taken into account. Practically, this means that the surface error needs to be recorded for different curvatures for a given slope. This can be achieved by measuring not only one, but several reference balls with different ROCs across the FOV. Secondly, since only aberrations of the imaging systems have been considered, errors of the mechanical displacement could also be taken into account. For instance, a misalignment between the optical and mechanical axis could have an effect on the measurement.

It also has to be noted that this method can be extended directly to characterize cylindrical or freeform surfaces.

### 3.5 Phase jumps in coherence scanning interferometry (CSI)

When microlens surface measurements are performed by a coherence scanning interferometer, it may happen, especially when the surface slope is steep, that a surface error occurs caused by phase ambiguity during the signal processing step converting the phase to the surface height. This effect has physical origins, as it is enhanced by vibrations, steep slopes, and wrong positioning of the reference mirror in the Mirau microscope objective. Figure 3.14 shows an example of a microlens surface measurement performed by the CSI Nexview equipped with the 20× microscope objective. The microlens geometrical parameters are diameter  $2a = 750 \mu\text{m}$ ,  $R = 896 \mu\text{m}$ , and  $\kappa = -4.35$ . When the surface is filtered with a high-pass filter, Fig. 3.14b, a sudden change of height as well as spikes are observed. It is clear they are not caused by the fabrication process but are the translation of the aforementioned phase jumps issue.

However, under the assumption that the surface is smooth, this error can be effectively corrected. To do so, we start with the following observation: a phase jump occurs on a scale

### 3.5. Phase jumps in coherence scanning interferometry (CSI)

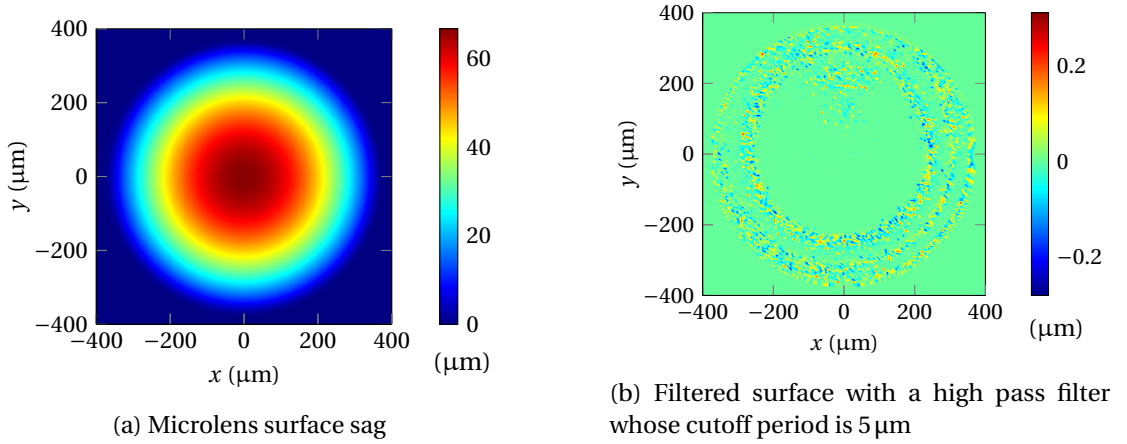


Figure 3.14 – Microlens surface sag (a) and its high spatial components (b) measured by the CSI Nexview equipped with its  $20\times$  microscope objective. The microlens geometrical parameters are: diameter  $2a = 750\mu\text{m}$ ,  $R = 896\mu\text{m}$  and  $\kappa = -4.35$ . Measurement artifacts (spikes) are easily observed in (b).

of one pixel and thus provokes a sudden change of height but also of the surface slope. In order to determine the change of values provoked by phase jumps and compare them to the changes provoked by the surface, properties of the system have to be quantified. Again, the measurements are performed with a  $20\times$  NA 0.4 zoom lens  $0.5\times$ . With this magnification, the lateral spatial sampling is  $0.82\mu\text{m}/\text{pixel}$ . The central wavelength of the light spectrum used in the CSI is  $500\text{ nm}$ , which means that a single phase jump of  $\pi$  leads to a change of  $250\text{ nm}$  in height,  $17^\circ$  in slope, and  $0.38\text{ mm}^{-1}$  in the second derivative.

The same changes caused by the microlens surface are derived from the microlens parameters. This leads to a maximum slope of  $16.8^\circ$ . For an ideally smooth surface, over one pixel, the maximum change in height is  $246\text{ nm}$ , the maximum change in slope is  $0.03^\circ$ , and the maximum change in the second derivative is  $6.1 \cdot 10^{-4}\text{ mm}^{-1}$ . By comparing these values to the one provokes by phase jumps, it is seen that looking at the slope or the second derivative of the surface allows for easy identification of the phase jumps. However, when the surface roughness provokes slope changes with an amplitude comparable to those provoked by phase jumps, it is no more possible to differentiate them. The assumption of smoothness is thus crucial. Luckily, optical surfaces generally require a very low roughness, and reflow with subsequent RIE based microlenses generally have a roughness  $s_q < 1\text{ nm}$ .

Based on these considerations, we choose to use the second derivative to identify the phase jumps. Figure 3.15a plots the second derivative along  $x$ ,  $D_{x,x}$ , of the measured surface. Spikes that form rings are observed. This pattern is identical to the one observed in Fig. 3.14b. Figure 3.15b shows the histogram of the second derivative along  $x$ . Several peaks are observed and correspond to integer number ( $0, \pm 1, \pm 2, \dots$ ) of phase jumps. These peaks are equivalently spaced by  $0.4\text{ mm}^{-1}$ , which is the effect of a single phase jump as previously calculated. The width of the peaks is due to the roughness of the surface. However, the separation of the peaks

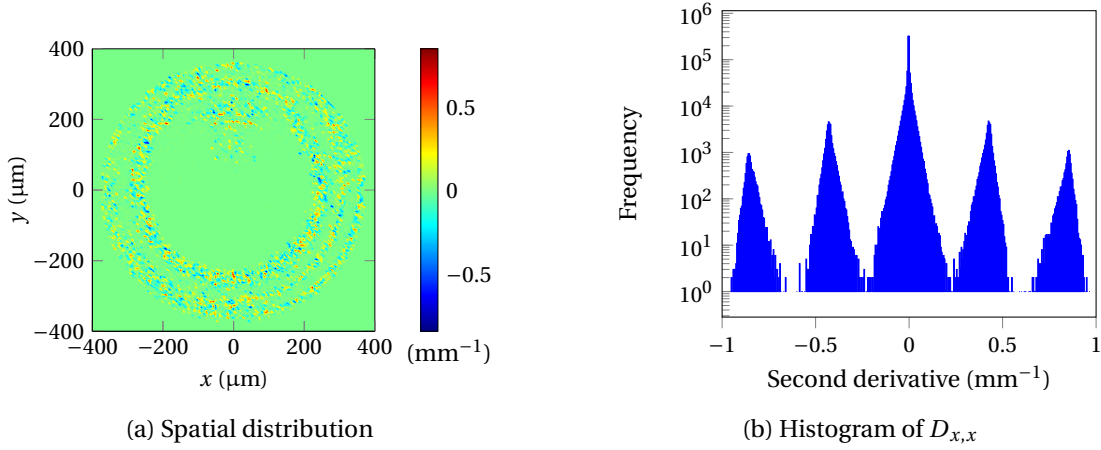


Figure 3.15 – Second derivative along the x-axis  $D_{x,x}$ . (a) The spatial distribution of  $D_{x,x}$  is identical to Fig. 3.14b allowing the spatial localization of the phase jumps. (b) The histogram of  $D_{x,x}$  shows different peaks that correspond to an integer number of phase jumps. Because the peaks are well separated, the number of phase jumps that occurs may be assessed and thus corrected.

is very neat, the y-axis being in log scale. This suggests a way to correct this error: each peak has to be brought back to zero.

If we name  $D_{x,x}^\epsilon$  the absolute value of the shift of  $0.4 \text{ mm}^{-1}$  produced by a single phase jump in  $D_{x,x}$ , then for each  $D_{x,x}$  the corrected value  $D_{x,x}^c$  is:

$$D_{x,x}^c = D_{x,x} - \text{round}\left(\frac{D_{x,x}}{D_{x,x}^\epsilon}\right). \quad (3.41)$$

Once this correction is done for every pixel, the surface is reconstructed by two integration steps. This can be done for every line of pixels independently, from left to right, for example, as the first rows of pixels ( $x \sim -400 \mu\text{m}$ ) do not contain errors, see Fig. 3.15a.

The method we propose to solve this issue is summarized by the following steps:

1. Identification of the phase jumps locations by computing the second derivative with respect to  $x$ ,  $D_{x,x}$ .
2.  $D_{x,x}(x, y)$  is corrected according to Eq. (3.41).
3. The surface is reconstructed by a double integration.

To evaluate the effectiveness of this method, we present the surface irregularity over the clear aperture before and after the correction procedure, see Fig. 3.16. Before the correction, surface height errors due to phase jumps are visible. After correction, the surface appears smooth as expected. The irregularity presents a radial symmetry, which is expected for an RIE based

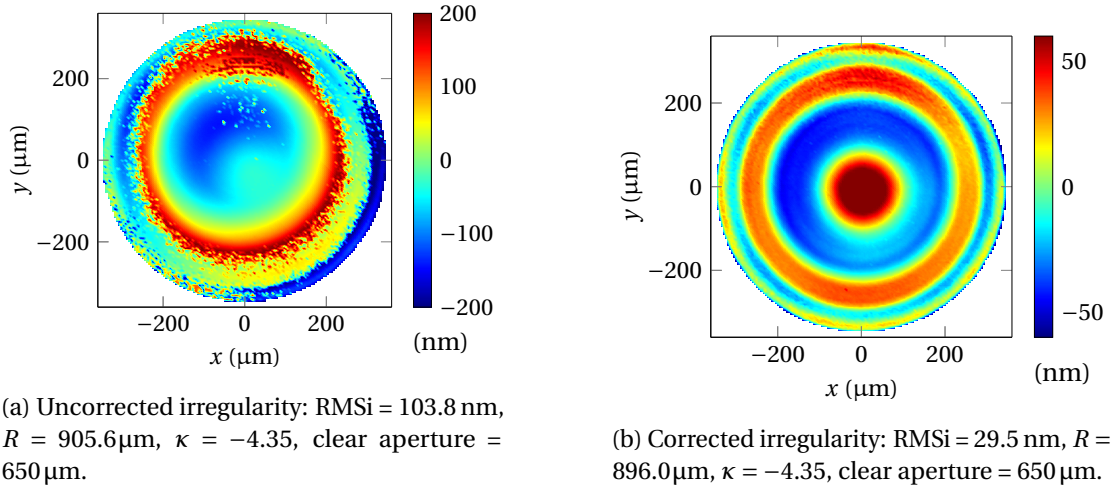


Figure 3.16 – Comparison between the irregularity before (a) and after (b) the correction procedure. For this particular example, the phase jumps issue increases the RMS value by a factor of 3.5 and provokes a ROC increase of 1.1%. Without this correction, the characterization of the surface is impossible.

microlens. The RMS value of the irregularity,  $\text{RMSi}$ , goes from 103.9 nm before correction to 29.5 nm after correction. Likewise, the ROC  $R = 905.6 \mu\text{m}$  before the correction and  $896.0 \mu\text{m}$  after correction. This represents a difference of +1.1%. These numbers demonstrate that without this correction procedure, the characterization of the microlens through this surface measurement is impossible.

This method is likely not the only way to correct these errors. However, we believe it has one clear advantage: the process is deterministic, and no iteration is needed. The correction process is thus fast: in this example, it takes 0.16 sec to correct a measurement that consists of  $1024 \times 1024$  pixels. This is negligible compared to the measurement time that is  $> 30$  seconds for this microlens.

### 3.6 Conclusion

In this chapter, we discuss the measurement of microlens surfaces by confocal microscopy and coherence scanning interferometry. We mainly focus on the accuracy of such measurements and how to improve it by advanced calibration or correction procedures.

In particular, we show that a surface error appears when non-flat surfaces are measured by optical surface profilers. We review the possible causes and propose a new calibration procedure. This one is based on the fact that the surface can be locally approximated by planes, and it is summarized in Fig. 3.9. We apply it to measurements performed by the confocal microscope  $\mu\text{surf}$  equipped with a  $20\times$  microscope objective. With the common calibration procedure, ROC errors  $> 1\%$  are observed as well as an RMS surface form deviation of  $\sim 140 \text{ nm}$ .

### Chapter 3. Microlens Surface Measurement

---

The proposed calibration procedure corrects the ROC deviation up to the measurement uncertainty level, and the surface form deviation is decreased to  $\sim 20$  nm. This level of accuracy allows the characterization of diffraction-limited microlenses.

In definitive, such calibration shows that it is possible, for a required magnification, to use optical surface profilers equipped with higher NA microscope objectives over larger FOVs. Even though these microscope objectives are more aberrated imaging systems, we show that the characterization of diffraction-limited microlenses is possible. This obviously increases the characterization capability in terms of microlens diameter and numerical aperture, with the corollary of an extension of fabrication capability.

Even though the proposed approach for correction measurement is introduced for microlenses and demonstrated for spherical and aspheric surfaces, it can be extended to any surface that has a large curvature, and that is smooth. In particular, it can be applied to the measurements of freeform surfaces that should be more common in the future in micro-optics.

In this chapter, we also propose a method to correct the error that may appear during the surface reconstruction from phase information in CSI measurements. The procedure consists of a post-processing of the measurement and is shown to be quick ( $< 1$  sec) and effective.

To conclude, we want to discuss the potential future of microlens surface metrology. As stated in the introduction, surface metrology is very important for micro-optics because it allows feedback for fabrication improvement and a quality evaluation at the same time, quickly, in an automated way, and with high accuracy. However, the measurement of microlenses surfaces by optical surface profilers is fundamentally limited by the microscope objective properties, which are themselves limited by the law of optics. The availability of new microscope objectives with a greatly extended capacity of NA seems thus illusory. In the near future, surface metrology for high NA and large microlenses will likely rely on stitching and automated contact probe profilers. The emergence of a completely new technique that outperforms the existing ones is, in our opinion, purely speculative. Consequently, for the next years, an effort has to be put in adapting the existing technologies to the specific case of micro-optics.

## 4 Microlens Fabrication Modeling

This chapter addresses the modeling of the microlens fabrication at the wafer-level. We focus on the photoresist reflow and reactive ion etching processes. In both cases, we use an empirical approach based on experiments. To motivate the need for these models and provide validation, we use them to improve the uniformity over large microlens arrays. The limits of this fabrication technique are also discussed.

### 4.1 Introduction

Refractive microlenses are produced in high volume using wafer-level techniques. In particular, glass and silicon microlenses are fabricated with the well-established technique of photoresist reflow with a subsequent reactive ion etching process [26], see Fig. 1.3. In this chapter, we focus on modeling this specific fabrication technique.

As for any manufacturing process  $P$ , it is ideal to have a full model to obtain complete predictability of the output parameters  $\vec{o}$ , here the etched microlens surface, as a function of the process input parameters  $\vec{i}$ , e.g. the resist spinning time, the reflow temperature, the plasma composition and so on. This means having the relation  $\vec{o} = P(\vec{i})$ . As for most real cases, because of the process complexity, obtaining such a model is impossible. This is particularly true in the present case, which involves two subsequent complex processes, the photoresist reflow and the reactive ion etching process.

Then, how to determine the input that leads to a desired output? An answer that seems trivial is by trial and error. In other words, by experience. The learning process is then nothing else than an optimization process. In this case, it is the surface deviation with respect to the nominal surface that has to be minimized.

Like in any optimization process, the function  $P$  must be evaluated for a given input  $\vec{i}$  as well as its partial derivatives. An evaluation of  $P$  corresponds to a full fabrication process realized with these given input parameters. However, the partial derivatives are still unknown without a model and other trials (the exact number depends on the number of input parameters) are

needed to determine them and to obtain an idea of the convergence direction. Each trial costs resources, money, and time, so the convergence must be as fast as possible. The problem lies in the fact that the number of involved parameters is huge in practice. In the case of a reactive ion etching process, for instance, the plasma composition usually changes with time and is thus a continuous function. Likewise, the output parameters consist of a surface.

It is thus complicated to find the correlation between the input and the output parameters without prior knowledge. For example, it is difficult to link the ROC and the conic constant of the final microlens to the plasma composition. Quantitative strategies must be set up for this purpose.

For that, empirical models can be developed, and their parameters can be determined from experiments. These models can then be used to predict, if not the output as a function of a particular input, the gradient of a certain realization. This is the method we use here to achieve our goals.

Conceptually, it is interesting to note that the modeling task cannot be avoided. Even unconsciously, we make assumptions and evaluate the best improvement step based on our understanding of the reality, which is nothing else than formally establishing a model to determine the partial derivatives.

As the full fabrication process consists mainly of a photoresist reflow and an etching process, the first section addresses the modeling of the thermal reflow. We first describe the conditions needed to obtain an ideal spherical cap formed by surface tension. Then, from this reference state, we use a perturbative approach to describe the change of shape, which mainly consists of a change of radius of curvature.

The second section is about modeling the transfer of the resist microlens into the substrate by a reactive ion etching process. The model we propose uses macroscopic parameters such as etching rates and the selectivity to describe the dynamics of the process and its effect on the microlens geometry. In particular, the difference between anisotropic and isotropic etching components are discussed.

The third and final section is the application of the models developed to improve the uniformity over one wafer. Indeed, for a given fabrication process, if an input parameter can be modified locally, then the surface of the completed microlenses can be modified as a function of the wafer location. Here we modify the volume of each microlens and show that this allows increasing the uniformity of large MLA.



## 4.2 Photoresist thermal reflow

The mechanism of photoresist thermal reflow consists of the continuous transition of the solid-state of a polymer in its liquid state and is used to create 3D structures in microfabrication [91]. Different contributions focus on the modeling of such a process [92–94]. Nevertheless, here, we are not interested in the dynamics of the reflow neither in the involved complex physicochemical reactions. Our interest lies in the prediction of the surface form after reflow as a function of the initial state. In our case, the diameter and height of the patterned photoresist cylinder are the main input parameters.

The main physical concept that describes resist reflow is surface tension. For this reason, we start by considering the ideal case where surface energy minimization is sufficient to describe the process. Then, we extend the discussion to cases where the effect of other parameters must be included.

### 4.2.1 Spherical cap creation by surface energy minimization

When the reflow temperature and time are well-chosen, all the resist is molten. We can consider that the resist is a liquid, and only the surface tension governs the equilibrium. By saying so, we also assume that the dimensions we consider are smaller than the capillary length [95] of the photoresist, which is confirmed by the experiment. It is known that in such a case, the surface of the liquid droplet is minimized for a given volume [96]. Consequently, it has a spherical form, which is described, when the contact angle  $\theta_c$  is acute, by

$$z(r) = R - \sqrt{R^2 - r^2}, \quad (4.1)$$

with  $r$  the radial coordinate and  $R$  the ROC. By using this fact, it is possible to determine the initial shape of the resist pillar, it means its diameter  $2a_c$  and its height  $h_c$ , to obtain a spherical cap with a certain curvature. Another parameter is however required: the empirical reflow resist shrinkage factor  $\eta_r$  which is defined to be the ratio of the resist microlens volume  $V_r$  to the cylindrical one  $V_c$ ,

$$\eta_r = \frac{V_r}{V_c}. \quad (4.2)$$

Typical values for the physical parameters are  $\eta_r \sim 0.9$  and  $\theta_c \sim 40^\circ$ . The volume of the spherical cap,  $V_r$ , is thus given by:

$$V_r = \eta_r \pi a_c^2 h_c. \quad (4.3)$$

With this volume, the spherical cap is completely determined. Indeed, the contact angle

condition at the resist microlens edge must also be respected. This reads

$$\tan(\theta_c) = \frac{dz(a_r)}{dr} = \frac{a_r}{\sqrt{(R^2 - a_r^2)}}, \quad (4.4)$$

$a_r$  being the semi-diameter of the spherical cap. Since two conditions have to be met and two parameters define the spherical cap,  $R$  and  $a_r$ , these two parameters are completely linked. In other words, for given input parameters  $a_c$  and  $h_c$ , there exists a function  $R = R(a_r)$ .

However, from a practical point of view, the footprint of the photoresist must stay the same during the reflow. Otherwise, we could have a fusion of adjacent microlenses or a reduction of the fill factor. This constraint imposes the condition  $a_r = a_c := a$  and makes  $a$  the single design input parameter. Now, we want to determine the ROC of the spherical cap and the thickness of the resist layer that has to be applied for a desired diameter  $2a$ .

The ROC is simply found by inverting Eq. (4.4) and is given by:

$$R = a \frac{\sqrt{\tan^2(\theta_c) + 1}}{\tan(\theta_c)}. \quad (4.5)$$

To determine the resist layer thickness, the volume of the spherical cap determined geometrically,

$$V_r = \frac{h_r^2 \pi (3R - h_r)}{3} \quad (4.6)$$

must be equaled to Eq. (4.3) to satisfy volume conservation. The height of the resist microlens  $h_r$  is given by  $h_r = R - \sqrt{R^2 - a^2}$ . This finally provides the height of the resist pillar,

$$h_c = a \left( \frac{2(\tan^2(\theta_c) + 1)^{3/2} - 3\tan^2(\theta_c) - 2}{3\eta_r \tan^3(\theta_c)} \right), \quad (4.7)$$

which is proportional to the diameter. The resist thickness is plotted in Fig. 4.1 against the contact angle  $\theta_c$  and the microlens semi-diameter  $a$  for a shrinkage factor  $\eta_r$  of 0.9. For microlenses with a diameter of over 1 mm, the resist layer thickness that must be applied reaches about 100  $\mu\text{m}$  for a typical contact angle of 40°. In this case, it becomes difficult to fulfill this condition because it is challenging to spin-coat such resist thickness.

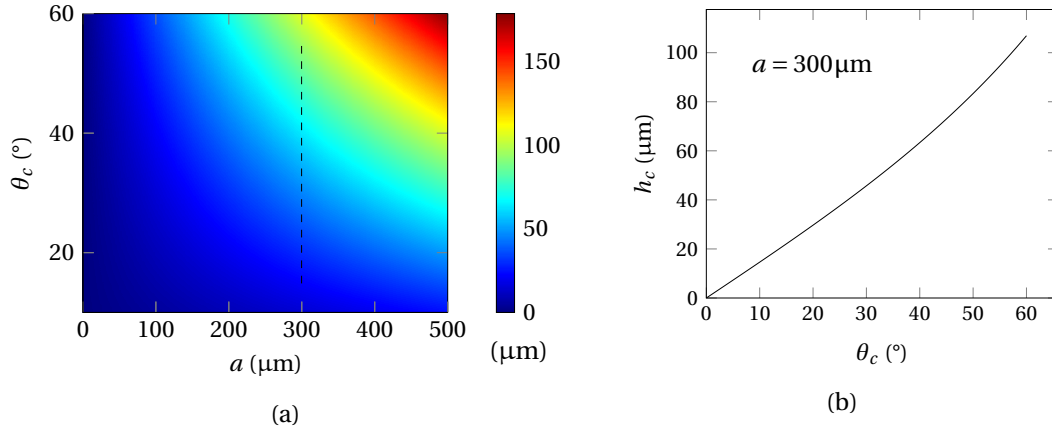


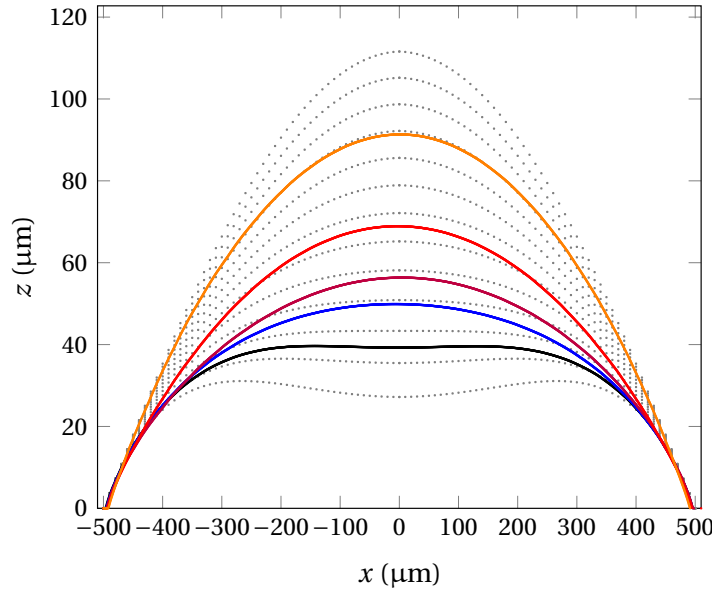
Figure 4.1 – (a) Resist layer thickness  $h_c$  that provides a spherical cap after reflow without footprint change as a function of the semi-diameter  $a$  and the contact angle  $\theta_c$ . The resist shrinkage ratio  $\eta_r$  is set to 0.9. We note that it becomes difficult to produce resist microlenses with diameters over 1 mm when the contact angle is around  $40^\circ$ . Indeed, it is technologically difficult to spin-coat resist layer with the required thickness higher than  $100 \mu\text{m}$ . (b) Section at  $a = 300 \mu\text{m}$ .

#### 4.2.2 Deviation from the ideal spherical cap case

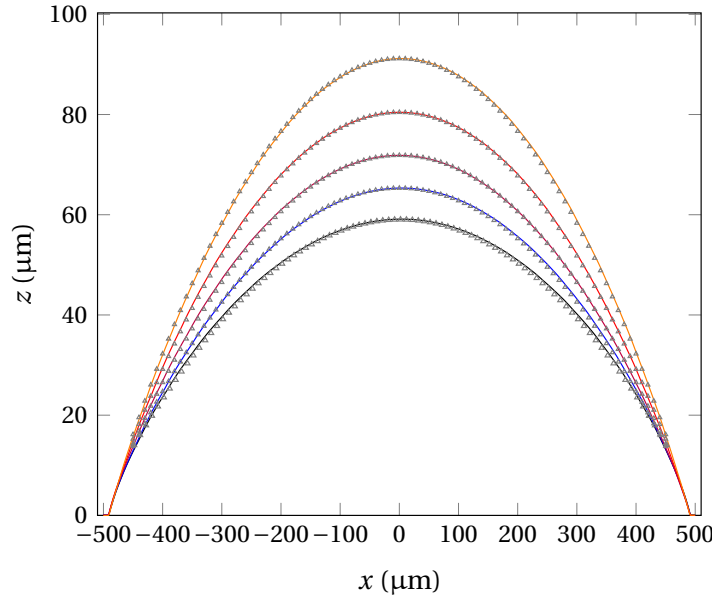
In practice, the conditions for the formation of a perfect spherical cap by means of surface tension are rarely met at wafer-level. Indeed, the spin coating process induces some thickness variations across the wafer, a typical value is 1% Peak-to-Valley for a thickness of  $20 \mu\text{m}$ . Also, repeatability is difficult to achieve. Another reason is that very thick ( $> 30 \mu\text{m}$ ) or thin layers ( $< 1 \mu\text{m}$ ) may not easily be produced, and we have to live with a non-ideal case. The problem is that when the resist volume deviates from the ideal one, the footprint of the resist microlens changes. This is highly problematic for MLAs as the gap between the individual resist microlenses is needed and might be only a few microns. The risk is that the microlenses merge, thus completely deteriorating their shape. Also, if the diameter is reduced, the fill factor is decreased, which is not desirable.

The wafer surface can be processed to keep the footprint constant during the reflow. This is confirmed experimentally, see Fig. 4.2, which presents the profile of resist microlenses for different values of the resist thickness  $h_c$ . Two observations can be done: firstly, the diameter of the microlenses does not change even though the volume variation is important. Secondly, the contact angle does not vary either.

When the footprint and the contact angle are constants, the dynamics of the reflow changes [98] and the produced surface cannot be determined only by considering the principle of surface energy minimization. Indeed, this principle would give a spherical surface that cannot fulfill the contact angle condition, Eq. (4.4). To solve this issue, one approach is the generalization of the Laplace equation to curvature terms [97]. This model is tested



(a) Cylindrical microlenses: when the resist volume reduction starts to be significant, the profile presents a dip. The dashed grey lines represent the predictions of the model proposed in [97]. The agreement is qualitatively good as the dip is predicted, but quantitatively not accurate when the profile deviates from the spherical cap, see blue and red curves.



(b) Circular microlenses: the grey triangles represent the best-sphere fit for each measured profile. The good agreement between the fits and the measurements confirms that the profile remains spherical over most of the diameter when the resist volume change is small.

Figure 4.2 – Measured profiles of microlenses after reflow for different resist layer thicknesses. For both geometries, the footprint and the contact angle remain constants as the resist volume changes.

against experiments, and results are presented in Fig. 4.2a. Even if the model can predict the appearance of dips when the resist volume is low, differences of several microns between the predicted and measured profiles are observed. Other empirical models have also been proposed [99, 100], but here, we use a perturbative approach to represent small deviations around an equilibrium state, because this is more interesting for fabrication purposes. The surface form at the equilibrium point is assumed to be not far from the ideal spherical cap case.

The model we derive is based on an experimental observation: when the resist volume deviates from the ideal spherical cap volume, the microlens surface is still spherical over most of the microlens diameter, see Fig. 4.2b. A deviation occurs only at the edges. This is not problematic from an optical point of view as, usually, the clear aperture of the microlens is set to 90% of the diameter. Under this assumption, we can describe the surface change by a change of ROC as a function of the photoresist volume difference. To obtain this relation, we assume that after reflow, the microlens is still a perfect spherical cap, whatever the difference of volume. In other words, this is equivalent to defining a contact angle that depends on the volume difference.

Following this assumption, and using the second-order Taylor approximation to allow analytical expressions, we write:

$$V_r = \int_0^a dr 2\pi r \frac{r^2}{2R} = \frac{\pi a^4}{4R}. \quad (4.8)$$

However, the resist volume after reflow must also be equal to the value given by the cylinder:  $V_r = \eta_r \pi a^2 h_c$ . Combining these two equations provides the ROC  $R$  as a function of the semi-diameter  $a$ :

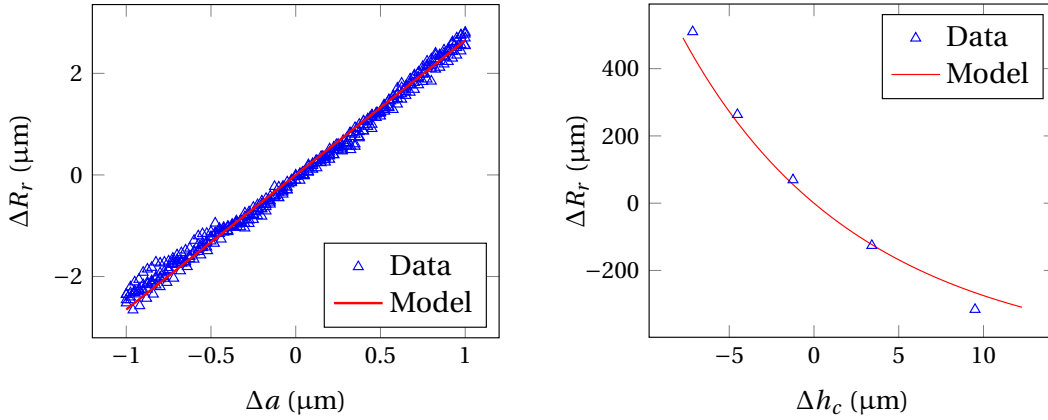
$$R = \frac{a^2}{4\eta_r h_c}, \quad (4.9)$$

which is clearly an approximation that may not be really accurate. However, it should give a good approximation of the differential form. At this point, two parameters change the ROC: the initial resist thickness  $h_c$  and the microlens semi-diameter  $a$ . The total differential thus reads:

$$\delta R = \frac{a}{2\eta_r h_c} \delta a - \frac{a^2}{4\eta_r h_c^2} \delta h_c. \quad (4.10)$$

This first term of this expression is compared to experimental data in Fig. 4.3a. The second term is compared in Fig. 4.3b to the experimental data presented in Fig. 4.2b. We note that in both cases, the model fits well the experiments.

This expression can thus be used to determine the change of ROC as a function of the resist



(a) Measured difference of resist microlens ROC  $\Delta R_r$  as a function of the semi-diameter variation  $\Delta a$ . Initial parameters are  $R_r = 260\mu\text{m}$  and  $2a = 315\mu\text{m}$ . The resist thickness layer is constant with a value of  $60\mu\text{m}$ .

(b) Measured difference of resist microlens ROC  $\Delta R_r$  as a function of the resist thickness variation  $\Delta h_c$ . Initial parameters are  $R_r = 1900\mu\text{m}$  and  $h_c = 42\mu\text{m}$ . The diameter is constant with a value of  $1000\mu\text{m}$ .

Figure 4.3 – Measured change of ROC caused by a change of diameter (a) and by a change of resist layer thickness (b). In both cases, the experiment and the model are in very good agreement.

layer thickness variation, for example. This is useful to avoid the measurement of the surface of the resist spherical cap to determine its ROC: the resist layer thickness measurement might be sufficient. This result is also useful if we want on purpose to modify the ROC of the resist microlenses locally. We use this effect in Section 4.4 to increase the uniformity within an MLA.

In this section, we do not provide a full model of the resist reflow for the creation of resist microlenses. However, based on geometrical considerations and experimental evidence, we give the conditions for the reflow to produce an ideal spherical cap and then consider perturbations from this equilibrium case. This approach is thus sufficient to determine the change of ROC induced by the change on the input parameters when the microlenses are quasi spherical, which is usually the case in practice.

### 4.3 Reactive ion etching (RIE) process

Reactive ion etching is a dry etching process that uses a plasma to remove progressively non-masked parts of the substrate [101, 102]. The reaction can be chemical, thus generating an isotropic etching, or physical, thus etching the surface anisotropically [103]. The ratio between these two etching components can be selected by tuning the plasma parameters.

The RIE process is complex, and we thus model it from a macroscopic point of view. To simplify the discussion, we make some assumptions. We know that the presence of neighboring microlenses influences the etching process, see Section 2.2. Here, we do not consider this

effect, even though it may lead to severe issues in terms of optical performance. The reason is that this effect cannot be corrected by modifying the RIE process parameters. Also, to simplify the discussion, we consider only rotationally symmetrical surfaces. Their profiles are given by a function  $z = s(r)$  with  $r$  the radial coordinate. Finally, the process is assumed to consist only of the variation of a single input parameter  $i = i(t)$  such as a gas flow, for example. Here, we adopt the convention of a normalized time, i.e.  $t \in [0, 1]$ .

The full fabrication process optimization that we address in this chapter can be reduced to the RIE step. Indeed, the input parameters can be reduced to the ROC of the microlens resist, which can be known by measurement, and the function  $i = i(t)$ . For this reason, qualitatively, the optimization can be divided into two situations:

**A.** Given an etching process  $i$ , how is the output (the etched microlens surface) modified when the input (the resist microlens ROC) is changed? This is typically the question that is raised when the repeatability is evaluated. Another example where we face this situation is the case of uniformity improvement over one wafer and is presented in detail in Section 4.4.

**B.** Given a known resist microlens and the result of a RIE process  $i$ , how the completed microlens is modified when this process  $i$  is changed? Or equivalently, how to modify the process to obtain the desired output change? This is the situation we face as a manufacturer when we have to optimize the etching process  $i$ .

This section starts with the case of purely directional (anisotropic) etching. Then, the discussion is shifted to the isotropic case and is finally generalized to the combination of both anisotropic and isotropic etching.

#### 4.3.1 Directional etching

We first consider the case of purely anisotropic (directional) etching. Here, we only describe an etching process that occurs in the  $z$ -direction, see Fig. 4.4.

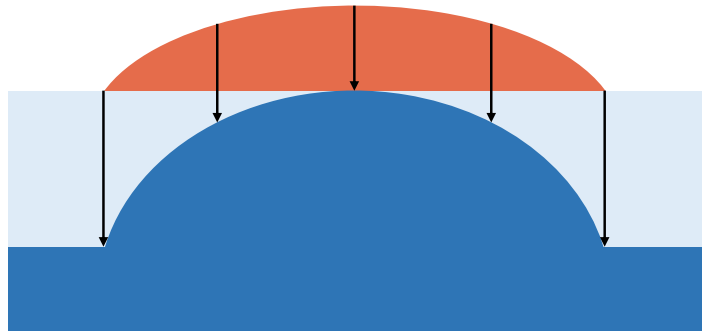


Figure 4.4 – Illustration of a directional etching process. The surface can be seen as a collection of points that are moving along the  $z$ -axis.

## Chapter 4. Microlens Fabrication Modeling

---

The etching process can be macroscopically described by two functions of the input parameter  $i$ : the etching rate of the resist  $v_r = v_r(i)$  and the etching rate of the substrate  $v_s = v_s(i)$ . Because the resist quantity varies along the process, the reactor chemistry may be modified, as well as the etching rates. For this reason, these functions should also depend on the  $z$ -position where the etching happens:

$$\begin{aligned} v_r &= v_r(i, z), \\ v_s &= v_s(i, z). \end{aligned} \tag{4.11}$$

If these two functions were known, it would be possible to determine the function  $i = i(t)$  that should be applied as the input of the system to obtain the desired surface after the etching process. Unfortunately, these functions cannot be determined from more fundamentals physics laws and have to be guessed empirically.

The question is, thus, how to gain information about these two functions? For a given process  $i = i(t)$ , the pieces of information we have are the measurements of the surface of the resist and substrate microlenses,  $s_r(r)$  and  $s_s(r)$ , respectively.

From geometrical considerations presented in Fig. 4.5, we note that during a time  $dt$ , the thickness of resist that is etched is  $v_r dt$ . Likewise, the thickness of the etched substrate is  $v_s dt$ . Moreover, the interface radial position is reduced by  $dr = v_r(r) dt / s'_r(r)$  or equivalently  $dr = v_s(r) dt / s'_s(r)$ . Thereby, the etching selectivity is

$$\Sigma(r) = \frac{v_r(r)}{v_s(r)} = \frac{s'_r(r)}{s'_s(r)}. \tag{4.12}$$

In other words, the selectivity is nothing else than the ratio of the slopes.

This result is an answer to the challenge posed by situation **A**: when the process is stable, the microlens surface is measured before and after the RIE process and the ratio of the slope is determined as a function of the radial position  $r$ . Like this,  $\Sigma(r)$  can be determined. Now, if the surface of the resist microlenses is slightly changed, and we assume this change does not modify the process, the slope of the etched microlens can be obtained using Eq. (4.12). A simple integration step allows the surface reconstruction.

However, this is not enough to address situation **B**. If a process defined by the function  $i$  gives a surface  $s_r$ , we can determine the change of selectivity  $\delta\Sigma(r)$  that should be applied in order to get the desired etched surface. Then, we have to determine the change of the input parameter that provokes this change:  $\delta i(t) \rightarrow \delta\Sigma(r)$ . This operation consists of determining  $i = i(r)$ , meaning the etching position  $r = r(t)$  and then the derivative  $\partial\Sigma/\partial i$  for all  $r$  positions. The goal is thus to develop strategies to get this derivative effectively to obtain the fastest convergence possible of the optimization process.



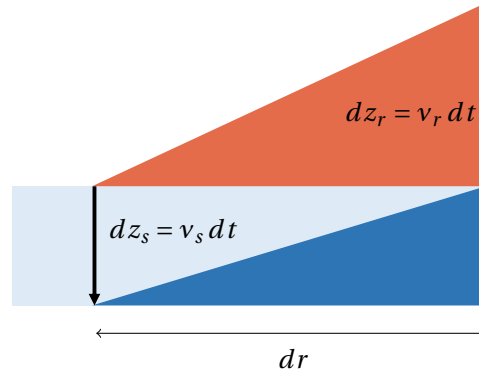


Figure 4.5 – Directional etching at the interface during a time  $dt$ . By trigonometrical considerations, the ratio of the slopes is found to be equal to the etching rates ratio, thus to the selectivity.

We could first make assumptions and use them to obtain the feedback. First, that the etching rate  $v_r$  is constant. This can be motivated by the fact that surface deviations are usually in the nanometer range (along  $z$ ) and have low spatial frequencies (dozens of microns along  $r$ ). Under this assumption, the etching position  $r$  is known as a function of  $t$ , and is approximated by the expression:

$$r(t) = a\sqrt{1-t}. \quad (4.13)$$

On top of that, if we assume the selectivity  $\Sigma$  to be a function of only  $i$  and not of  $z$ , then we can use the variation of the selectivity during the process to estimate the desired gradient  $\partial\Sigma/\partial i$ . The feedback is then obtained. These assumptions should, however, be confirmed as they may be valid for specific processes and not for others.

Another strategy would be to use a more deterministic approach. If a process  $i_0 = i_0(t)$  leads to a certain selectivity  $\Sigma_0 = \Sigma_0(r)$ , we run a second process  $i' = i_0 + A\cos(\omega t)$ . Consequently, the difference of the selectivity between  $i_0$  and  $i'$  contains a pattern with waves. It is then possible to make the correspondence between each node, maximum and minimum. By looking at the nodes, we can estimate the function  $r = r(t)$ . By looking at the amplitude of the maximums and minimums, we can have access to  $\partial\Sigma(i, z)/\partial i$  for all  $z$ -positions.

### 4.3.2 Isotropic etching

In an RIE process, there is also an isotropic etching component that can be important. Because chemical etching can be way faster than physical etching, it is useful in a production environment. However, this component is, in principle, more challenging to handle and has

not the advantage of the directional etching in terms of surface form creation. Here, we model this process and again propose techniques to fulfill the requirements posed by the situations **A** and **B**, as discussed above.

The isotropic etching is, by definition, characterized by an etching rate identical in all directions. The etching process thus occurs perpendicularly to the surface of the object being etched and not only along the  $z$ -axis as for the directional etching, see Fig. 4.6. A point of the surface is thus moving on the axis that is defined by the surface normal. E.g., a sphere remains a sphere, but its ROC is reduced during the etching process. At this point, we remark this is comparable to the propagation of a wavefront, and we use the analogy with optics to model the process. A ray or vector can thus represent a point of the surface.

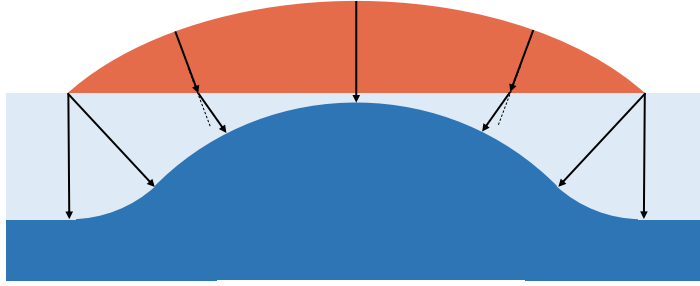


Figure 4.6 – Illustration of an isotropic etching process. The surface can be seen as a collection of points that are moving along the normal of the surface. This behavior is analog to the propagation of a wavefront.

This picture is especially useful to understand the etching at the interface, see Fig. 4.7. At this point, the slope of the rays changes as a result of the different etching rates. This effect is identical to the refraction and can be expressed by:

$$\Sigma = \frac{v_r}{v_s} = \frac{\sin \theta_i}{\sin \theta_o} \approx \frac{s'_r}{s'_s}, \quad (4.14)$$

with  $\theta_i = \arctan(s'_r)$  and  $\theta_o = \arctan(s'_s)$ . The last approximation is accurate when the slopes are not steep or when the selectivity is close to one.

As for the directional etching, these considerations allow us to describe the process with a function  $\Sigma = \Sigma(r)$  and express it as a function of the surface slope. However, this time, a point of the surface changes not only its  $z$ -coordinate but also its radial one  $r$ .

If we define  $r_r$  the radial position of a ray when intersecting the resist surface,  $r_i$  the same quantity but for the interface and  $r_s$  for the completed surface, we obtain the following

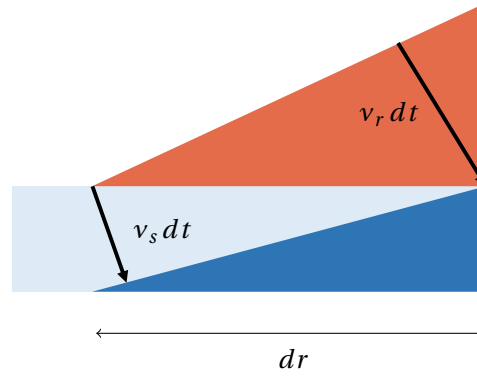


Figure 4.7 – Isotropic etching at the interface during a time  $dt$ . From trigonometrical considerations, the ratio of the etching rate is found to be the ratio of the sinus of the slope angle. This is the analogy of the law of refraction.

relations due to geometrical considerations, see Fig. 4.8:

$$\begin{aligned} r_i &= r_r - s'_r(r_r) s(r_r) \\ r_i &= r_s + s'_s(r_s) (s_s(0) - s_s(r_s)) \end{aligned} \quad (4.15)$$

This allows expressing the selectivity

$$\Sigma(r_i) = \frac{s'_r(r_r)}{s'_s(r_s)}. \quad (4.16)$$

As for the directional etching case, the selectivity is nothing else than the ratio of the surface slopes but calculated at different positions.

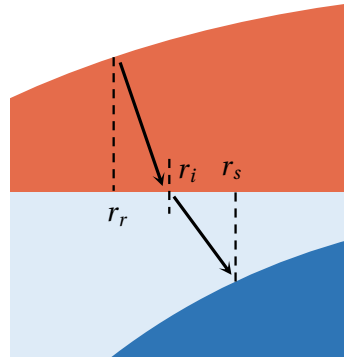


Figure 4.8 – Definition of the different radial positions  $r_r$ ,  $r_i$ , and  $r_s$ .

Again, this answers the question raised in situation **A**. To address case **B**, we can follow the same reasoning as exposed in the case of directional etching. Similarly, we can either first assume a constant etching rate and independence of the selectivity on the  $z$  position and derive the gradient  $\partial\Sigma/\partial g$  from the initial process. Alternatively, we can use two processes that differ by a sinusoidal perturbation.

The main difference between directional and isotropic etching is the round edges observed in the etched microlens surface, see Fig. 4.6. This has significant consequences that should be discussed. As observed in Fig. 4.6, the edges of the resist microlenses are a singularity as the change of slope (the curvature) is infinite at this point. This position can thus be seen as the origin of a spherical wave. This provokes a concave area in the final surface, which does not focus the light. The clear aperture (or optically effective surface)  $A$  is thus reduced, which is undesired, for instance, because it reduces the fill factor of an MLA. For a process completely isotropic, the clear aperture is given by:

$$A = 2 \left( a - \frac{\sin(\theta_c) h_s}{\Sigma} \right), \quad (4.17)$$

with  $h_s = s_r(0)$  the sag of the etched microlens. However, the height of the microlens, optically speaking, is  $h_e = \cos(\theta_c) h_s / \Sigma$ . Indeed, the height of the concave part does not change the phase within a light beam. It can thus be considered as a part of the substrate. Figure 4.9 shows the minimum achievable ROC of an etched microlens that keeps a clear aperture of 90% as a function of the diameter and the contact angle of the photoresist. This shows that isotropic etching is a limitation to the fabrication of high microlenses as the footprint is significantly reduced. If the etching process cannot be adapted to reduce the isotropic component, one other option would be to use a photoresist with a lower contact angle.

Figure 4.10 presents the example of an aspheric microlens etched by an isotropic etching

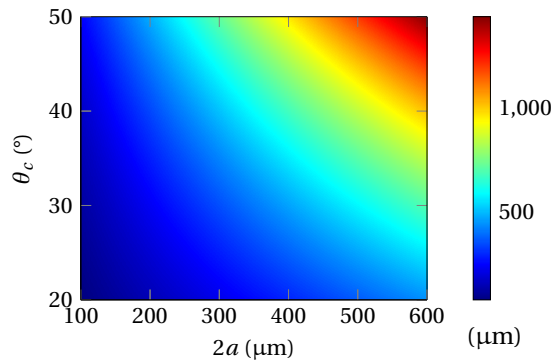


Figure 4.9 – Minimum achievable ROC of a spherical microlens manufactured by isotropic etching ( $\Sigma = 1$ ) under the condition that its clear aperture is at least 90% of the diameter. The ROC value is given as a function of the diameter  $2a$  and the contact angle  $\theta_c$ . A resist with a smaller contact angle can be used to attenuate the effective aperture reduction.

process. The concave part of the profile reduces the effective aperture of the microlens. By using Eq. (4.17), the clear aperture is about found to be about  $500\mu\text{m}$ , which corresponds to the measured one. This suggests that the etching is almost entirely isotropic. In terms of slope, this is translated into a sudden change of value. A sudden curvature change is also noted, which demonstrates that the outer part of the microlens is concave. Also, the value of the local concave ROC is almost constant and about  $70\mu\text{m}$ , see Fig. 4.10c, which corresponds to the sag of the etched microlens  $h_s$ , confirming again that the etching process is isotropic.

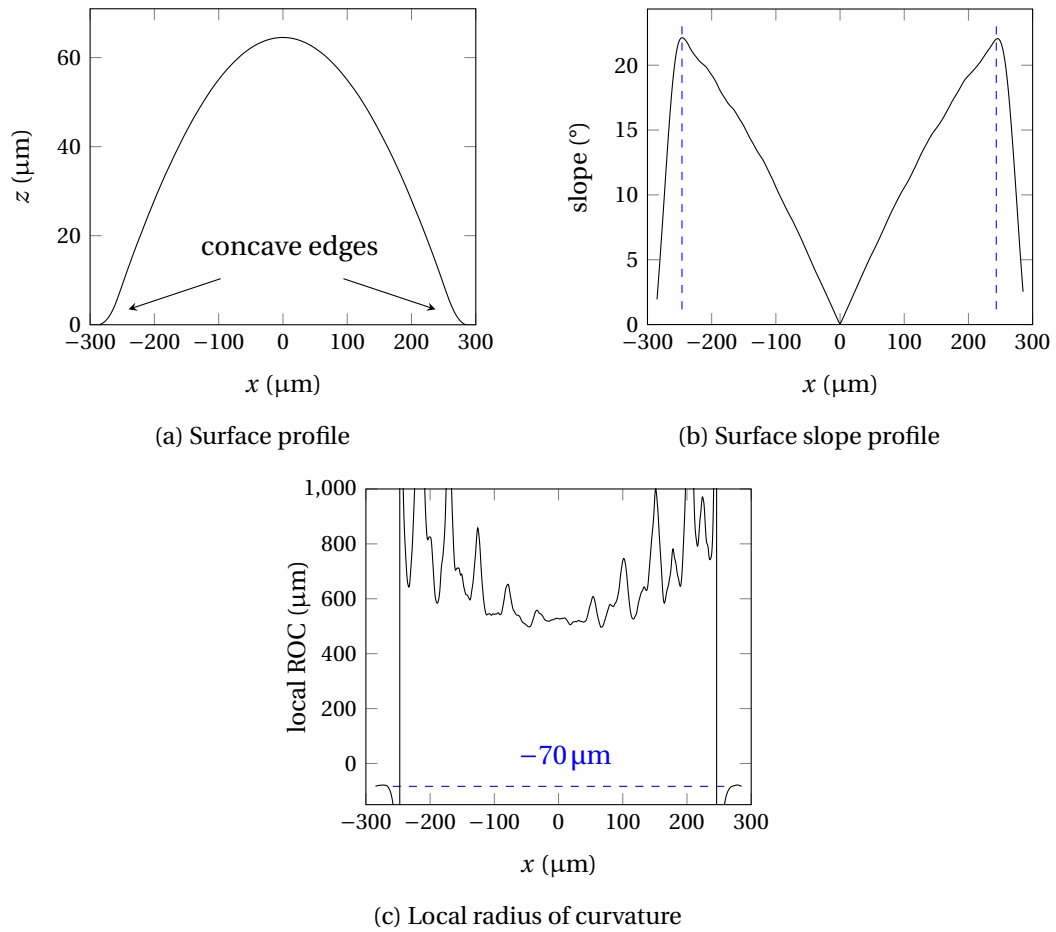


Figure 4.10 – Example of an aspheric microlens (diameter  $2a = 600\mu\text{m}$ ,  $R = 525\mu\text{m}$ , and conic constant  $\kappa = -2.5$ ) created by an isotropic etching process. (a) The concave part of the profile reduces the effective aperture of the microlens, which is no more equal to the diameter. (b) This effect is translated into a sudden change of slope value (blue dashed lines). (c) A sudden curvature change, from positive to negative values, is also noted. This confirms the concavity of the microlens outer part. This change can be used to determine the effective aperture, which is about  $500\mu\text{m}$  in this case. We also note that the value of the local ROC is about  $-70\mu\text{m}$  at the edges. This value corresponds to the etched microlens height  $h_s$ , confirming that the etching is isotropic.

### 4.3.3 General case

An arbitrary RIE process contains a directional and an isotropic component and can be modeled by the addition of the two. In the models we derive for the directional and isotropic etching, the selectivity is in both cases the ratio of the slopes. So, at the interface the selectivity remains the ratio of the slopes:

$$\Sigma(r_i) = \frac{s'_r(r_i)}{s'_s(r_i)}. \quad (4.18)$$

However, the relation between  $r_i$ ,  $r_r$ , and  $r_s$  is unknown this time. To determine it, one could use the average ratio of isotropic to directional etching to estimate the relation between the different radial positions by considering a superposition of the two effects. A way to determine this ratio is by measuring the radius of curvature of the concave part of the microlens  $R_{cve}$  or, equivalently, the aperture reduction. This ratio  $\eta_e$  is given by:

$$\eta_e = \frac{R_{cve}}{h_s}. \quad (4.19)$$

This could be used to solve the issue **A**. In situation **B**, the link between  $\delta i(t) \rightarrow \delta \Sigma(r_i)$  must be found. Again, a sinusoidal perturbation can be used. It has to be remarked first that,

$$\delta \Sigma = -\frac{s_r}{s_s'^2} \delta s_s', \quad (4.20)$$

and thus, instead of deriving the selectivity, it is possible to directly obtain the final surface slope change as a function of the input parameter change:  $\delta i(t) \rightarrow \delta s_s'(r_s)$ . This shows that an intermediate derivation of the selectivity is not necessary for the task of feedback in situation **B**.

Our formulation of the etching process requires only one input parameter  $i = i(t)$ . Alternatively, one could modify two or more parameters at the same time during the etching process. However, from all these derivations, one can already see that optimizing a process with a single input is not trivial. Extending this approach to two or more parameters renders the task even more difficult because of the cross-correlations, thus resulting in more trials to determine the optimized process.

Here, the feedback process is seen as an optimization process. In such process, an educated guess for the starting point is needed. Here, we assume some background and experience that allows us to set the initial conditions, which should not be too far from the optimum. In that sense, the approach we propose is made for fine-tuning. However, fine-tuning is essential for optical surfaces that require an irregularity RMS below 100 nm to achieve diffraction-limited microlenses.

## 4.4 Uniformity improvement of microlens arrays (MLAs)

Microlens arrays (MLAs) usually consist of a collection of microlenses arranged in a 1D or 2D pattern and attached to the same substrate. In most applications, the microlenses can be seen as channels that have the same optical function. For this reason, all microlenses must have the same properties, in particular the same surface form. Within an MLA, the number of microlenses can reach several thousands. In order to manufacture such large MLAs, it is advantageous for time and cost reasons to use wafer-level techniques that fabricate all microlenses in parallel at the same time. The main drawback of these techniques is that the surface manufacturing of the individual microlenses cannot be controlled independently. An unavoidable consequence is a non-uniformity that appears throughout the MLA. This section aims to propose a method that reduces this non-uniformity and to demonstrate its effectiveness.

Again, we consider the well-established technique based on photoresist reflow with subsequent RIE. Indeed, it remains the most effective approach to manufacture large MLAs in fused silica or silicon. The machines used during the fabrication are made to process wafers with a diameter of up to 200 mm. Reasonably, we can expect that MLA with a spatial extension of a few millimeters may not be impacted by non-uniformity. Here, we present the case of a 100 mm × 100 mm MLA used as a part of a microlens projection lithography system [104]. The microlenses are made in a fused silica substrate and are aspheric with nominal parameters  $R_n = 253\mu\text{m}$ ,  $\kappa_n = -1.02$ , and diameter  $2a = 315\mu\text{m}$ . Moreover, they are arranged in a hexagonal lattice to maximize the fill factor.

The wafer non-uniformity is induced by all steps of the fabrication process illustrated in Fig. 1.3. Firstly, the photoresist spinning produces a non-uniform thickness of the resulting layer. Then, the illumination is not perfectly uniform, which means that after development, the resist pillars do not have the same volume, and thus the resist microlenses have different ROCs after reflow. Finally, the etching process takes place in a chamber that has a finite size. The electromagnetic field, the temperature, and the plasma present spatial variations, which provoke an etching rate that depends on the position. All these parameter variations are combined and provoke a non-uniform distribution of aspheric surfaces within the MLA. To simplify the discussion of the proposed correction method and allow a graphical representation, we represent the aspheric surfaces by only two parameters instead of by a continuous function. They can be the ROC  $R$  and the conic constant  $\kappa$  or equivalently, see Section 2.3.1, the defocus  $c_4$  and the primary spherical  $c_{11}$ . This restriction can, however, be suppressed without any difficulty.

Figure 4.11 illustrates the non-uniformity after the resist reflow step. The ROC difference  $\Delta R = R - \bar{R}^1$  and the RMS surface form deviation for the spherical resist microlenses are provided in Fig. 4.11a and Fig. 4.11b respectively. This non-uniformity is already the combination of variations in the resist thickness, the illumination, and the development process.

---

<sup>1</sup>The bar notation means the average over the MLA.

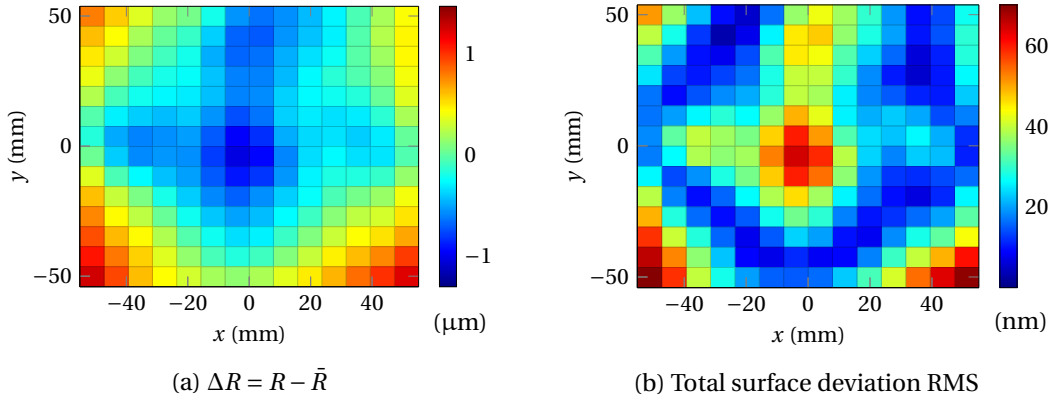


Figure 4.11 – Evidence of the non-uniformity after the photoresist reflow process. The MLA sampling consists of measuring 225 microlenses out of  $\sim 10^5$ . Variations of the resist thickness layer and the illumination are the leading causes.

Figure 4.12 illustrates the non-uniformity for the completed etched MLA. The ROC difference is shown in Fig. 4.12a, the conic constant difference in Fig. 4.12b and the RMS surface form deviation for the fused silica microlenses in Fig. 4.12c. The comparison between the total surface deviation RMS and  $\kappa$  shows that the non-uniformity is mainly translated into the conic constant variation as the distributions present the same circular shape. We explain this radial symmetry by the geometry of the plasma chamber. Also, by comparing the total surface deviation RMS of the resist microlenses, Fig. 4.11b, to the etched microlenses, Fig. 4.12c, we observe that the non-uniformity is more important at the end of the fabrication. The RIE step is thus the primary source of variations in this example.

In order to compensate for this variation, one parameter of the process must be changed locally. However, since all microlenses are processed in parallel, there is only one feature that can easily be changed at the scale of one microlens: the photo-mask design. From the reflow study, we know that it is possible to change the ROC of the resist microlens by modifying its volume, either by gray-scale lithography, by modifying the resist layer thickness, or by modifying its diameter. The resist layer thickness cannot be modified locally, so the two other options remain. The gray-scale lithography is likely the ideal method as the diameter can be kept at its nominal value, thus preserving the fill factor. However, it is more difficultly implementable than a simple diameter change, as the link between the photo-mask structure and the volume reduction is likely to be position-dependent and should thus be assessed experimentally. For this reason, we choose to use the diameter change as the tunable parameter.

From the considerations about the resist reflow, the change of volume resist only affects the ROC value, meaning that it is only possible to act on the symmetrical radial components of the final surface. Since even order components above  $c_4$  have low amplitude, it is reasonable for them to be neglected. This is a justification why using only the two parameters  $R$  and  $\kappa$  to represent the surface is reasonable.



#### 4.4. Uniformity improvement of microlens arrays (MLAs)

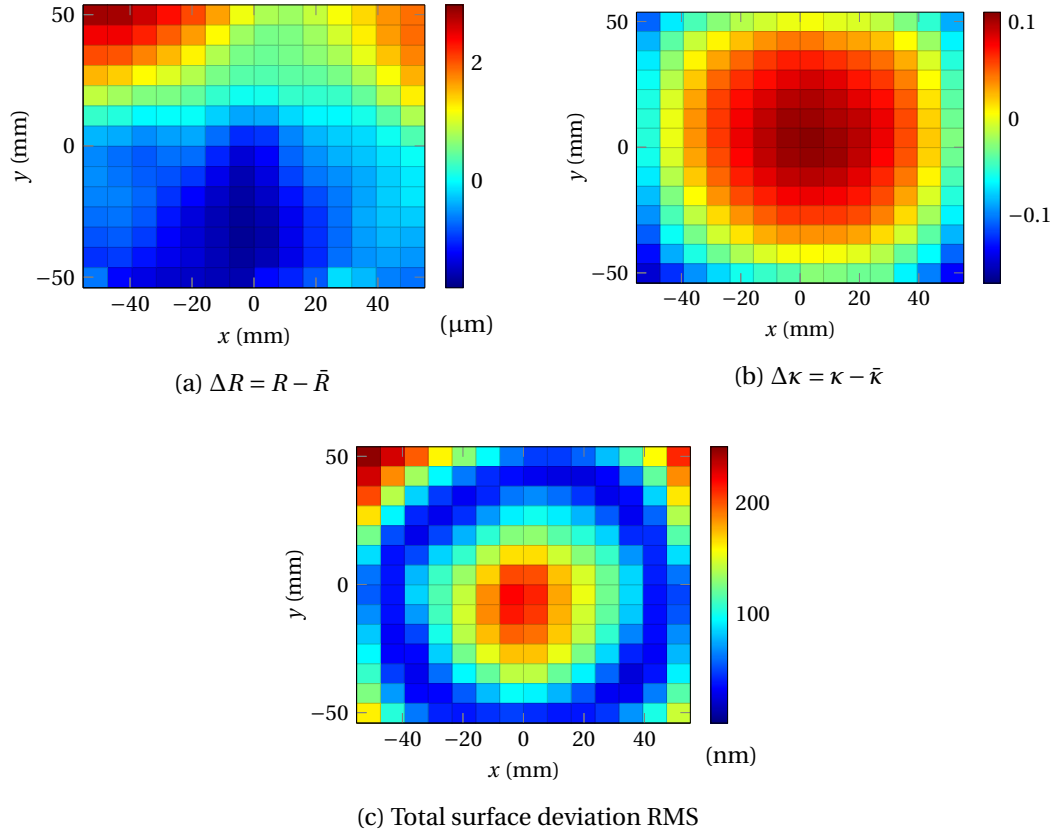


Figure 4.12 – Evidence of the non-uniformity after the RIE process. By comparing (b) and (c), we note that the non-uniformity is mainly translated into a dispersion of conic constant. Also, by comparing the total surface deviation RMS after reflow, one notes that the etching process is the primary source of the variations. The radial symmetry is likely explained by the geometry of the reactor.

##### 4.4.1 Methods

Now that we have identified a means to leverage the form of the etched microlenses surface, we have to address the following question: what diameter change should be applied to increase the MLA uniformity? Formally, the problem we want to solve is nothing else than an optimization. The goal is to determine the resist volume change  $\Delta V_c$  that we have to apply in order to minimize a loss function representing the non-uniformity.

Thus, we first have to define the non-uniformity quantitatively. As previously mentioned, the final interest is that all microlenses behave the same way from an optical point of view. By looking at the total surface deviation RMS provided in Fig. 4.12c, we can estimate that the aberration level caused by the non-uniformity is far from the diffraction-limited threshold and, thus, the optical performance is well represented by the RMS spot size. From Section 2.3.2, we know that this quantity is almost perfectly correlated to the RMS slope deviation. Consequently, both quantities are equivalent to solve this optimization problem. For convenience, we thus

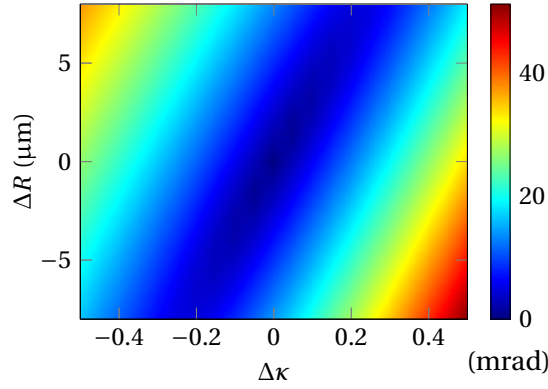


Figure 4.13 – Total slope deviation RMS as a function of the differences  $\Delta R = R - R_n$  and  $\Delta \kappa = \kappa - \kappa_n$ , calculated from the nominal values. All microlenses along the blue diagonal have the same focal length.

define the non-uniformity  $L$  (loss function) as the RMS slope deviation.

What is still to be specified is the reference used to calculate the slope deviation. Intuitively, we may think that we should use the nominal surface. However, we only want to correct the non-uniformity. It means that we assume that the process is already optimized in the sense that  $\bar{R} \approx R_n$  and  $\bar{\kappa} \approx \kappa_n$ . However, it is clear that from wafer to wafer, there are some unavoidable variations, of which the correction we apply must be independent. For this reason, the slope deviation is calculated based on  $\Delta R = R - \bar{R}$  and  $\Delta \kappa = \kappa - \bar{\kappa}$ . Figure 4.13 shows the RMS slope deviation for a typical dispersion of ROC and conic constant values. Qualitatively, the combinations of  $R$  and  $\kappa$  that follow the blue diagonal have similar optical performance, meaning the same focal length. More discussion about these considerations can be found in Section 2.3.1. Figure 4.14 illustrates the loss function across a MLA.

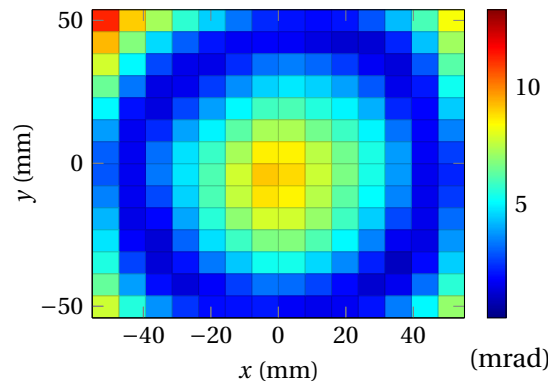


Figure 4.14 – Non-uniformity across the MLA as defined as the total slope deviation RMS. Same example as in Fig. 4.12.

#### 4.4. Uniformity improvement of microlens arrays (MLAs)

Now that we have defined the loss function  $L = L(\Delta R, \Delta \kappa)$ , we have to find the relation that connects the input parameter  $\Delta a$  to the process output parameters  $\Delta R, \Delta \kappa$ ,

$$\Delta a \xrightarrow{\text{reflow}} \Delta R_r \xrightarrow{\text{RIE}} (\Delta R, \Delta \kappa), \quad (4.21)$$

through the difference of microlens resist ROC  $\Delta R_r$ . From the study of the resist reflow, we know that

$$\Delta R_r = C \cdot \Delta a, \quad (4.22)$$

with  $C$  a constant. The RIE process cannot be represented explicitly, but it is determined as explained in Section 4.3. We name it  $\Upsilon = \Upsilon(\Delta R_r)$

At this point, it may be useful to clarify the dependency of all these functions on the substrate position  $(x, y)$ . The reflow process does depend on the position only through the resist layer thickness  $h_c$ , and the constant  $C$  can thus be considered independent on the position as it is confirmed in Fig. 4.3a, which presents data from all wafer positions. On the other hand, the RIE process is a function of the position. As already discussed, the temperature and plasma composition are different for distinct positions. The comparison between Fig. 4.11b and Fig. 4.12c shows that the shape of the non-uniformity changes during the RIE process. Practically, this means that the function  $\Upsilon$  must be determined for each microlens position and that the optimization process must be performed independently for each microlens.

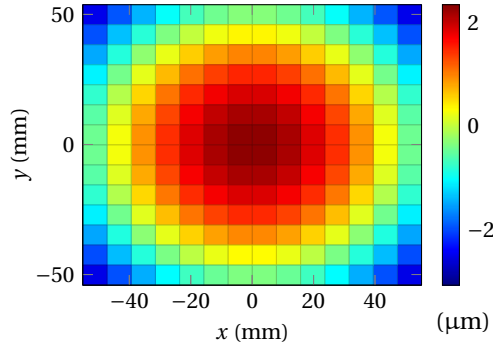


Figure 4.15 – The calculated semi-diameter change  $\Delta a$  that minimizes the non-uniformity defined by the total slope deviation RMS. The semi-diameter change function has a radial symmetry similar to the one that is observed in Fig. 4.13. The maximum semi-diameter change is about  $5 \mu\text{m}$ .

The optimization problem is thus defined by the determination of the function  $\Delta a_0(x, y)$  such that:

$$L(\Upsilon(C\Delta a_0(x, y), x, y)) \leq L(\Upsilon(C\Delta a(x, y), x, y)) \text{ for all } \Delta a(x, y). \quad (4.23)$$

This operation is realized numerically. The result of the optimization, the change of diameter as a function of the MLA position, is presented in Fig. 4.15.

### 4.4.2 Results and discussion

Based on the diameter change calculated in the previous section and presented in Fig. 4.15, a new photo-mask is created. New MLAs are then manufactured with this new photo-mask but by using the same process as before.

Figure 4.16 shows the non-uniformity of the ROC  $R$  and the conic constant  $\kappa$ . The comparison with Figs. 4.12a and 4.12b shows that the conic constant distribution is not really modified by the correction procedure, whereas the  $R$  distribution is clearly impacted. The  $R$  and  $\kappa$  distributions are now quite well correlated to each other. This is expected since the change of the loss function provoked by a difference of conic constant can be compensated by a well-chosen change of ROC, as seen in Fig. 4.13.

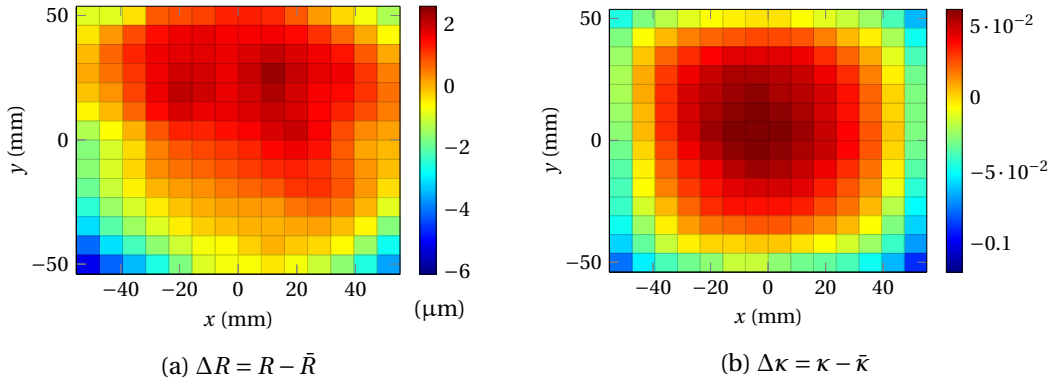


Figure 4.16 – Example of the  $R$  and  $\kappa$  distribution across a completed MLA after the correction procedure. The conic constant variation is not impacted by the correction procedure, whereas the  $R$  distribution is entirely different. It is now well correlated to the  $\kappa$  distribution as one expects.

To evaluate the uniformity improvement, we have to look at the RMS slope deviation, which is the loss function. Figure 4.17 presents an example of corrected and uncorrected MLA. In the uncorrected case, the radial non-uniformity is visible but has completely disappeared in the corrected case. The improvement is clearly observed.

To more accurately assess the improvement, the RMS slope deviation is calculated for 10 MLAs, 5 uncorrected and 5 corrected, and then compared. Visually, the improvement can be observed in the  $R/\kappa$  space, see Fig. 4.18. The corrected distribution (green) is aligned along the diagonal of reduced cost, whereas the uncorrected distribution (red) has no well defined principal component. This plot also shows that it is the ROC that is impacted by the correction procedure and not the conic constant in this particular example.

#### 4.4. Uniformity improvement of microlens arrays (MLAs)

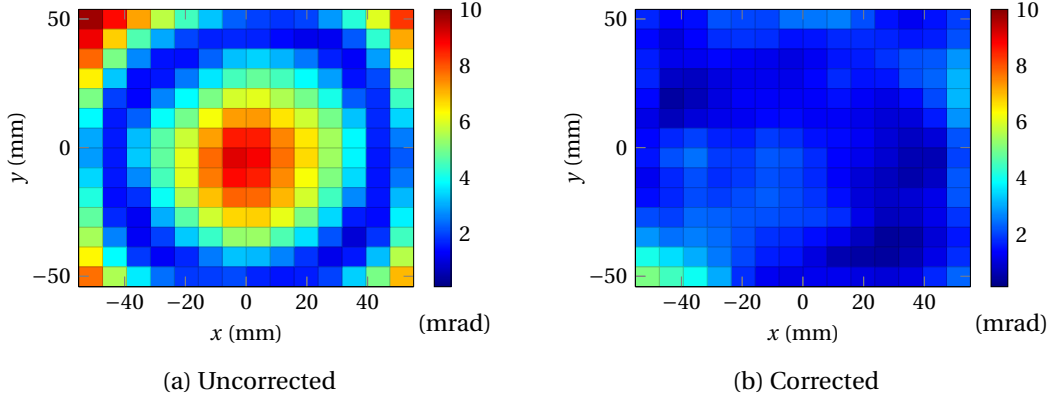


Figure 4.17 – Comparison of the loss function value across an example MLA before (a) and after (b) the correction procedure. A clear improvement is observed.

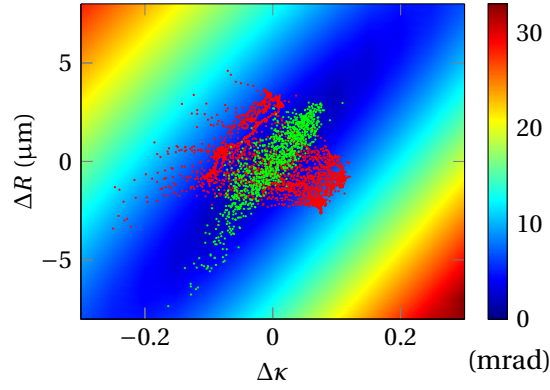


Figure 4.18 –  $R/\kappa$  distribution of 5 uncorrected (red) and 5 corrected (green) MLAs. The corrected distribution is now aligned along the blue diagonal that represents the loss function minimum.

To quantitatively score the improvement, the empirical distributions of the loss function are compared for these 10 MLAs, see Fig. 4.19. On average, the RMS slope deviation is 4.93 mrad before correction and 1.48 mrad after correction. This is an improvement by a factor of 3.3. To look at the extremes of the distribution, we can also determine the value of the RMS slope deviation that comprises 95% of the distribution. It is 8.4 mrad in the uncorrected case and 3.1 mrad after correction. This is an improvement by a factor 2.7. These numbers demonstrate the effectiveness of this method on average, but also in terms of extreme cases.

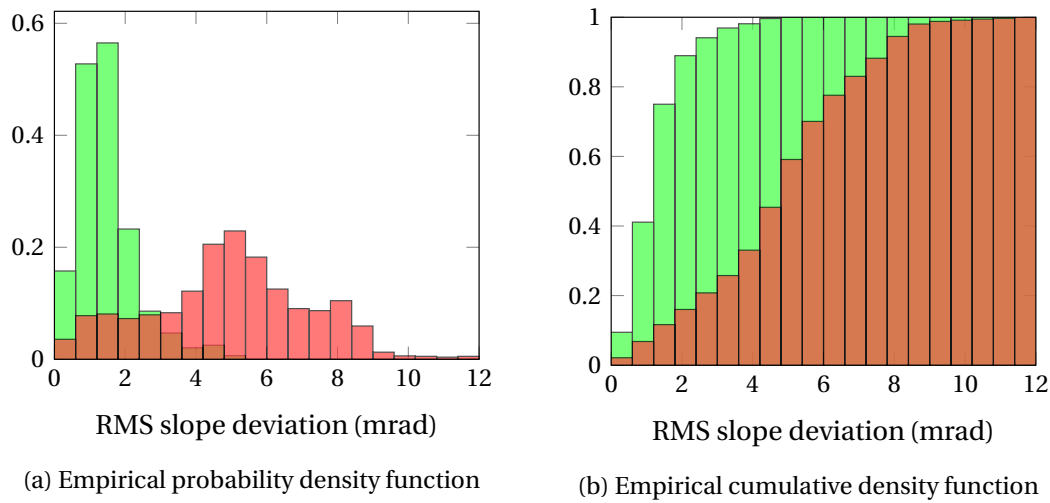


Figure 4.19 – Empirical distribution of the loss function for 5 uncorrected (red) and 5 corrected (green) MLAs. Distribution means are 4.93 mrad and 1.48 mrad, respectively. 95% of the microlens are below 8.4 mrad in the uncorrected case and 3.1 mrad in the corrected case. Both number show an effective improvement of the uniformity.

These numbers show that the procedure is effective to reduce the non-uniformity. However, the cost of the method in terms of money and time is also essential for its practical implementation. To discuss it, we summarize first the steps involved in the procedure:

1. Measurement of the resist and etched microlenses surfaces for a MLA manufactured with a stable process.
2. Process modeling based on the surface measurements.
3. Determination of the diameter change by optimization.
4. Creation of a photo-mask with modified structures.

Then, new MLAs can be processed. The measurement of the resist and etched microlenses is usually a familiar process. The new steps involved in this method are the modeling of the process and the optimization, which consist only of a software analysis. They may, however, require some time and competences to be done correctly. Besides working time, the cost of the method is due to the new mask that has to be ordered. In terms of time, the entire procedure should take at least a few days.

The idea to modify the resist volume to change the spherical cap curvature and, finally, to change the curvature of the completed microlens could be used to compensate for another issue. Indeed, within an MLA, the microlenses at the edges, that miss one or several neighboring microlenses, usually present differences compared to the inner microlenses, see Section 2.3.3.

For instance, this results in quite a large difference in ROC, which is usually compensated by designing dummy microlenses. The proposed method could be an interesting alternative.

The procedure described here, namely determining a loss function and one or more tunable parameters, modeling the fabrication process, and determining by optimization the best input parameters, applies to any manufacturing process, and other fabrication techniques of MLA in particular. We can mention that MLA manufactured by UV imprinting are also subject to non-uniformity caused by mold deformation and polymer shrinkage [105]. When the master mold is created by direct writing, the surface itself can be modified without restriction, allowing, in theory, a perfect compensation for these effects. For this, accurate process modeling is required, which is not trivial.

In order to improve the method, grey-scale photolithography could be used instead of changing the diameter. Also, using a direct-writing based master mold and replication could replace the reflow process for the creation of resist microlenses and thus be combined with RIE for further uniformity improvement of silicon or glass MLA.

## 4.5 Conclusion

In this chapter, we intend to model the microlens fabrication process by resist reflow with subsequent reactive ion etching. As a full model that allows complete predictability is impossible to achieve, we use a more practical approach based on trial and error, in other words, based on process optimization. However, since the number of parameters is huge, we use empirical models that we calibrate with experimental measurements to obtain estimations of the gradient in order to ensure and speed up the descend towards the optimum.

More concretely, we model both the resist reflow and the RIE process. First, we establish the conditions to obtain a spherical cap with resist reflow. Then, from this ideal case, we show how the ROC of the resist microlens changes as a function of the input parameters, namely the microlens diameter and the resist thickness layer.

For the RIE process, we model the directional and isotropic etching separately and then combine the results. In particular, we show that the ratio of the slopes between the resist and the etched microlens is an indicator of the etching selectivity. Based on this and further developments, we propose strategies to optimize the RIE process, which is usually represented by a continuous parameter function of time.

We demonstrate the validity of these models as we use them to increase the uniformity of a large MLA. Indeed, a controlled change of the microlens diameter allows to modify the resist microlens ROC and compensate for etching variations. The uniformity is improved by a factor  $\sim 3$ .

With these models, we can also estimate the fundamentals limits of the photoresist reflow with subsequent RIE approach and what are the origins of these limitations. We identify mainly the

photoresist layer thickness that can be dispensed and the isotropic component of the etching process, which significantly reduces the microlens aperture. Overcoming these limitations could be realized by replacing the resist reflow by a UV imprinting step based on freeform mastering.



## 5 Microlens Characterization in Transmission

The characterization of high NA microlenses by surface measurements in reflection is no more possible because of the steep surface slopes. As a possible alternative, we present and discuss measurements of the PSF and of the wavefront performed in transmission. In particular, we evaluate how these measurements can provide information about the surface for fabrication process optimization and about the optical performance for quality evaluation.

### 5.1 Introduction

A convenient way to characterize microlenses is by measuring their surface in reflection using optical surface profilers such as confocal microscopes or CSIs. However, for high NA microlenses, the required steep surfaces prevent the reflected light from being collected by the imaging system (microscope objective) of these instruments. Alternatives are the use of higher magnification microscope objectives with smaller FOVs combined with image stitching or the use of mechanical contact profilers. However, both approaches are rather slow. An alternative that takes into consideration this drawback is to work in transmission and thus directly examine the optical functionality of the microlens. One obvious condition is to use, for the test, a wavelength in the transparent range of the material. This thus prevents the measurement in transmission of silicon microlenses with visible light. However, this condition is not a very strong drawback since most silicon microlenses are flat due to the high refractive index ( $n \sim 3.5$ ) and can usually be characterized by surface measurements without difficulty. This approach is thus considered for glass or plastic microlenses used in the visible or ultraviolet (UV) range.

The full information about the function of a lens is included in the field scattered by this lens. Phase and irradiance measurements allow probing selected optical functions of the lens. Here, we consider the well-known wavefront [35, 58, 106, 107] and PSF measurements [108–110]. We discuss both approaches and determine what pieces of information can be obtained. In particular, we discuss for both of them the possibility to evaluate the microlens optical quality and to obtain information for fabrication process optimization, the two purposes of

the characterization. The novelty of the work presented here lies in three points: firstly, we consider high NA aspheric microlenses. Secondly, we discuss the analysis of the measurements, which is rarely done. Finally, we present a method to reconstruct the surface. Usually, only the ROC is derived as a geometrical parameter.

This chapter starts with a description of the setup used to perform the measurements of the PSF and the wavefront, Section 5.2. PSF measurements and their analysis are then discussed in detail in Section 5.3. Similarly, Section 5.4 discusses the phase measurements and subsequent processing. Finally, the principal results and conclusions are summarized in Section 5.5.

### 5.2 Experimental setup

In order to perform PSF and wavefront measurements, we use a high-resolution interference microscope with spectral resolution [111]. The schematic of the setup is presented in Fig. 5.1.

The working principle is derived from a Mach-Zehnder interferometer and allows recording irradiance and phase [112–115] at a desired wavelength and position after the microlens. The light source of the setup is a supercontinuum (SuperK Fianium, NTK Photonics), and the operating wavelength is selected by an optical variable filter within the range of 480–840 nm. An optical delay line sets the optical path difference between the object and reference arms to zero. Indeed, the optical path of each arm varies through different wavelengths because of the dispersion of the optical components. A piezo mirror is deployed to vary the optical

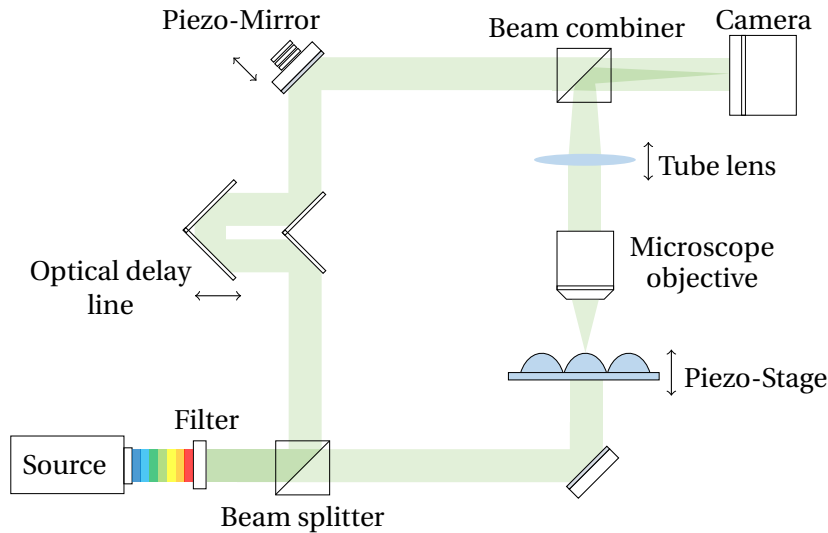


Figure 5.1 – Schematic representation of the high-resolution interference microscope. The field scattered by a sample, a microlens in this case, can be recorded in a specific volume thanks to irradiance and phase measurement. This allows for PSF and wavefront measurements.

path length of the reference arm, inducing the phase shifts that are necessary for the five-steps phase-shifting interferometry technique [116, 117] that is used to extract the phase information. Equivalently, digital holography could be used for this operation [118]. An additional piezo stage that moves the sample allows us to run measurements at different positions along the optical axis. The position of the tube lens corrects residual wavefront errors of the objective so that a flat phase profile can be achieved on the camera when no sample is present.

### 5.3 Point spread function (PSF) measurements

The point spread function of a lens is the response provided by this lens to a point source. When the lens is not aberrated, the shape of the PSF is only the result of the diffraction caused by the lens aperture [50]. For a circular aperture, it is represented in the focal plane by the well-known Airy pattern [119]. The diffraction-limited PSF is thus the best achievable case, and the comparison of a measured PSF to the ideal one is an indicator of the lens quality.

Figure 5.2 presents the measured PSF of a low (0.14) and high (0.4) NA microlenses illuminated by a plane wave, see Fig. 5.1. For the low NA spherical microlens, the measurement presents an almost ideal PSF as it is symmetrical. On the other hand, for the high NA spherical microlens, a spherical aberration is detected, which is expected.

This spherical aberration is the reason why aspheric surfaces defined as conic sections are used, see Section 2.2.1. However, the conic constant value that has to be set is a function of the object position and of the refractive index  $n$ . Figure 5.3 shows the optimized conic constant for an on-axis object as a function of the distance  $d$  between the microlens vertex and the object. For such an imaging case, the conic constant is included in the interval  $[-n^2, -1/n^2]$ .

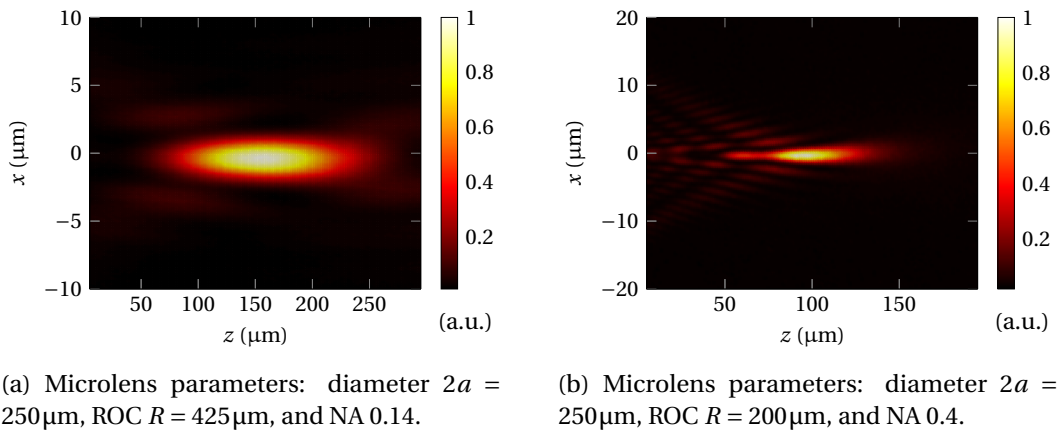


Figure 5.2 – Measured irradiance at the focal spot for low (a) and high (b) NA spherical microlenses. When the NA is low, the spherical aberration is not visible, and the focal spot is close to the ideal one. For the high NA microlens, spherical aberration is visible, and the PSF is no more symmetrical.

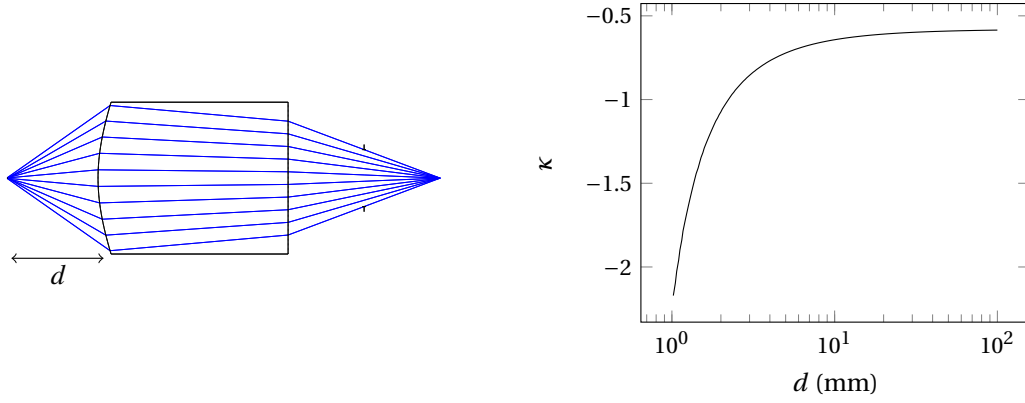


Figure 5.3 – Optimized conic constant values that allow for an almost aberration-free image of an on-axis point source as a function of its distance  $d$  from the microlens vertex. Microlens parameters: ROC  $R = 500\mu\text{m}$ , diameter  $2a = 500\mu\text{m}$ , substrate thickness  $T = 500\mu\text{m}$  and refractive index  $n = 1.5$ . The conic constant value can be significantly different whether the object is placed at infinity ( $\kappa = -0.6$ ) or at the front focal plane of the lens ( $\kappa = -2.25$ ).

The fact that an aspheric surface suppresses the spherical aberration only for on-axis objects placed at one specific position shows that testing a lens with another illumination provokes artificial aberration. The testing configuration must thus be equivalent to the working configuration for the correct PSF to be recorded. Thus, instead of illuminating the microlens with a plane wave, a point source can be placed at the correct distance  $d$ . This can be realized by using a single-mode fiber.

On top of that, the correct wavelength must be used for testing because of chromatic dispersion. This can be realized using a supercontinuum as the light source, as described in Section 5.2. However, this condition limits the testing to the visible range, which is also the working range of the optical elements in the measurement setup. In particular, PSF measurement poses difficulty to characterize elements working in the UV range because of the lack of highly corrected optical elements made for UV light. In conclusion, PSF measurements are meaningful only when performed under proper working conditions.

### 5.3.1 Quality assessment

Based on PSF measurements, the optical quality of the lens is usually assessed by calculating the Strehl ratio [120]. It is the ratio of the irradiance peak value  $I$  of an image produced by an aberrated lens to the same quantity produced by a diffraction-limited lens,  $I_0$ . It is written::

$$SR = \frac{I}{I_0}. \quad (5.1)$$

In the framework of the Fraunhofer diffraction theory,  $I_0$  is expressed as

$$I_0 = \frac{P_0 A}{\lambda^2 f^2} = \frac{C \cdot A^2}{\lambda^2 f^2} = \frac{C \pi^2 a^4}{\lambda^2 f^2}, \quad (5.2)$$

with  $P_0 = C \cdot A$ , the power falling onto the aperture of area  $A$ ,  $C$  being the constant of proportionality when the illumination is uniform.

Most of the microlenses that are fabricated at SUSS MicroOptics have an irregularity RMS below 150 nm, which represents a wavefront error RMS smaller than  $\lambda/6$  for glass microlenses. At this level of quality, determining the Strehl ratio is still relevant, but this is not the case for microlenses of low quality [121].

Equation (5.2) shows that the derivation of the Strehl ratio requires the value of the aperture of the lens. The diameter of a microlens is usually fixed as a requirement of the design and well known. However, is the diameter equivalent to the aperture? As seen in Section 4.3 and illustrated in Fig. 5.4, microlenses fabricated by resist reflow with subsequent reactive ion etching possess a concave area at the microlens edge, which reduces the effective aperture. This raises the following questions: firstly, can the Strehl ratio still be derived using Eq. (5.2)? If yes, how to determine the aperture?

The aperture could intuitively be defined by considering the inflection point, where the slope decreases rapidly and which is close to a hard aperture definition. However, the profile has still to be measured to determine this value. An optical surface profiler cannot perform this operation in the case of high NA microlenses, and mechanical contact profilers have to be used. Moreover, on a single wafer and from wafer to wafer, the values of the individual microlens apertures vary caused by fabrication process variations. This imposes the measurement of all

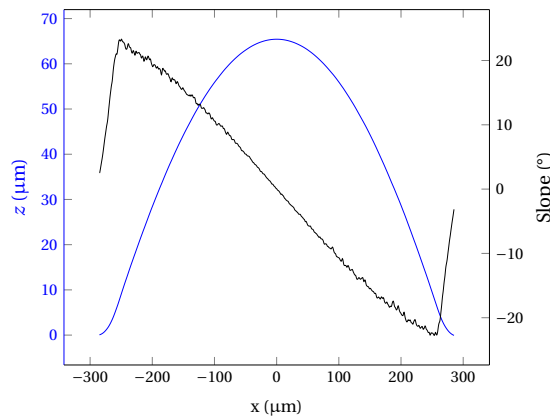


Figure 5.4 – Example of a measured microlens surface profile and slope. It illustrates the issue concerning the aperture definition for microlenses fabricated by reactive ion etching. Indeed, the continuous transition between the edges of the microlens that are concave and the convex part of the surface prevents the definition of a hard aperture.

of them. Indeed, for a Strehl ratio  $SR$ , a wrong aperture determination  $a + \delta a$  leads to a wrong Strehl ratio  $SR'$ , which is expressed as

$$SR' = SR \frac{1}{1 + 4 \frac{\delta a}{a}}. \quad (5.3)$$

This means that an error of 1% of the aperture value gives an error of 4% of the Strehl ratio. Like this, Strehl ratios above 1 are derived when  $\delta a$  is negative. In conclusion, this means that the PSF measurement alone cannot provide an accurate assessment of the microlens quality.

Another practical issue is the determination of  $P_0$ . Practically, it can be estimated by integrating the irradiance over all the camera when the measurement plane coincides with the focal plane. However, the light coming from outside the effective aperture also fall onto the sensor. This effect artificially increases the Strehl ratio and again adds uncertainty to its value.

In conclusion, even if the working conditions are reproduced, the quality of an RIE based microlens is not accurately assessed through PSF measurements.

### 5.3.2 Feedback for process optimization

The second purpose of the characterization is to obtain feedback in order to optimize the fabrication process. If we assume that the surface form of the microlens defines most of the optical functionality, i.e., we do not consider the substrate thickness variation or the material non-homogeneity, the goal is thus to determine the surface change that has to be applied to obtain the ideal performance.

Besides the focal length that is linked to the microlens ROC, it is challenging to derive quantitative feedback from a PSF measurement. In Fig. 5.2, spherical aberration is clearly visible for the high NA microlens, but it is difficult to estimate how much surface deviation this represents. Furthermore, this case is quite obvious, but when the amplitude of the aberration is smaller, and the type of aberration is of a higher order, this task becomes even more difficult. We do not claim this is not feasible, but we emit doubts.

In conclusion, quality testing of high NA microlenses through PSF measurements is quite restrictive. Indeed, it requires that the testing conditions are equivalent to the working conditions. Also, it is difficult applicable for RIE microlenses because the diameter does not correspond to the aperture, which has to be determined by a contact profilometer. Finally, we do not see the possibility of obtaining quantitative feedback for a fine optimization of the fabrication process.

## 5.4 Wavefront measurements

Measuring the output wavefront of a lens and determining the deviation from a reference - generally, a plane wave or a spherical wave - is a well-established and standardized technique to assess the quality of this lens [35, 122]. As mentioned in Section 5.3, for high NA microlenses, if the testing conditions are not similar to the working conditions, artificial aberrations appear. However, in the case of phase measurement, one can find workarounds in order to suppress this condition.

The PSF is the consequence of the diffraction and is the result of a complex integral calculation performed over the lens aperture. On the other hand, the wavefront can be explained mainly by geometrical optics and can be seen in a first approximation as a simple addition of phase shifts without spatial dependence. Indeed, within the framework of the thin element illuminated by a plane-wave, the phase  $\phi$  at the exit pupil induced by a surface sag  $s$  is given by:

$$\phi(x, y) = k(n - 1)s(x, y). \quad (5.4)$$

This shows that in this particular regime, the reference wavefront is of no importance as a surface deviation  $\Delta s$  provokes a wavefront aberration  $\Delta\phi$  which is not a function of the target surface, thus of the reference wavefront.

For high NA microlenses, the bending of the rays cannot be neglected anymore and has to be taken into account. From Section 2.3.2, we know that the phase at the exit pupil becomes:

$$\phi(x', y') = ks(x, y) \left( n - \sqrt{1 + m_x^2(x, y) + m_y^2(x, y)} \right), \quad (5.5)$$

with  $m_{x,y}$  the slope of the ray after refraction,  $x' = x - m_x s$ , and  $y' = y - m_y s$  the coordinates in the exit pupil. However, in this case, the wavefront aberration depends on the reference wavefront  $\Delta\phi = \Delta\phi(\Delta s, \phi_0)$  because of the terms that take the slope of the rays into account. We can nevertheless note that the wavefront component that depends on the reference wavefront is smaller than the linear part. This offers the possibility to use a perturbative approach and thus use the wavefront provoked by the ideal surface under testing condition  $\phi_0^t$  as a reference:

$$\Delta\phi = \phi - \phi_0 \approx \phi^t - \phi_0^t. \quad (5.6)$$

In other words, it is possible to use a plane wave illumination to characterize microlenses that are not designed to work under this illumination if we accept the drawback to lose some accuracy. However, the knowledge of  $\phi_0^t$  is required, which can be determined by Eq. (5.5) or by any simulation software. To illustrate this, Fig. 5.5 presents a simulation that compares a chosen wavefront aberration and its approximation under plane wave testing for a typical aspheric microlens that is not designed to work under plane wave illumination ( $\kappa = -1.5$ ). The

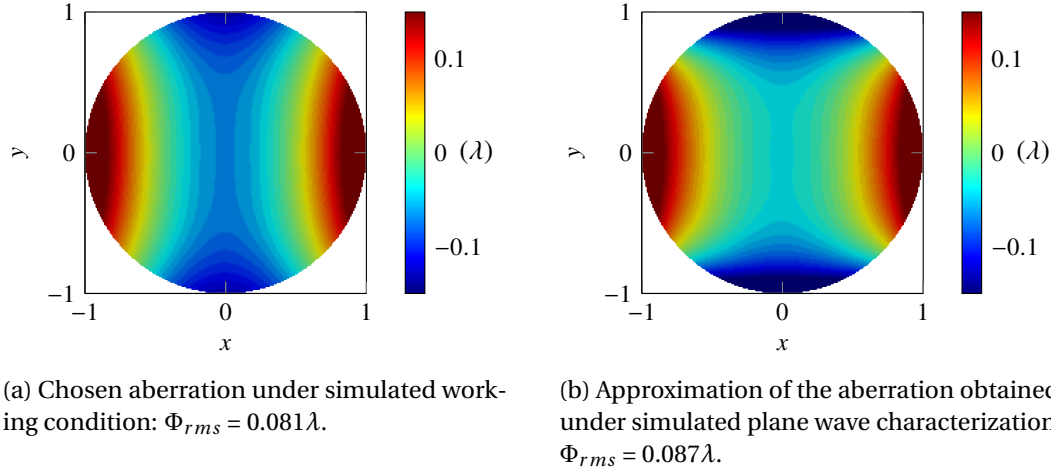


Figure 5.5 – Comparison between a simulated wavefront aberration and its approximation by Eq. (5.6). The amplitude and shape of these two wavefront aberrations are similar. Microlens properties:  $R = 0.5$  mm,  $\kappa = -1.5$ , diameter  $2a = 0.5$  mm, substrate thickness  $T = 0.5$  mm and refractive index  $n = 1.5$ .

amplitude and shape of the wavefront are similar which shows that this approach can be used for testing the quality of the microlens.

#### 5.4.1 Quality assessment

To illustrate this quality testing method, an interferometric measurement of a microlens is presented. The microlens, made in Borofloat®33, is fabricated at wafer-level using photoresist reflow with subsequent reactive ion etching. This specific microlens is chosen for three reasons: firstly, because of its physical parameters (sag =  $38\mu\text{m}$ , aperture =  $180\mu\text{m}$ ,  $R = 150\mu\text{m}$ , paraxial effective front focal length  $\sim 300\mu\text{m}$ ,  $n = 1.476$  at  $\lambda = 550\text{nm}$ ), its NA of  $\sim 0.4$  is one of the highest for such fabrication method. Secondly, this microlens is chosen because it has no hard aperture, thus allowing to illustrate the issue presented in Section 5.3. Finally, this microlens is spherical thus highly aberrated ( $\Delta\phi_{rms} > 0.5\lambda$ ), which allows to evaluate the method far from the ideal case.

The phase is recorded on a plane situated at a position  $z_m$ , between the microlens vertex and the front focal spot, where all the phase information can be recorded on the camera without limitation caused by the field of view, see Fig. 5.6. This renders the procedure pretty insensitive to the microlens diameter since there is always a position where the entire phase information can be recorded whatever the field of view provided by the imaging system. The NA of the microscope objective can thus be freely chosen to be above the NA of the tested microlens. In this particular example,  $z_m$  is  $\sim 10\mu\text{m}$ . The microscope objective used for this measurement is a  $20\times$  apochromat NA 0.4 manufactured by Leica.



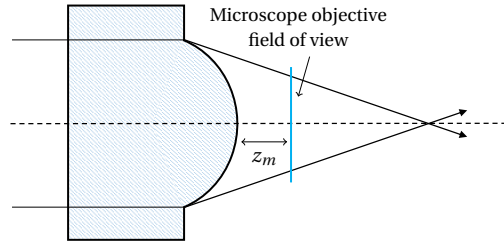


Figure 5.6 – Schematic of the measurement configuration. A plane wave is focused by the microlens and the phase is recorded at a position  $z_m$  where all information is included in the field of view of the microscope objective.

Figure 5.7a presents the wrapped phase. Figure 5.7b shows a cross-section of the unwrapped phase as well as its derivative. It can be observed that on a diameter of about  $160\mu\text{m}$ , the wavefront is convex and converges towards the focal spot. Outside this area, the wavefront deviates dramatically from a spherical wave. This is the translation of the aperture issue mentioned in Section 5.3. The sharp change in the wavefront derivative provides a convenient way to define the aperture of the microlens.

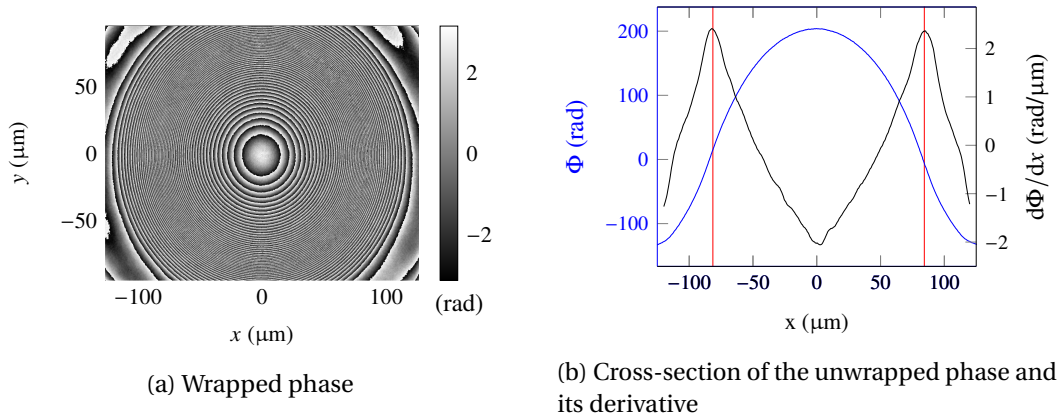


Figure 5.7 – Measured wavefront produced by the RIE based microlens. Measurement is performed with a  $20\times$  NA 0.4 microscope objective at  $\lambda = 550 \text{ nm}$ . The wavefront is convex and spherical at the center and concave at the edges. A smooth transition between the two regimes is observed.

From this phase measurement, the wavefront aberration is retrieved by subtracting a reference wavefront. Figure 5.8 presents the wavefront deviation from a spherical wavefront as well as its decomposition into Zernike polynomials. The RMS value of the wavefront aberration is  $0.55 \lambda$  and its PV value is  $2.24 \lambda$ . The wavefront aberration consists almost only of spherical aberration, which is expected for a spherical microlens.

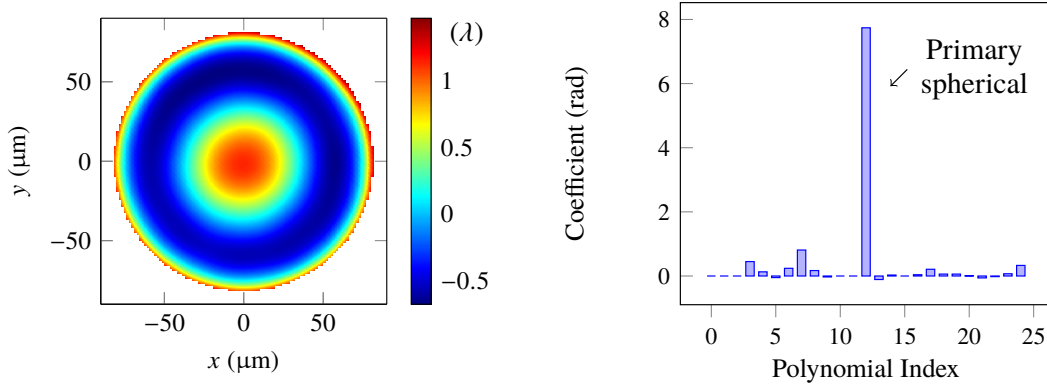


Figure 5.8 – Wavefront aberration from a spherical wave reference and its Zernike polynomials decomposition.  $\text{RMS} = 0.55 \lambda$ ,  $\text{PV} = 2.24 \lambda$ . Indices as in [123]. As expected for a spherical microlens, the main aberration is primary spherical.

#### 5.4.2 Feedback for process optimization

The second objective of the characterization is to obtain feedback for fabrication process optimization. In other words, we want to acquire information about the surface of the microlens.

When a plano-convex lens is thin and illuminated by a plane wave, a measurement of the phase at the exit pupil gives the surface directly, see Eq. (5.4). The generalization of this equation to high NA plano-convex lenses illuminated with a plane wave from the backside is explicitly derivable. In this case, the phase  $\phi$  at a position  $z_m$  is written:

$$\phi(x', y') = kns(x, y) + k(z_m - s)\sqrt{1 + m_x^2(x, y) + m_y^2(x, y)}. \quad (5.7)$$

This equation can be inverted to obtain the surface  $z = s(x, y)$ :

$$s(x, y) = \frac{\phi(x', y') - kz_m\sqrt{1 + m_x^2 + m_y^2}}{k\left(n - \sqrt{1 + m_x^2 + m_y^2}\right)}. \quad (5.8)$$

The wavefront measurement presented in Fig. 5.7 is used to reconstruct the surface of the microlens. First, the unwrapped measured wavefront is cropped and decomposed into the first 150 Zernike polynomials. This specific number is chosen for the decomposition to contain all the relevant surface information and to remove the noise. Then, the surface is obtained by using Eq. (5.8). In order to demonstrate that this approach is valid, the same microlens is also measured with a mechanical stylus profiler along the  $x$ -axis crossing its vertex. Figure 5.9 presents both the reconstructed and measured profiles. A good agreement between them is observed. To allow a better comparison between them, they are both fitted with the spherical equation, and their fit residuals (irregularity) are presented in Fig. 5.10. The reconstructed ROC

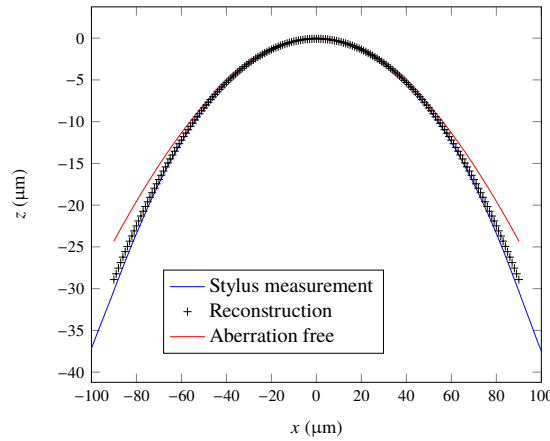


Figure 5.9 – Comparison between the stylus measurement (ROC  $R = 150.9\ \mu\text{m}$ ) and the reconstructed profile (ROC  $R = 152.5\ \mu\text{m}$ ). Even if these two surface profiles do not perfectly agree, they both provide similar feedback for fabrication process optimization.

value is in good agreement with the direct stylus measurement:  $R = 152.5\ \mu\text{m}$  vs.  $150.9\ \mu\text{m}$ . The RMS values of both irregularities are comparable,  $46.1\ \text{nm}$  vs.  $67.5\ \text{nm}$ , and their shapes are qualitatively similar. These results show the validity of the approach for surface determination.

The maximum usable numerical aperture of this microlens can be estimated based on the maximum slope of the surface, which is about  $37^\circ$ . This leads to a NA of almost 0.4. For this surface to be characterized in reflection, a microscope objective with a NA of at least 0.6 is required.

To reconstruct this surface, we require a plane wave illumination from the backside because we do not think that an analytical reconstruction of the surface is possible in the general case of a point source illumination. However, the goal is to obtain feedback for fabrication process

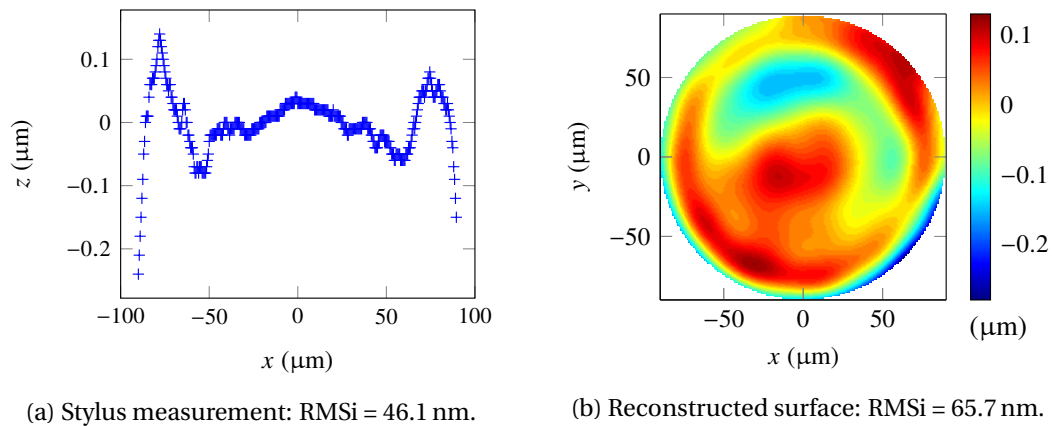


Figure 5.10 – Irregularity comparison between stylus measurement and reconstructed surface: the shape and amplitude are similar.

optimization. In reality, the surface form deviation with respect to the nominal surface is enough. In all configurations, an approximation of the surface deviation can be obtained using the thin element approximation:

$$\Delta s(x, y) = \frac{\Delta \phi(x', y')}{k(n-1)}. \quad (5.9)$$

The relation between  $(x, y)$  and  $(x', y')$  can be estimated using geometrical considerations in the aberration-free case. Even though this is only an approximation, it has to be noted that it converges to a surface deviation of zero when the phase deviation is zero. This means that this is usable in an optimization process, and this approximation does not alter the quality of the lens manufactured with the optimized process, maybe more trials are needed.

In the example we present, the measured wavefront aberration suffers from the expected spherical aberration, and the reconstructed profile is in good agreement with the mechanical stylus measurement. However, how is it possible to evaluate the accuracy of such measurement? Among the sources of error, we can mention:

- An error in the measurement plane position  $z_m$ . In principle, positioning can be performed accurately, and this uncertainty can be estimated.
- The homogeneity of the material. Local variations of the refractive index induce undesired wavefront aberrations. However, these variations can be measured accurately, and they are negligible for glass [124, 125].
- The diffraction is neglected: first, the finite extent of the aperture is not considered. However, for an aperture  $> 150\mu\text{m}$ , this is not a problem [126]. Secondly, the intensity variation of the transmitted light due to the transmission coefficient, which depends on the surface slope [127], is not taken into consideration.
- Aberrations of the imaging system. This is the most problematic part as it is difficult, if not impossible, to characterize and to correct.

A method that is used in classical optics to address this issue of accuracy is the null test [44]. It can be done in reflection, but until recently and the development of direct writing, aspheric micro-surface of reference could not be manufactured. The accuracy of such a surface should also be verified. Another option in classical optics is the utilization of computer-generated holograms (CGHs) [128–130]. However, in micro-optics, a microscope objective is required to upscale the field to the classical scale to record it on a camera. Because of the fabrication technique limitations, computer generated-holograms cannot shape wavefront at the micro-scale, and the aberration of the microscope objective cannot thus be suppressed. An exception is the 1D case of cylindrical microlenses tested with gratings [131]. One practical alternative would be to use a golden sample that is well characterized by other means, e.g., by using an

ultrahigh accurate 3D profilometer [132] with rigorous optical simulation to assess the error produced by the optical imaging system.

## **5.5 Conclusion**

This chapter discusses the characterization of high NA microlenses in transmission by probing their optical function. In particular, we report on a characterization based on PSF and wavefront measurements.

Firstly, we show that a characterization based on PSF measurements allows us to evaluate the microlens quality by deriving the Strehl ratio. However, we point out the fact that the test conditions must be similar to the working conditions for this assessment to be meaningful. This limits the versatility of the approach in terms of microlens geometries. Also, we discuss the issue of aperture determination in the case of RIE based microlenses. On the other side, we claim our doubts about the possibility of determining information in order to optimize the fabrication process.

Secondly, we discuss wavefront measurements by interferometry. In this case, we show that the testing conditions may be slightly different from the working conditions. This allows a characterization without modifying the setup for different microlens geometries, which is a clear advantage of this method. We also show how the phase information can be processed to reconstruct the surface form, thus giving feedback for the manufacturer in order to optimize the fabrication process. A single interferometric measurement can thus fulfill both purposes of the characterization. For this reason, we believe that phase measurements are more suited than PSF measurements for the characterization of high NA microlenses.

An important question that remains open is the expected accuracy of this method. Because the measurements are not performed in a null test configuration, one may expect aberrations from the optical systems which are difficult to assess or correct. For implementation in a production environment, this problem and instrument automation are the main challenges that have to be faced.



## 6 Conclusion

### 6.1 Summary and discussion

The goal of this thesis is to improve the quality of wafer-level microlenses by considering selected steps involved in their manufacturing: the microlens surface measurement, the performance assessment, and the fabrication process optimization.

To reach this objective, we firstly start by studying surface form tolerancing. As the surface is the main component of a microlens, its form governs the optical performance. For this reason, tolerancing the form of a microlens surface is a common way to control its quality. In this thesis, we study the link between the surface form and optical performance to understand which surface parameters are the most correlated to the optical performance. For instance, we find that the slope deviation is an important parameter when the RMS spot size well describes the optical performance. Then, we make a comparison between the suggested parameters and conventional tolerances. Based on the results, we propose guidelines for typical applications. In particular, we show that common ways of tolerancing that are used with the customers are often not the most efficient approaches.

The direct effect of a smarter choice of tolerances is a better assessment of the microlens quality, which allows larger tolerances and less discarded microlenses. In consequence, this allows production at lower cost and with a lower risk of performance failure.

Second, we study the microlens surface measurement by optical surface profilers. This step is essential as it enables the microlens quality control and fabrication process optimization. In particular, we assess and improve surface measurement accuracy. More precisely, we show that an error appears in such measurements, and we illustrate this in the particular case of a confocal microscope. We discuss the origin of the error and propose a method based on reference balls to correct it. In the presented example, the error value for typical spherical surfaces goes from 140 nm RMS to 20 nm RMS after the correction procedure. This represents an improvement by a factor of 7. This method also benefits from an original calibration procedure that gives a ROC uncertainty of about 0.01%.

An advantage of the proposed approach is the possibility to use microscope objectives that have residual aberrations to measure the surface of microlenses accurately. This means the possibility to use higher numerical aperture objectives for a given FOV. Without this method, accurate measurements are limited to spherical microlenses with a radius of curvature similar to existing reference balls. Consequently, it extends the characterization capability in terms of diameter, surface slope, and surface form, which is especially crucial for aspheric microlenses.

Finally, we model the microlens fabrication process to be optimized more quickly and more accurately. We start with an empirical description of the resist reflow process based on surface tension and experimental evidence. In a second step, we create models for the reactive ion etching process. Again, we use an empirical approach that relies on macroscopic parameters. We also discuss the limitations of this technology. Then, we use these models to increase the uniformity of a large (100 mm  $\times$  100 mm) MLA by changing the photomask design. In terms of optical quality, the average optical performance over the MLA is improved by a factor  $\sim 3$ . This shows that a correct tuning of the process parameters allows improving the average quality of the microlenses, which is not possible without a reliable model of the process.

Improving the fabrication process means, in particular, a general quality improvement over one wafer, which may signify more microlenses within the optical specification. Accurate modeling also renders the process of fabrication optimization faster, meaning saving time and resources.

Besides these three points, we also discuss an alternative of surface measurement to characterize the microlenses. It is based on the measurement of the microlens optical function in transmission. We show that such measurements allow assessing the microlens quality by wavefront aberration determination and also allows the reconstruction of the surface, which is necessary to optimize the fabrication process. The only doubt we have about the method is its accuracy and its implementation in an industrial environment. Such a method would be useful for microlenses that cannot be characterized in reflection by optical surface profilers.

To stress the significance of this work, we have to recall that wafer-level techniques are made for high volume production of high-quality microlenses. Because thousands of microlenses are manufactured in parallel, an enhancement of the microlens performance impacts the thousands of systems where they are implemented. Small improvements have thus a high impact.

In this thesis, we discuss a characterization based on surface measurements. Such an approach has crucial advantages in an industrial environment: the instruments are reliable and commercially available, the measurement is relatively fast, the accuracy is generally sufficient, and the measurement configuration does not depend on the microlens geometry. To give a little more context, we list here the different types of microlenses for which this approach is used and works, fails, and when alternatives must be found.

Firstly, the microlenses that can easily be characterized in reflection with optical surface



profilers, and no significant error is present in the measurement. The characterization of such microlenses does not present any particular difficulty. The microlenses that belong to this category are typically large and flat, diameter  $2a < 800\mu\text{m}$  and surface slope  $< 15^\circ$ , or small and steep, diameter  $2a < 300\mu\text{m}$  and surface slope  $< 25^\circ$ .

Secondly, the microlenses that can be characterized in reflection by surface optical profilers but that require high NA microscope objectives for a given field of view with the consequence of an error in the measured surface. In principle, confocal microscopes must be used instead of coherence scanning interferometers for this type of microlenses. This thesis offers an answer to this problem as it proposes a method to correct such error. Surface measurements with the proposed correction method are thus still an excellent way to characterize this type of microlenses. This category includes microlenses that have the following typical dimensions: diameter  $2a < 800\mu\text{m}$  and surface slope  $< 25^\circ$  or diameter  $2a < 300\mu\text{m}$  and surface slope  $< 35^\circ$ .

Thirdly and finally, the microlenses that cannot be characterized in reflection with a single frame by optical surface profilers. These microlenses are typically large and steep. The possible alternatives are optical surface profilers with high magnification (NA) microscope objectives combined with images stitching, mechanical contact profilers that scan the surface, or optical function measurements in transmission. The choice of the alternative is based on considerations such as accuracy and time. However, most of the microlenses manufactured by resist reflow and RIE fall in the first two categories and are thus well characterized based on surface measurements by optical surface profilers.

It is also worth commenting on the case of MLAs, which is slightly different. Indeed, the quality is no more defined by the microlenses surface, but by a collective effect of all the surfaces. As it is difficult to estimate the MLA optical quality from the individual surface forms, it is usually assessed by a functional test, which is specific to each MLA design. However, for process optimization purposes, the surface of the individual microlenses have still to be measured, and the comments mentioned above are thus valid.

## 6.2 Outlook

Even though some potentially useful results are obtained in this work, they still have to be implemented and exploited. A successful implementation in an industrial environment is a final test that validates the developed methods and ideas. Indeed, new concepts, even beautiful from a theoretical point of view, may not be implemented with success if they do not resist to considerations such as time and resources cost, automation, and complexity. Here, we list the steps that should be undertaken to implement the results presented in this thesis.

Firstly, we can make a reliable implementation of the surface measurement correction procedure, which is based on multiple measurements of a reference ball, that we propose. In particular, it could be interesting to check with the confocal microscope manufacturer if it

would be willing to implement such a method directly in the instrument software instead of using a separate post-processing script.

Secondly, we can propose and discuss the suggested methods to tolerance the surface form of microlenses with customers. Also, we have to prevent the use of inefficient approaches. Nevertheless, in practice, this is not as easy as it sounds. Indeed, the optical designer has the final word on the method he wants to use and does not often understand the consequences of such a choice. Such implementation is, in part, a pedagogical work.

Finally, we can implement tools to model the fabrication process based on surface measurements automatically. This would help the engineers that set the fabrication process more accurately. This would particularly help to assess the RIE process.

Besides the implementation of the results, this work could be pursued by extending some investigations further. In the following, we propose the ideas that we consider as the most relevant to be developed in the short term.

We can continue the investigation about microlens tolerancing. We can extend the idea we developed by introducing more surface parameters and by studying more real applications. Also, we can extend it to freeform surfaces that are slowly being developed in micro-optics. Finally, we can extend it to complex systems that consist of several MLAs and which performance is the combination of a large number of parameters. The challenge would be to link the set of parameters to the final optical performance. Ideally, if successfully done, this would render the quality check based on a functional test useless. Also, this would allow the discarding of bad elements early in the production stage, thus saving time and resources.

The methods developed here could also be adapted to other manufacturing techniques. In particular, empirical models describing the UV imprint fabrication process would be useful. Indeed, polymer shrinkage and mold deformations provoke modifications of the surface form during the curing process. Accurate feedback is thus required to compensate for these effects, and for this reason, a model is a necessary step towards successful manufacturing.

To conclude, we believe that a quantitative description of the full microlens fabrication process, such as partially done in this thesis, should be continued and extended. Indeed, this allows for better control and understanding of the microlens fabrication, thus allowing a better quality at a more effective cost. This is especially important for us as a manufacturer because refractive micro-optics is leaving the status of niche technology and is rapidly gaining in importance.

# Bibliography

- [1] Roshdi Rashed. A pioneer in anaclastics: Ibn sahl on burning mirrors and lenses. *Isis*, 81(3):464–491, 1990.
- [2] Claude Phipps. *Islamic Science and Art*, chapter 10, pages 105–112. Springer International Publishing, 2016.
- [3] George Sines and Yannis A. Sakellarakis. Lenses in antiquity. *American Journal of Archaeology*, 91(2):191–196, 1987.
- [4] Zoran D. Popovic, Robert A. Sprague, and G. A. Neville Connell. Technique for monolithic fabrication of microlens arrays. *Appl. Opt.*, 27(7):1281–1284, 1988.
- [5] Dan-Eric Nilsson. Optics and evolution of the compound eye. In Doekele Gerben Stavenga and Roger Clayton Hardie, editors, *Facets of Vision*, pages 30–73, Berlin, Heidelberg, 1989. Springer Berlin Heidelberg.
- [6] Joanna Aizenberg and Gordon Hendler. Designing efficient microlens arrays: lessons from nature. *J. Mater. Chem.*, 14:2066–2072, 2004.
- [7] Ki-Hun Jeong, Jaeyoun Kim, and Luke P. Lee. Biologically inspired artificial compound eyes. *Science*, 312(5773):557–561, 2006.
- [8] C. A. Edwards, H. M. Presby, and C. Dragone. Ideal microlenses for laser to fiber coupling. *Journal of Lightwave Technology*, 11(2):252–257, 1993.
- [9] Eva M. Strzelecka, Duane A. Louderback, Brian J. Thibeault, Geoff B. Thompson, Kent Bertilsson, and Larry A. Coldren. Parallel free-space optical interconnect based on arrays of vertical-cavity lasers and detectors with monolithic microlenses. *Appl. Opt.*, 37(14):2811–2821, 1998.
- [10] Reinhard Voelkel, Hans Peter Herzig, Philippe Nussbaum, Rene Daendliker, and William B. Hogle. Microlens array imaging system for photolithography. *Optical Engineering*, 35(11):3323 – 3330, 1996.
- [11] Ming-Hsien Wu and George M Whitesides. Fabrication of two-dimensional arrays of microlenses and their applications in photolithography. *Journal of Micromechanics and Microengineering*, 12(6):747–758, 2002.

- [12] Guy Edouard Artzner. Microlens arrays for Shack-Hartmann wavefront sensors. *Optical Engineering*, 31(6):1311 – 1322, 1992.
- [13] Geun Young Yoon, Takahisa Jitsuno, Masahiro Nakatsuka, and Sadao Nakai. Shack hartmann wave-front measurement with a large f-number plastic microlens array. *Appl. Opt.*, 35(1):188–192, 1996.
- [14] Jérôme Primot. Theoretical description of shack–hartmann wave-front sensor. *Optics Communications*, 222(1):81 – 92, 2003.
- [15] Tasso R. M. Sales. Structured microlens arrays for beam shaping. In Fred M. Dickey and David L. Shealy, editors, *Laser Beam Shaping IV*, volume 5175, pages 109 – 120. International Society for Optics and Photonics, SPIE, 2003.
- [16] Frank Wippermann, Uwe-D. Zeitner, Peter Dannberg, Andreas Bräuer, and Stefan Sinzinger. Beam homogenizers based on chirped microlens arrays. *Opt. Express*, 15(10):6218–6231, 2007.
- [17] Maik Zimmermann, Norbert Lindlein, Reinhard Voelkel, and Kenneth J. Weible. Microlens laser beam homogenizer: from theory to application. In Fred M. Dickey and David L. Shealy, editors, *Laser Beam Shaping VIII*, volume 6663, pages 9 – 21. International Society for Optics and Photonics, SPIE, 2007.
- [18] Ren Ng, Marc Levoy, Mathieu Brédif, Gene Duval, Mark Horowitz, and Pat Hanrahan. Light field photography with a hand-held plenoptic camera.
- [19] A. Lumsdaine and T. Georgiev. The focused plenoptic camera. In *2009 IEEE International Conference on Computational Photography (ICCP)*, pages 1–8, 2009.
- [20] Andreas Brückner, Jacques Duparré, Robert Leitel, Peter Dannberg, Andreas Bräuer, and Andreas Tünnermann. Thin wafer-level camera lenses inspired by insect compound eyes. *Opt. Express*, 18(24):24379–24394, 2010.
- [21] Peng Ge, Yang Li, Zanzi Chen, and Hong Wang. Led high-beam headlamp based on free-form microlenses. *Appl. Opt.*, 53(24):5570–5575, 2014.
- [22] David Patrick Luebke, Douglas Lanman, Thomas F Fox, and Gerrit Slavenburg. Near-eye microlens array displays, 2017. US Patent 9,841,537.
- [23] Herbert Gross, Hannfried Zügge, Martin Peschka, and Fritz Blechinger. *Correction of Aberrations*, chapter 31, pages 215–289. John Wiley & Sons, Ltd, 2015.
- [24] H Ottevaere, R Cox, H P Herzig, T Miyashita, K Naessens, M Taghizadeh, R Völkel, H J Woo, and H Thienpont. Comparing glass and plastic refractive microlenses fabricated with different technologies. *Journal of Optics A: Pure and Applied Optics*, 8(7):S407–S429, 2006.

- 
- [25] Reinhard Voelkel. Wafer-scale micro-optics fabrication. *Advanced Optical Technologies*, 1(3):135 – 150, 2012.
- [26] Ph Nussbaum, R Völkel, H P Herzig, M Eisner, and S Haselbeck. Design, fabrication and testing of microlens arrays for sensors and microsystems. *Pure and Applied Optics: Journal of the European Optical Society Part A*, 6(6):617–636, 1997.
- [27] Madanagopal V. Kunnavakkam, F. M. Houlihan, M. Schlax, J. A. Liddle, P. Kolodner, O. Nalamasu, and J. A. Rogers. Low-cost, low-loss microlens arrays fabricated by soft-lithography replication process. *Applied Physics Letters*, 82(8):1152–1154, 2003.
- [28] H. Schmitt, M. Rommel, A.J. Bauer, L. Frey, A. Bich, M. Eisner, R. Voelkel, and M. Horning. Full wafer microlens replication by uv imprint lithography. *Microelectronic Engineering*, 87(5):1074 – 1076, 2010. The 35th International Conference on Micro- and Nano-Engineering (MNE).
- [29] Kris Naessens, Heidi Ottevaere, Roel Baets, Peter Van Daele, and Hugo Thienpont. Direct writing of microlenses in polycarbonate with excimer laser ablation. *Appl. Opt.*, 42(31):6349–6359, 2003.
- [30] Rui Guo, Shizhou Xiao, Xiaomin Zhai, Jiawen Li, Andong Xia, and Wenhao Huang. Micro lens fabrication by means of femtosecond two photon photopolymerization. *Opt. Express*, 14(2):810–816, 2006.
- [31] Nanoscribe GmbH. The new Quantum X redefining microfabrication. <https://www.nanoscribe.com/fileadmin/Nanoscribe/Solutions/QuantumX/QuantumX.pdf>.
- [32] A. Y. Yi and L. Li. Design and fabrication of a microlens array by use of a slow tool servo. *Opt. Lett.*, 30(13):1707–1709, 2005.
- [33] Mao Mukaida and Jiwang Yan. Ductile machining of single-crystal silicon for microlens arrays by ultraprecision diamond turning using a slow tool servo. *International Journal of Machine Tools and Manufacture*, 115:2 – 14, 2017. Far East Innovations in super-fine finishing of complex optics.
- [34] ISO:14880-1:2019. Optics and Photonics – Microlens array – Part 1: Vocabulary. Standard, International Organization for Standardization, 2019.
- [35] ISO 14880-2:2006. Optics and Photonics – Microlens array – Part 2: Test methods for wavefront aberrations. Standard, International Organization for Standardization, 2006.
- [36] ISO 14880-3:2006. Optics and Photonics – Microlens array – Part 3: Test methods for optical properties other than wavefront aberrations. Standard, International Organization for Standardization, 2006.
- [37] ISO 14880-4:2006. Optics and Photonics – Microlens array – Part 2: Test methods for geometrical properties. Standard, International Organization for Standardization, 2006.

## Bibliography

---

- [38] ISO 14880-5:2010. Optics and Photonics – Microlens array – Part 5: Guidance on testing. Standard, International Organization for Standardization, 2010.
- [39] Randall H. Wilson, Randy C. Brost, David R. Strip, Ronald J. Sudol, Richard N. Youngworth, and Paul O. McLaughlin. Considerations for tolerancing aspheric optical components. *Appl. Opt.*, 43(1):57–66, 2004.
- [40] U. Fuchs. Tolerancing aspheric surfaces in optical design. In José Sasián and Richard N. Youngworth, editors, *Optical System Alignment, Tolerancing, and Verification IX*, volume 9582, pages 27 – 33. International Society for Optics and Photonics, SPIE, 2015.
- [41] ISO 10110-5:2015. Optics and photonics - Preparation of drawings for optical elements and systems - Part 5: Surface form tolerances. Standard, International Organization for Standardization, 2015.
- [42] ISO 14999-4. Optics and photonics - Interferometric measurement of optical elements and optical systems - Part 4: Interpretation and evaluation of tolerances specified in ISO 10110. Standard, International Organization for Standardization, 2015.
- [43] ISO 10110-12. Optics and photonics - Preparation of drawings for optical elements and systems - Part 12: Aspheric surfaces. Standard, International Organization for Standardization, 2016.
- [44] D. Malacara, K. Creath, J. Schmit, and J. C. Wyant. *Testing of Aspheric Wavefronts and Surfaces*, chapter 12, pages 435–497. John Wiley & Sons, Ltd, 2006.
- [45] Herbert Gross, Hannfried Zügge, Martin Peschka, and Fritz Blechinger. *Tolerancing*, chapter 35, pages 595–716. John Wiley & Sons, Ltd, 2015.
- [46] von F. Zernike. Beugungstheorie des schneidenverfahrens und seiner verbesserten form, der phasenkontrastmethode. *Physica*, 1(7):689 – 704, 1934.
- [47] Raoul Kirner, Jeremy Béguelin, Martin Eisner, Wilfried Noell, Toralf Scharf, and Reinhard Voelkel. Improvements on the uniformity of large-area microlens arrays in fused silica. *Opt. Express*, 27(5):6249–6258, 2019.
- [48] Robert J. Noll. Zernike polynomials and atmospheric turbulence\*. *J. Opt. Soc. Am.*, 66(3):207–211, 1976.
- [49] Herbert Gross, Hannfried Zügge, Martin Peschka, and Fritz Blechinger. *Image Quality Criteria*, chapter 30, pages 71–213. John Wiley & Sons, Ltd, 2015.
- [50] J.W. Goodman. *Introduction to Fourier Optics*. Roberts & Company Publishers, 2005.
- [51] A. Shan, R.N. Roth, and R.J. Wilson. Genetic algorithms in statistical tolerancing. *Mathematical and Computer Modelling*, 38(11):1427 – 1436, 2003. Stochastic models in engineering, technology, and management.

- 
- [52] Chun Zhang and Hsu-Pin (Ben) Wang. Integrated tolerance optimisation with simulated annealing. *The International Journal of Advanced Manufacturing Technology*, 8(3):167–174, 1993.
- [53] Photon Engineering. Simulation of laser diode to fiber coupling. <https://photonengr.com/wp-content/uploads/kbasefiles/Laser-Diode-to-Fiber-Coupling-Analysis.pdf>.
- [54] Marcel Sieler, Peter Schreiber, Peter Dannberg, Andreas Bräuer, and Andreas Tünnermann. Ultraslim fixed pattern projectors with inherent homogenization of illumination. *Appl. Opt.*, 51(1):64–74, 2012.
- [55] M. Sieler, S. Fischer, P. Schreiber, P. Dannberg, and A. Bräuer. Microoptical array projectors for free-form screen applications. *Opt. Express*, 21(23):28702–28709, 2013.
- [56] John R. Rogers. Slope error tolerances for optical surfaces. In James J. Kumler and Matthias Pfaff, editors, *Optifab 2007: Technical Digest*, volume 10316, pages 5 – 8. International Society for Optics and Photonics, SPIE, 2007.
- [57] SB Kotsiantis. Supervised machine learning: A review of classification techniques. *Informatica*, 31:249–268, 2007.
- [58] Stephan Reichelt and Hans Zappe. Combined twyman–green and mach–zehnder interferometer for microlens testing. *Appl. Opt.*, 44(27):5786–5792, 2005.
- [59] ISO 25178-607:2019. Geometrical product specifications (GPS)–Surface texture: Areal–Part 607: Nominal characteristics of non-contact (confocal microscopy) instruments. Standard, International Organization for Standardization, 2019.
- [60] Roger Artigas. Imaging confocal microscopy. In Richard Leach, editor, *Optical Measurement of Surface Topography*, pages 237–286. Springer Berlin Heidelberg, 2011.
- [61] ISO 25178-604:2013. Geometrical product specifications (GPS)–Surface texture: Areal–Part 604: Nominal characteristics of non-contact (coherence scanning interferometry) instruments. Standard, International Organization for Standardization, 2013.
- [62] Peter de Groot. Coherence scanning interferometry. In Richard Leach, editor, *Optical Measurement of Surface Topography*, pages 187–208. Springer Berlin Heidelberg, 2011.
- [63] JCGM 100:2008. Evaluation of measurement data – Guide to the expression of uncertainty in measurement. Guide, Joint Committee for Guides in Metrology, 2008.
- [64] JCGM 101:2008. Evaluation of measurement data – Supplement 1 to the "Guide to the expression of uncertainty in measurement" – Propagation of distributions using a Monte Carlo method. Guide, Joint Committee for Guides in Metrology, 2008.
- [65] JCGM 104:2009. Evaluation of measurement data – An introduction to the "Guide to the expression of uncertainty in measurement" and related documents. Guide, Joint Committee for Guides in Metrology, 2009.

- [66] JCGM 102:2011. Evaluation of measurement data – Supplement 2 to the "Guide to the expression of uncertainty in measurement" – Extension to any number of output quantities. Guide, Joint Committee for Guides in Metrology, 2011.
- [67] JCGM 106:2012. Evaluation of measurement data – The role of measurement uncertainty in conformity assessment. Guide, Joint Committee for Guides in Metrology, 2012.
- [68] Peter J. de Groot. Progress in the specification of optical instruments for the measurement of surface form and texture. In Kevin G. Harding and Toru Yoshizawa, editors, *Dimensional Optical Metrology and Inspection for Practical Applications III*, volume 9110, pages 131 – 142. International Society for Optics and Photonics, SPIE, 2014.
- [69] DIN 5401:2002-08. Rolling bearings - Balls for rolling bearings and general industrial use. Standard, Deutsches Institut für Normung, 2002.
- [70] Helmut Groemer. *Geometric Applications of Fourier Series and Spherical Harmonics*. Encyclopedia of Mathematics and its Applications. Cambridge University Press, 1996.
- [71] Ping Zhou and James H. Burge. Limits for interferometer calibration using the random ball test. In James H. Burge, Oliver W. Föhnle, and Ray Williamson, editors, *Optical Manufacturing and Testing VIII*, volume 7426, pages 241 – 252. International Society for Optics and Photonics, SPIE, 2009.
- [72] Ulf Griesmann, Quandou Wang, Johannes Soons, and Remi Carakos. A simple ball averager for reference sphere calibrations. In H. Philip Stahl, editor, *Optical Manufacturing and Testing VI*, volume 5869, pages 189 – 196. International Society for Optics and Photonics, SPIE, 2005.
- [73] Giacomo Maculotti, Xiaobing Feng, Rong Su, Maurizio Galetto, and Richard Leach. Residual flatness and scale calibration for a point autofocus surface topography measuring instrument. *Measurement Science and Technology*, 30(7):075005, 2019.
- [74] Goran Baer, Johannes Schindler, Christof Pruss, Jens Siepmann, and Wolfgang Osten. Calibration of a non-null test interferometer for the measurement of aspheres and free-form surfaces. *Opt. Express*, 22(25):31200–31211, 2014.
- [75] Dong Liu, Yongying Yang, Chao Tian, Yongjie Luo, and Lin Wang. Practical methods for retrace error correction in nonnull aspheric testing. *Opt. Express*, 17(9):7025–7035, 2009.
- [76] J M Coupland and J Lobera. Holography, tomography and 3d microscopy as linear filtering operations. *Measurement Science and Technology*, 19(7):074012, 2008.
- [77] Jeremy Coupland, Rahul Mandal, Kanik Palodhi, and Richard Leach. Coherence scanning interferometry: linear theory of surface measurement. *Appl. Opt.*, 52(16):3662–3670, 2013.



- 
- [78] Rahul Mandal, Jeremy Coupland, Richard Leach, and Daniel Mansfield. Coherence scanning interferometry: measurement and correction of three-dimensional transfer and point-spread characteristics. *Appl. Opt.*, 53(8):1554–1563, 2014.
- [79] Rong Su, Yuhang Wang, Jeremy Coupland, and Richard Leach. On tilt and curvature dependent errors and the calibration of coherence scanning interferometry. *Opt. Express*, 25(4):3297–3310, 2017.
- [80] Rong Su, Matthew Thomas, Richard Leach, and Jeremy Coupland. Effects of defocus on the transfer function of coherence scanning interferometry. *Opt. Lett.*, 43(1):82–85, 2018.
- [81] Herbert Gross, Fritz Blechinger, and Bertram Aichtner. *Microscope Optics*, chapter 42, pages 541–721. John Wiley & Sons, Ltd, 2015.
- [82] J. Park, S. Byun, and B. Lee. Lens distortion correction using ideal image coordinates. *IEEE Transactions on Consumer Electronics*, 55(3):987–991, 2009.
- [83] Peter Ekberg, Rong Su, and Richard Leach. High-precision lateral distortion measurement and correction in coherence scanning interferometry using an arbitrary surface. *Opt. Express*, 25(16):18703–18712, 2017.
- [84] Yue Zhou, Young-Sik Ghim, Ali Fard, and Angela Davies. Application of the random ball test for calibrating slope-dependent errors in profilometry measurements. *Appl. Opt.*, 52(24):5925–5931, 2013.
- [85] Carlos Bermudez, André Felgner, Pol Martinez, Aitor Matilla, Cristina Cadevall, and Roger Artigas. Residual flatness error correction in three-dimensional imaging confocal microscopes. In Christophe Gorecki, Anand Krishna Asundi, and Wolfgang Osten, editors, *Optical Micro- and Nanometrology VII*, volume 10678, pages 116 – 125. International Society for Optics and Photonics, SPIE, 2018.
- [86] Herbert Gross, Bernd Dörband, and Henriette Müller. *Testing the Geometry of Optical Components*, chapter 53, pages 679–783. John Wiley & Sons, Ltd, 2015.
- [87] Albrecht v. Pfeil, Frank Wyrowski, Andreas Drauschke, and Harald Aagedal. Analysis of optical elements with the local plane-interface approximation. *Appl. Opt.*, 39(19):3304–3313, 2000.
- [88] Ian Goodfellow, Yoshua Bengio, and Aaron Courville. *Deep Learning*. MIT Press, 2016. <http://www.deeplearningbook.org>.
- [89] Herbert Gross. *Raytracing*, chapter 5, pages 173–228. John Wiley & Sons, Ltd, 2015.
- [90] Herbert Gross, Hannfried Zügge, Martin Peschka, and Fritz Blechinger. *Aberrations*, chapter 29, pages 1–70. John Wiley & Sons, Ltd, 2015.

- [91] Robert Kirchner and Helmut Schiff. Thermal reflow of polymers for innovative and smart 3d structures: A review. *Materials Science in Semiconductor Processing*, 92:58 – 72, 2019. Material processing of optical devices and their applications.
- [92] Andreas Schilling, R. Merz, Christian Ossmann, and Hans Peter Herzig. Surface profiles of reflow microlenses under the influence of surface tension and gravity. *Optical Engineering*, 39(8):2171 – 2176, 2000.
- [93] Myung-Geun Han, Yoon-Jung Park, Seoung-Hoe Kim, Byueng-Su Yoo, and Hyo-Hoon Park. Thermal and chemical stability of reflowed-photoresist microlenses. *Journal of Micromechanics and Microengineering*, 14(3):398–402, dec 2003.
- [94] Sébastien Bérard-Bergery, Jérôme Hazart, Jean-Baptiste Henry, Patrick Quéméré, Charlotte Beylier, Nacima Allouti, Maryline Cordeau, Raphaël Eleouet, Florian Tomaso, Alain Ostrovsky, and Valérie Rousset. 3D resist reflow compact model for imagers microlens shape optimization. In Jason P. Cain, editor, *Design-Process-Technology Co-optimization for Manufacturability XIII*, volume 10962, pages 95 – 114. International Society for Optics and Photonics, SPIE, 2019.
- [95] Bastian E. Rapp. Chapter 21 - capillarity. In Bastian E. Rapp, editor, *Microfluidics: Modelling, Mechanics and Mathematics*, Micro and Nano Technologies, pages 445 – 451. Elsevier, Oxford, 2017.
- [96] Jacob J. Bikerman. Chapter ii - physical chemistry of liquid surfaces. In J.J. Bikerman, editor, *Physical Surfaces*, volume 20 of *Physical Chemistry*, pages 44 – 116. Elsevier, 1970.
- [97] Sumiyoshi Abe and John T. Sheridan. Curvature correction model of droplet profiles. *Physics Letters A*, 253(5):317 – 321, 1999.
- [98] Joon-Min Park, Eun-Jin Kim, Joo-Yoo Hong, Ilsin An, and Hye-Keun Oh. Photoresist adhesion effect of resist reflow process. *Japanese Journal of Applied Physics*, 46(9A):5738–5741, 2007.
- [99] Feidhlim T. O'Neill and John T. Sheridan. Photoresist reflow method of microlens production part i: Background and experiments. *Optik*, 113(9):391 – 404, 2002.
- [100] Feidhlim T. O'Neill and John T. Sheridan. Photoresist reflow method of microlens production part ii: Analytic models. *Optik*, 113(9):405 – 420, 2002.
- [101] G. C. Schwartz and P. M. Schaible. Reactive ion etching of silicon. *Journal of Vacuum Science and Technology*, 16(2):410–413, 1979.
- [102] Henri Jansen, Han Gardeniers, Meint de Boer, Miko Elwenspoek, and Jan Fluitman. A survey on the reactive ion etching of silicon in microtechnology. *Journal of Micromechanics and Microengineering*, 6(1):14–28, 1996.
- [103] G. C. Schwartz. Competitive mechanisms in reactive ion etching in a  $\text{CF}_4$  plasma. *Journal of The Electrochemical Society*, 126(3):464, 1979.

- 
- [104] Raoul Kirner. *On Advanced Large-Field Photolithography*. PhD thesis, Lausanne, 2019.
- [105] Yuki Onishi, Ryunosuke Yamashita, Kenji Amaya, and Yoshihiko Hirai. Numerical modeling method for uv imprint process simulation using thermoviscoelastic constitutive equations. *Journal of Vacuum Science & Technology B*, 37(6):062915, 2019.
- [106] Paul D. Pulaski, James P. Roller, Daniel R. Neal, and Keith Ratte. Measurement of aberrations in microlenses using a Shack-Hartmann wavefront sensor. In Robert E. Fischer, Warren J. Smith, and R. Barry Johnson, editors, *Current Developments in Lens Design and Optical Engineering III*, volume 4767, pages 44 – 52. International Society for Optics and Photonics, SPIE, 2002.
- [107] Florian Charrière, Jonas Kühn, Tristan Colomb, Frédéric Montfort, Etienne Cuche, Yves Emery, Kenneth Weible, Pierre Marquet, and Christian Depeursinge. Characterization of microlenses by digital holographic microscopy. *Appl. Opt.*, 45(5):829–835, 2006.
- [108] Joseph J.M. Braat, Sven van Haver, Augustus J.E.M. Janssen, and Peter Dirksen. Chapter 6 assessment of optical systems by means of point-spread functions. volume 51 of *Progress in Optics*, pages 349 – 468. Elsevier, 2008.
- [109] Maciej Baranski, Stephane Perrin, Nicolas Passilly, Luc Froehly, Jorge Alberro, Sylwester Bargiel, and Christophe Gorecki. A simple method for quality evaluation of micro-optical components based on 3d ipsf measurement. *Opt. Express*, 22(11):13202–13212, 2014.
- [110] Myun-Sik Kim, Toralf Scharf, and Hans Peter Herzig. Small-size microlens characterization by multiwavelength high-resolution interference microscopy. *Opt. Express*, 18(14):14319–14329, 2010.
- [111] Carsten Rockstuhl, Iwan Märki, Toralf Scharf, Martin Salt, Hans Peter Herzig, and René Dändliker. High resolution interference microscopy: A tool for probing optical waves in the far-field on a nanometric length scale. *Current Nanoscience*, 2:337–350, 2006.
- [112] Myun-Sik Kim, Toralf Scharf, Stefan Mühlig, Carsten Rockstuhl, and Hans Peter Herzig. Engineering photonic nanojets. *Opt. Express*, 19(11):10206–10220, 2011.
- [113] Myun-Sik Kim, Toralf Scharf, Stefan Mühlig, Carsten Rockstuhl, and Hans Peter Herzig. Gouy phase anomaly in photonic nanojets. *Applied Physics Letters*, 98(19):191114, 2011.
- [114] Michail Symeonidis, Radius N. S. Suryadharma, Rossella Grillo, Andreas Vetter, Carsten Rockstuhl, Thomas Bürgi, and Toralf Scharf. High-resolution interference microscopy with spectral resolution for the characterization of individual particles and self-assembled meta-atoms. *Opt. Express*, 27(15):20990–21003, 2019.
- [115] Michail Symeonidis, Wataru Nakagawa, Dong Cheon Kim, Andreas Hermerschmidt, and Toralf Scharf. High-resolution interference microscopy of binary phase diffractive optical elements. *OSA Continuum*, 2(9):2496–2510, 2019.

## Bibliography

---

- [116] P. Hariharan, B. F. Oreb, and T. Eiju. Digital phase-shifting interferometry: a simple error-compensating phase calculation algorithm. *Appl. Opt.*, 26(13):2504–2506, 1987.
- [117] E. P. Goodwin and J. C. Wyant. *Field guide to interferometric optical testing*. 2006.
- [118] T Kozacki, M Jóźwik, and R Jóźwicki. Determination of optical field generated by a microlens using digital holographic method. *Opto-Electronics Review*, 17:211–216, 2009.
- [119] G. B. Airy. On the Diffraction of an Object-glass with Circular Aperture. *Transactions of the Cambridge Philosophical Society*, 5:283, 1835.
- [120] Max Born and Emil Wolf. *Principles of Optics: Electromagnetic Theory of Propagation, Interference and Diffraction of Light*. Cambridge University Press, 1999.
- [121] Herbert Gross, Hannfried Zügge, Martin Peschka, and Fritz Blechinger. *Image Quality Criteria*, chapter 30, pages 71–213. John Wiley & Sons, Ltd, 2015.
- [122] James C Wyant and Katherine Creath. *Basic Wavefront Aberration Theory for Optical Metrology*, chapter 1, pages 1–53. Academic Press, Inc., 1992.
- [123] Larry N. Thibos, Raymond A. Applegate, James T. Schwiegerling, and Robert Webb and. Standards for reporting the optical aberrations of eyes. In *Vision Science and its Applications*, page SuC1. Optical Society of America, 2000.
- [124] Johannes Schwider, R. Burow, K.-E. Elssner, R. Spolaczyk, and J. Grzanna. Homogeneity testing by phase sampling interferometry. *Appl. Opt.*, 24(18):3059–3061, 1985.
- [125] J. M. De Freitas and M. A. Player. Ultrahigh precision measurements of optical heterogeneity of high quality fused silica. *Applied Physics Letters*, 66(26):3552–3554, 1995.
- [126] Myun-Sik Kim, Toralf Scharf, Stefan Mühlig, Martin Fruhnert, Carsten Rockstuhl, Roland Bitterli, Wilfried Noell, Reinhard Voelkel, and Hans Peter Herzig. Refraction limit of miniaturized optical systems: a ball-lens example. *Opt. Express*, 24(7):6996–7005, 2016.
- [127] Herbert Gross. *Interfaces*, chapter 3, pages 61–109. John Wiley & Sons, Ltd, 2015.
- [128] A. J. MacGovern and J. C. Wyant. Computer generated holograms for testing optical elements. *Appl. Opt.*, 10(3):619–624, 1971.
- [129] J. C. Wyant and V. P. Bennett. Using computer generated holograms to test aspheric wavefronts. *Appl. Opt.*, 11(12):2833–2839, 1972.
- [130] Christof Pruss, Stephan Reichelt, Hans J. Tiziani, and Wolfgang Osten. Computer-generated holograms in interferometric testing. *Optical Engineering*, 43(11):2534 – 2540, 2004.
- [131] Juergen Lamprecht, Norbert Lindlein, and Johannes Schwider. Null test measurement of high-numerical-aperture cylindrical microlenses in transmitted light. In H. Philip Stahl, editor, *Optical Manufacturing and Testing V*, volume 5180, pages 253 – 260. International Society for Optics and Photonics, SPIE, 2003.

- [132] Hideki Tsutsumi, Keiichi Yoshizumi, and Hiroyuki Takeuchi. Ultrahighly accurate 3D profilometer. In Yongtian Wang, Zhicheng Weng, Shenghua Ye, and Jose M. Sasian, editors, *Optical Design and Testing II*, volume 5638, pages 387 – 394. International Society for Optics and Photonics, SPIE, 2005.



# Acronyms

**CSI** : Coherence Scanning Interferometer

**FOM** : Figure of Merit

**FOV** : Field of View

**ISO** : International Organization for Standardization

**MLA** : Microlens Array

**NA** : Numerical Aperture

**PSF** : Point Spread Function

**PV** : Peak-to-Valley

**RMS** : Root Mean Square

**ROC** : Radius of Curvature

**UV** : Ultraviolet





# Nomenclature

$A$  : the area of an aperture.

$a$  : the semi-diameter of a microlens.

$a_c$  : the semi-diameter of a resist cylinder.

$a_s$  : the semi-diameter of a resist microlens.

$\alpha_z$  : the amplification coefficient of a scanning optical surface profiler.

$c_1, c_2, \dots$  : the coefficients of the Zernike polynomials.

$c_{\alpha_z}$  : the calibration coefficient of the amplification coefficient.

$c_M$  : the calibration coefficient of the magnification.

$D$  : the surface derivative.

$d$  : a distance.

$\epsilon$  : a surface error.

$\eta_e$  : the ratio between anisotropic and isotropic components in a reactive ion etching process.

$\eta_r$  : the photoresist reflow shrinkage.

$f$  : a focal length.

$f_{E,b}$  : the effective back focal length of a microlens.

## Nomenclature

---

$f_{E,f}$  : the effective front focal length of a microlens.

$f_{sub}$  : the back focal length of a microlens when situated in the substrate.

$\gamma$  : the ratio between the calibrated and non-calibrated value of the radius of curvature.

$h_c$  : the height of a resist cylinder.

$h_r$  : the height of a resist microlens.

$h_s$  : the height of an etched microlens.

$I$  : an irradiance.

$\vec{i}$  : a set of input parameters.

$k$  : a wave number.

$\kappa$  : the conic constant.

$L$  : a loss or cost function.

$\lambda$  : the wavelength of light.

$M$  : the magnification of an imaging system.

$m$  : the slope of a ray of light.

$n$  : the refractive index.

$v_r$  : the resist etching rate.

$v_s$  : the substrate etching rate.

$\vec{o}$  : a set of output parameters.

$P$  : a fabrication process.

$P_0$  : the light power falling on an aperture.

$\phi$  : the phase of a wave of light.

- $R$  : the radius of curvature.
- $r$  : the radial position.
- $\rho$  : a surface residual.
- $\varrho$  : the normalized radial position.
- $S$  : a surface.
- $s$  : the sag of a surface.
- $SR$  : the Strehl ratio.
- $\sigma$  : a standard deviation.
- $\Sigma$  : the etching selectivity.
- $T$  : the substrate thickness.
- $\theta_c$  : the photoresist contact angle.
- $\Upsilon$  : a reactive ion etching process.
- $v$  : a lateral aberration.
- $u$  : a standard uncertainty.
- $V_c$  : the volume of a resist cylinder.
- $V_r$  : the volume of a resist lens.
- $Y_m^l$  : a spherical harmonic.



# Publications

Peer-review journal articles as first author:

- Jeremy Béguelin, Wilfried Noell, Toralf Scharf, and Reinhard Voelkel, "Tolerancing the surface form of aspheric microlenses manufactured by wafer-level optics techniques," Appl. Opt. 59, 3910-3919 (2020)
- Jeremy Béguelin, Michael Symeonidis, Wilfried Noell, Reinhard Voelkel, and Toralf Scharf, "Optical characterization of high numerical aperture microlenses for quality assessment and fabrication process optimization," Appl. Opt. 59, 3601-3607 (2020)
- Jeremy Béguelin, Toralf Scharf, Wilfried Noell, and Reinhard Voelkel, "Correction of spherical surface measurements by confocal microscopy," Meas. Sci. Technol. 31, 075002 (2020)

Peer-review journal article with shared first authorship:

- Raoul Kirner, Jeremy Béguelin, Martin Eisner, Wilfried Noell, Toralf Scharf, and Reinhard Voelkel, "Improvements on the uniformity of large-area microlens arrays in Fused Silica," Opt. Express 27, 6249-6258 (2019)

Presentations at conferences with respective proceedings:

- Jeremy Béguelin, Toralf Scharf, Wilfried Noell, Reinhard Voelkel, "Specification of aspherical surfaces used as refractive elements in micro-optical systems," Proc. SPIE 11103, Optical Modeling and System Alignment, 1110309 (30 August 2019)
- Jeremy Béguelin, Toralf Scharf, Wilfried Noell, Reinhard Voelkel, "Correction of surface error occurring in microlenses characterization performed by optical profilers," Proc. SPIE 11056, Optical Measurement Systems for Industrial Inspection XI, 110560Z (21 June 2019)

## **Publications**

---

- Jeremy Béguelin, Toralf Scharf, Wilfried Noell, Reinhard Voelkel, "Improved calibration of vertical scanning optical profilometers for spherical profiles measurements," Proc. SPIE 10692, Optical Fabrication, Testing, and Metrology VI, 1069207 (15 June 2018)
- Jeremy Béguelin, Michail Symeonidis, Wilfried Noell, Reinhard Voelkel, Toralf Scharf, "Assessing microlens quality based on 3D irradiance measurement at the focal spot area," Proc. SPIE 10678, Optical Micro- and Nanometrology VII, 106780B (24 May 2018)

Contribution to proceedings:

- Raoul Kirner, Jeremy Béguelin, Wilfried Noell, Martin Eisner, Toralf Scharf, Reinhard Voelkel, "Leveraging wafer-level manufacturing process limitations to increase large-scale fused silica microlens array uniformity," Proc. SPIE 11103, Optical Modeling and System Alignment, 111030A (30 August 2019)

# Curriculum Vitae

## Jeremy Béguelin

### Personal details and contact:

Birth: March 4 1991, Neuchâtel  
Nationality: Swiss  
Language: French, English  
Email: jeremy.beguelin@gmail.com  
Phone: +41 79 738 58 46

### Education:

Jul. 2020 Ph.D in Photonics, École Polytechnique Fédérale de Lausanne  
Sept. 2016 M.Sc. in Physics, École Polytechnique Fédérale de Lausanne  
Sept. 2014 B.Sc. in Physics, École Polytechnique Fédérale de Lausanne

### Affiliations:

Sept. 2016- Optical engineer at SUSS MicroOptics SA  
Feb.-Sept. 2016 Visiting scholar at University of California, Berkeley  
Jul.-Dec. 2015 Intern at SUSS MicroOptics SA